2009-03-20

Laser Levitation of Solid Particles for Combustion and Gasification Applications

Skigh E. Lewis
Brigham Young University - Provo

BYU ScholarsArchive Citation

Lewis, Skigh E., "Laser Levitation of Solid Particles for Combustion and Gasification Applications" (2009). *All Theses and Dissertations*. 1757.
https://scholarsarchive.byu.edu/etd/1757

LASER LEVITATION OF SOLID PARTICLES FOR COMBUSTION AND GASIFICATION APPLICATIONS

by

Skigh E. Lewis

A dissertation submitted to the faculty of

Brigham Young University

in partial fulfillment of the requirements for the degree of

Doctor of Philosophy

Department of Chemical Engineering

Brigham Young University

April 2009

BRIGHAM YOUNG UNIVERSITY

GRADUATE COMMITTEE APPROVAL

of a dissertation submitted by

Skigh E. Lewis

This dissertation has been read by each member of the following graduate committee and by majority vote has been found to be satisfactory.

Date	Larry L. Baxter, Chair
Date	John L. Oscarson, Member
Date	Thomas H. Fletcher, Member
Date	William C. Hecker, Member
Date	Dean R. Wheeler, Member

BRIGHAM YOUNG UNIVERSITY

As chair of the candidate’s graduate committee, I have read the dissertation of Skigh E. Lewis in its final form and have found that (1) its format, citations, and bibliographical style are consistent and acceptable and fulfill university and department style requirements; (2) its illustrative materials including figures, tables, and charts are in place; and (3) the final manuscript is satisfactory to the graduate committee and is ready for submission to the university library.

Date

Larry L. Baxter
Chair, Graduate Committee

Accepted for the Department

Richard L. Rowley
Department Chair, Chemical Engineering

Accepted for the College

Alan R. Parkinson
Dean, Ira A. Fulton College of Engineering
and Technology

ABSTRACT

LASER LEVITATION OF SOLID PARTICLES FOR COMBUSTION AND GASIFICATION APPLICATIONS

Skigh E. Lewis
Department of Chemical Engineering
Doctor of Philosophy

This dissertation details theoretical and experimental work in the development of a novel combustion diagnostic: laser levitation of solid particles. Theoretical analyses of the forces involved in the suspension of solid particles in a laser beam provide a comprehensive description of the levitation mechanism. Experimental work provides extensive observations and data that describe each of the forces involved, including results from detailed models. Theoretical models establish that a free-convective drag force, light scattering, photon momentum, and other minor forces contribute to the trapping mechanism. The theory quantitatively predicts particle temperature and magnitudes of each of the forces involved. Experimental measurements contain significant scatter, primarily due to the difficulty of making measurements on these very small particles. However, the best estimate trends of the measurements agree well with

the predicted behavior despite the scatter. Computational fluid dynamics (CFD) predictions of the free-convective drag force qualitatively agree with published experimental values.

The technique represents a tool for studying combustion and gasification of single, micron-sized, solid particles. Biomass fuels and coal (among many others) provide experimental demonstration of particle suspension. The system suspends particles near the focal point of a visible-light laser, allowing continuous monitoring of their size, shape, temperature, and possibly mass. The Particle Levitation Model (PLM) establishes the trapping mechanism using data from three submodels: an energy balance, a drag force model, and a photon force model. Biomass fuels provide experimental demonstrations of particle levitation under a variety of conditions that illustrate each of the primary levitation mechanisms.

Several different trapping techniques provide single-particle data in literature, including optical tweezers and electrodynamic levitation. However, optical levitation of opaque particles is a relatively new technique and, although less-well understood, provides a potentially powerful novel diagnostic technique for single-particle combustion investigations. The diagnostic consists of a solid-state laser, a high-speed color camera, an infrared camera, and a variety of optics. All experimental data are obtained optically, including particle dynamics, size and shape, and particle temperature. Thus, this technique enables the *in situ* investigation of micron-sized, solid particles under conditions similar to commercial combustion and gasification processes.

ACKNOWLEDGEMENTS

This work is dedicated to my beautiful wife, Berkley, for her continuous love, support, and encouragement and for her tremendous patience.

I would also like to thank my incredible family for their support and counsel throughout my education, especially Mom, Dad, and Grandpa. Special thanks also to my advisor, Larry Baxter, and to Thomas Fletcher, Kenneth Solen, Justin Peatross, Dallin Durfee, Brad Damstedt, David Dunaway, Shrinivas Lokare, and numerous undergraduate students.

CONTENTS

List of Tables

List of Figures

Nomenclature

a – direction of laser propagation
A – cross-sectional area
A_{beam} – beam cross-sectional area
$A_{p,cs}$ – particle cross-sectional area
$A_{p,s}$ – particle geometric surface area
α – sensor response correction factor
Bi – Biot number
β – coefficient of volume expansion
c – speed of light in a vacuum
cw – continuous wave
C_D – drag coefficient
C_{ext} – extinction cross-section
C_p – heat capacity
C_{sca} – scattering cross-section
d_b – beam diameter
d_{eff} – effective diameter
d_p – particle diameter
D – beam diameter
DN – pixel value
EDB – electrodynamic balance
ε – emissivity
f – focal length
F_D – drag force
F_{drag} – drag force
F_{mg} – particle weight
F_{photon} – photon force
F_{ph_r} – radial photon force
F_{ph_z} – axial photon force
Φ_p – particle properties
g – asymmetry vector
Gr – Grashof number
h – convective heat transfer coefficient
h – Planck’s constant
He-Ne – helium-neon laser
ΔH_r – heat of combustion
I_{inc} – incident laser intensity
IR – infrared
J – asymmetry factor
k_g – gas thermal conductivity
k_p – particle thermal conductivity
K – Kelvin
Kn – Knudsen number
K_{SL} – coefficient of thermal slip
LP – long pass
λ – wavelength
m – mass
M – molecular weight
μ_g – gas viscosity
P – pressure
P_L – laser power
PLM – Particle Levitation Model
q_{rxn} – reaction rate
Q_{abs} – absorption of laser light
R – ideal gas constant
Re – Reynolds’ number
r_c – radial distance of particle center from beam center
r_p – particle radius
ρ – density
ρ_g – gas density
SEM – scanning electron microscope
$S.G.$ – specific gravity
S_L – function of spatial parameters that describes the beam shape
SP – short pass
S_{RF} – sensor response function
σ – Stefan-Boltzman constant
T – temperature
T_p – particle surface temperature
T_∞ – ambient gas temperature
τ – transmission curve
v – velocity
ν – kinematic viscosity
W – watts
ω_o – beam waist or radius of focal point

1 Introduction

It is difficult to overstate the importance of combustion to the world. In 2003, combustion sources accounted for about 85% of energy generated both in the United States and throughout the world [1, 2]. Although the amount of energy derived from nuclear and renewable sources, such as solar, wind, tidal, and biomass, is increasing, the world continues to depend almost entirely upon fossil fuels (coal, petroleum, and natural gas). Projections of the diminishing supply of these fuels, in particular natural gas and petroleum, prompt their conservation and further explorations into alternative fuels and processes. Furthermore, CO_2 and other pollutant emissions combined with energy security issues call to reduce dependence on fossil energy [3]. Nevertheless, the demand for energy continues to rise, even in the face of such appeals.

In short, the challenge is to maintain (and even increase) the world's fuel supply while decreasing the pollutant and greenhouse gas emissions and conserving our limited supply of fossil fuels. Various options can alleviate these problems; however, because less than 4% of our energy in the U.S. comes from biomass sources (with a similar trend worldwide) [4, 5], increasing the use of biomass fuels/sources may be the most feasible solution. Biomass fuels, including wood, black liquor (by far the largest non-hydro source of renewable energy in the U.S. [6]), straws, grasses, etc., may provide the supplement to fossil fuels and can be CO_2 neutral when properly implemented. However, biomass fuels differ greatly in composition and other properties from fossil fuels. Therefore, each of these fuels must be individually characterized to determine properties such as reactivity, swelling, ash content and composition, etc. [3].

The current techniques used to determine fuel properties provide relatively accurate information about reactivity, mass loss versus time, etc. However, none of these techniques is able to follow the combustion of a single particle through its entire combustion process. Drop-tube reactors take “snapshots” as each particle passes given points, measuring particle temperature, mass loss, size, and velocity. Thermogravimetric analyzers measure mass loss versus time with high resolution and can analyze the products of the given fuel reacting under specified heating rates. Electrodynamic chambers enable measurement of forces acting on single particles under various conditions [7-10], but particles lose their charge when heated above about 1200 K and, thus, high-temperature combustion experiments are not possible with electrodynamic levitation.

Some examples of particles of interest in single-particle investigations are pulverized coal, biomass, ash, energetic materials, and metals, each of which plays a role in commercial combustion processes. Therefore, single-particle investigations relate to a wide variety of combustion applications. Understanding single-particle combustion is fundamental to our understanding of combustion processes, which then enable better characterization of fuel properties and evaluation of fuel viability.

This discussion documents the development of a novel technique to characterize fuel properties. This technique is of interest for determining fuel properties and other particle properties even in the absence of renewable energy issues. This effort develops diagnostic techniques to investigate combustion of single particles of wide-ranging types (fossil, renewable, metallic, etc.) through optical levitation and trapping techniques.

Optical trapping methods manipulate cells and microscopic organisms in aerosol and biological research [11]. Related techniques measure changes in particle size, temperature, and mass throughout combustion. This work applies optical trapping procedures to develop a noninvasive system that supplements current methods used to characterize fuel properties.

1.1 Summary of Objectives

This project has three major objectives:

1) Describe a comprehensive mechanism for optical trapping of absorbing particles;
2) Observe and model size and temperature of particles that may be studied using this technique;
3) Develop *in situ* diagnostic techniques for single particle combustion analysis.

This research falls into three tasks corresponding to each of the objectives listed above. Descriptions of each of these tasks appear.

1.2 Task 1: Particle Levitation Model

The first task includes the development of a detailed, quantitative model that describes the levitation mechanism of opaque particles. This detailed model is referred to hereafter as the Particle Levitation Model or PLM. To understand the levitation mechanism more accurately, the Particle Levitation Model predicts the maximum particle size that may be levitated as a function of laser power and particle properties. This prediction includes estimates of particle diameter, surface temperature, and mass as well as the forces acting upon the particle. These predictions are essential to understanding the trapping mechanism and to design experiments. This model consists of three submodels. The first is an energy balance to predict particle surface temperature as a function of particle and surrounding fluid properties and laser power. The second submodel uses results from Fluent to predict the drag force incident on the particles due to the induced natural convective flow. The third submodel uses results from a scattering code to predict the photon force upon the particles due to absorption and scattering of incident laser light. Together, these submodels quantitatively describe the mechanism for optical trapping of opaque particles. The details of this model appear in the results section.

1.3 Task 2: Data Collection and Modeling

The second task involves data collection to validate predictions. Biomass particles are of primary interest; however, other particles are also used to further validate results. Particles are suspended within a chamber that serves to reduce disruptive air currents. Once trapped, a laser heats the particles to induce combustion. The independent variables include particle composition, laser intensity, laser orientation, and chamber pressure and gas composition; the dependent variables are particle size and temperature. *In situ*, non-contact, optical diagnostics provide all validation data. An IR camera measures surface temperature using a two-color pyrometry technique; a high-speed, color camera collects images suitable for determining size and shape. The experimental methods section details each of these techniques. This task provides the raw data, i.e. particle size and surface temperature that validate the proposed trapping mechanism and the Particle Levitation Model.

1.4 Task 3: Diagnostic Tool

The final objective of this work is to demonstrate the use of this system as a diagnostic tool that measures particle diameter, surface temperature, and mass. Such primary measurements find application to many particle conversion systems, such as particle reaction kinetics as a function of pressure and gas composition. Successful development of this technique may prepare a new avenue for experimental particle reaction experiments that are easier, more accurate, and less costly than current techniques. This *in situ* diagnostic system allows characterization of fuel properties, namely reaction kinetics, and yields their temperature and pressure dependencies and particle dynamics as a function of time during combustion. The ability to perform fuel characterization on any fuel with a noninvasive system will expedite fuel characterization and allow materials to be evaluated with respect to their viability in energy generation.

The following section contains a summary of the background and literature review for this project. The experimental methods and equipment are then detailed, followed by a summary of the results and conclusions.

2 Literature Review and Background

Extensive optical trapping work began in the 1970s. These techniques evolved and are currently used in various investigations of very small particles, aerosols, and cells. This section presents the development of optical trapping of both nonabsorbing (transparent) and absorbing (opaque) particles. Research has also established the forces incident upon trapped particles. A brief analysis of these forces is included. Finally, a brief discussion reviews the combustion application of these techniques.

2.1 Levitation/Manipulation of Nonabsorbing (Transparent) Particles

The first optical levitation (or optical trapping) experiments were performed with transparent particles. This type of levitation operates on the principle of photon momentum transfer [11-13]. Photon momentum was proposed by Planck and later used by Einstein to explain the photo-electric effect [12], the paper for which Einstein later received a Nobel prize. A photon of wavelength λ carries momentum h/λ, where h is the Planck constant, and this momentum partially or completely transfers to the particles when photons reflect or refract. This momentum is often referred to as light, radiometric, or radiation pressure. Under normal conditions, the momentum transferred by even a very large number of photons is negligible; however, for small particles (on the order of several microns) this force is significant relative to the particle's weight. For a 1 μm diameter particle with unit specific gravity, the gravitational force is about 10^{-15} N. With laser light of sufficient intensity, the particle weight can be balanced by the photon momentum force [11, 12].

Optical trapping has been performed with transparent particles on the order of nanometers to several microns in diameter. This phenomenon arises from geometric-optics arguments, as shown in Figure 2-2. Rays a and b refract through a sphere, producing forces F_a and F_b. There are two components to the net force, a transverse component, F_{tr}, sometimes referred to as the gradient force, and an axial component, F_{ax}, sometimes referred to as the scattering force. As seen in Figure 2-2, the net force actually pulls the sphere into the center, high-intensity region of a Gaussian profile (TEM_{00}) beam [11, 14]. The laser mode patterns are summarized by Figure 2-1 [82].

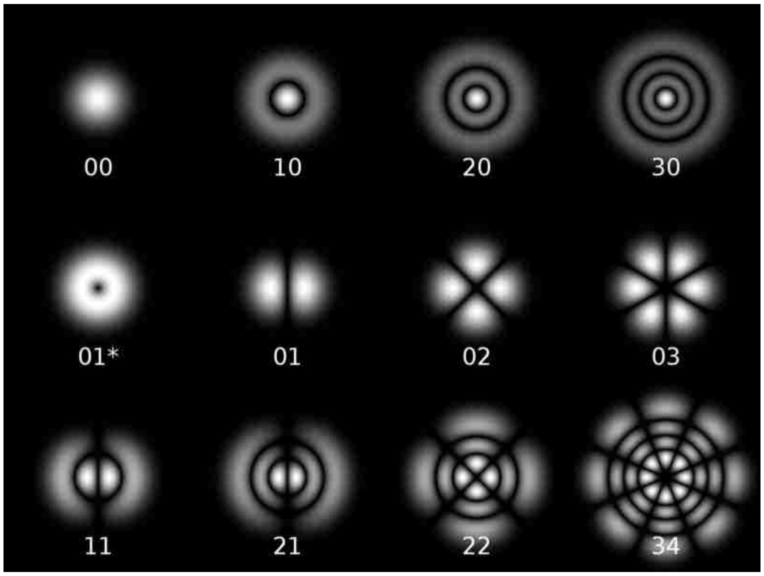

Figure 2-1: Cylindrical transverse mode patterns (TEM_{pl}) [82].

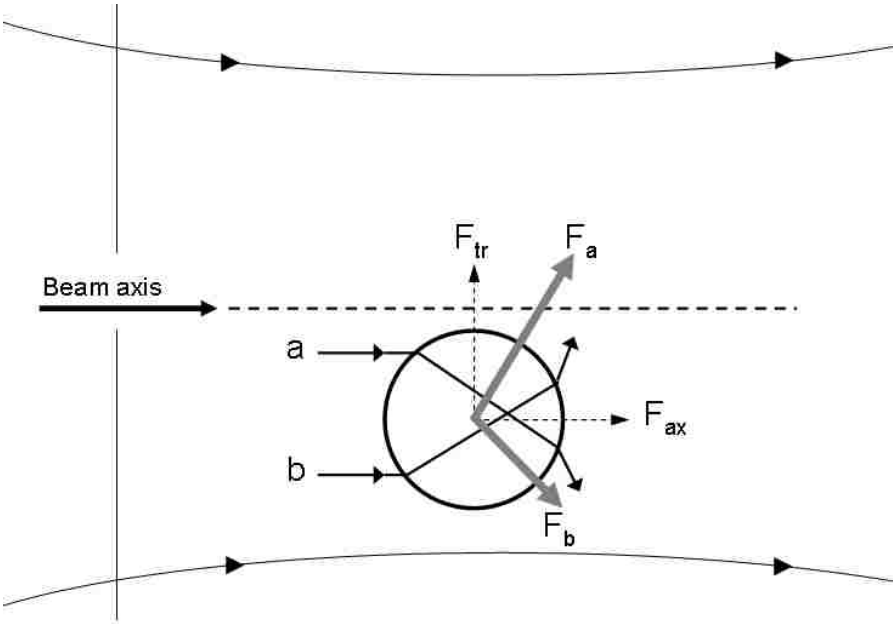

Figure 2-2: Diagram of resultant forces in an optical trap for a transparent particle in a Gaussian beam (TEM_{00}) [11, 14].

In the focus of a Gaussian beam, the maximum intensity occurs along the beam axis and decays with increasing radial distance. The intensity also decays with increasing axial distance from the beam waist (focal point). A particle moving away from the focus in any direction feels a force pushing it back to the focal point. This is an optical trap. It is a three-dimensional optical trap if the gradient force dominates the scattering force. If the scattering force is larger than the gradient force, optical trapping can still be performed by directing the beam vertically so the scattering force can be balanced by gravitational forces [12].

Ashkin was the first to report optical levitation of nonabsorbing (transparent) particles [15, 16]. This initially used a single, vertically-directed 514.5 nm continuous wave laser beam at 100-500 mW in air at pressures down to ~1 torr. He reported the manipulation of 15-25 µm glass spheres, and attributed this phenomenon to restoring forces that are generated when the beam is refracted by the glass sphere. These restoring forces, now referred to as the gradient and scattering forces, stabilize the spheres just above the focal point of the beam. In later work, Ashkin reported the levitation of hollow spheres in two distinct stable regimes, one above the focus and one below [17]. He also noted that hollow-sphere levitation requires greater laser power than solid spheres of the same weight due to differing refractive properties of the spheres. The two stable regions are explained by the fact that the laser beam creates the levitating forces on the spheres. These forces are directly proportional to the intensity of the beam. For any given focal length, the beam intensity increases closer to the focal point. Therefore, a particle will experience a maximum force when the beam diameter is equal to the particle diameter. Thus, given the symmetry of the focal point, particles will experience two maxima in beam intensity and, consequently, two stable trapping regions. In addition to this discovery, Ashkin also determined that lenses with shorter focal lengths gave improved trapping stability relative to longer focal lengths [17].

After Ashkin reported the trapping of nonabsorbing particles, other researchers extended his work to obtain expressions for the scattering and gradient trapping forces on micron-sized particles using electromagnetic theory [18-20]. These correlations show the dependence of each force on laser frequency, beam angle, position and nature of the particle in the beam focus. For nonabsorbing particles that are small compared to the laser wavelength, trapping at near-resonant absorption frequencies allows trapping strengths up to 50 times stronger than at non-resonant frequencies and also improves trapping specificity for optical tweezers [18].

Ashkin continued his work to determine what factors most significantly affected the stability of trapped particles. In 1976 he reported the observation of transparent particles trapped under high vacuum (~10^{-6} torr) [21]. Before this work, particles could be levitated down to 1-10 torr. Below 1 torr they were destabilized by residual radiometric forces – essentially thermal gradients around the particle. These forces become negligible at high vacuum conditions and allow the particles to be trapped solely by radiation pressure. To control the stability of trapped particles, Ashkin later developed an electronic feedback system that helped to dampen any instabilities [22]. The feedback system detected the location of the particle and manipulated its location by changing the strength of the electromagnetic field in which the particle was trapped. A similar technique would later be used by Zhao *et al.* for stable manipulation and study of opaque particles within an electrodynamic chamber [7].

Various modifications and improvements generalize Ashkin's initial experimental methods. Gahagan observed that it was difficult to isolate a single particle and that trapped particles may be susceptible to damage due to absorptive heating [23]. He lowered the peak beam intensities and was able to successfully isolate and manipulate single particles using an optical vortex trap (generated by a TEM_{01} beam or a computer-generated hologram). Ashkin's design also had difficulty trapping asymmetric particles, possibly because the peaks in the trapping force may not exist for irregular particles [24], or because the proper beam structure was not used. However, MacDonald *et al.* demonstrated trapping and manipulation of low-index (index of refraction) particles and rodlike samples using an interference pattern, generated by an interferometer [25]. Most notably, with this interference pattern, he trapped rods and hollow spheres simultaneously – an experimental first..

In 1997, Ashkin summarized his work on optical trapping and discussed the possible applications of optical levitation [11]. He suggested such applications as light scattering experiments to investigate the effects of numerous trapped particles and different laser modes on scattering patterns. Optical levitation performed in liquids, known as optical tweezers, prove useful in biological studies to manipulate submicron cells and organisms in scenarios where gravity plays a small role relative to the effects of Brownian motion. Optical trapping techniques have also been used extensively in aerosol research to investigate physical and chemical properties, including scattering properties that affect humidity and ozone reactions [26]. Other work has been cited in physics, chemistry, and microchemistry in which optical levitation and optical tweezers have been used to investigate the dynamics of small droplets and particles under otherwise impractical conditions.

The work done with transparent particles and optical tweezers has been almost exclusively for biological and aerosol research. This research did not consider the more hostile conditions in combustion applications except for possibly studying aerosols resulting from combustion processes. Nevertheless, this work laid the foundation for later work with opaque particles, which indeed relate to combustion research.

2.2 Levitation of Absorbing (Opaque) Particles

Lewittes *et al.* were the first to report optical levitation of opaque particles (~20 μm glycerol spheres) [27]. Unlike levitation of transparent particles, which operates almost exclusively on the principle of photon momentum transfer (or photon pressure), levitation of opaque particles involves several forces, as will be discussed in detail later. Because photon pressure plays a lesser role, significantly smaller laser intensities are required than those required for levitation of nonabsorbing particles. Lewittes proposed that a radiometric force suspends opaque particles in addition to photon momentum transfer. He was the first to propose that downward directed beams could suspend opaque particles, which he termed reversed levitation. Lewittes suggested that absorbing particles will seek an intensity minimum, and experimented with doughnut mode beams (TEM_{01} rotated rapidly) to demonstrate that the particles were stably suspended in the center of the beam where the intensity was at a minimum. Pluchino observed similar behavior with spherical carbon particles (1.5-8 µm) but suggested that diffraction patterns near the focal point cause an intensity minimum where the particle can stably rest [28]. He discounted the effects of convection caused by heating the walls of the chamber; however, he failed to account for the effects of convection caused by heating the particle itself.

Huisken expanded on the concepts introduced by Lewittes by attributing particle dynamics to the concept of thermal creep, a force due to a temperature gradient through the particle [29]. Thermal creep creates a higher pressure on the warm side of the particle than on the cold side. He demonstrated the levitation of metal oxide particles (copper and brass, <20 µm diameter) with a Gaussian beam (TEM_{00}). Although particles may seek an intensity minimum as proposed by Lewittes, Huisken suggested that the combination of thermal creep and photon pressure balance gravity and enable levitation. This leads to an analysis of the forces involved in levitation of opaque particles.

A research group in the Physics and Astronomy department at Brigham Young University conducted investigations into the mechanism of optical trapping of opaque particles. Two students under the direction of Justin Peatross completed undergraduate thesis work on this subject, both of whom hypothesized that the trapping mechanism is driven primarily by intensity minima within the beam [30, 31]. Bellville proposed that intensity minima may be created within the beam by manipulating optics to create a low-intensity cavity within which the particles rest, stably suspended. The work done by Bliss theorizes that "dark pockets" naturally exist within the beam due to lens and laser aberrations. These "dark pockets" would create similar low-intensity cavities that Bellville proposed be manually generated. The work done by Peatross' group has helped to significantly advance the fundamental understanding of the opaque particle trapping mechanism.

2.3 Forces in Optical Levitation of Opaque Particles

An overall force balance on an opaque particle reveals five forces that may influence the trapping mechanism: gravity, photophoresis, thermophoresis, thermal transpiration, momentum transfer of the laser light (photon force), and the free convection drag. Particle weight is constant, assuming that the particle is inert during trapping, and proportional to the diameter of the particle (d_p) cubed. The other forces will be described in detail in the following sections.

2.3.1 Photophoresis

Photophoresis acts on the particle due to non-uniform heating of the particle surface from an electromagnetic source [9, 32-34], a laser in the case of optical trapping.

The side of the particle on which the beam is incident may become hotter than the opposite side (depending on particle rotation and thermal conductivity). Gas molecules rebounding from the hotter side of the particle have greater momentum than those rebounding from the cooler side, imparting a net force in the direction of the cooler side. Various expressions for the photophoretic force appear in the literature [9, 35] and the expression developed by Zhao [9] is given below (Equation 2-1).

$$F_{pp} = \frac{-16\pi \cdot R \cdot J \cdot K_{SL}}{P \cdot M \cdot Q_{abs}} \cdot \frac{\left(T_p - T_{\inf}\right) \cdot \mu_g^2 \cdot k_g}{k_p} \tag{2-1}$$

Where R is the ideal gas constant, P is the pressure, M is the gas molecular weight, Q_{abs} is the absorption of laser light, μ_g is the gas viscosity, T_p is the particle temperature, k_g is the gas thermal conductivity evaluated at the film temperature, and k_p is the particle thermal conductivity. J is an asymmetry factor describing the asymmetry of radiation absorption within the particle that generates a temperature distribution through the particle. K_{SL} is the coefficient of thermal slip and should be in the range 0.75-1.169; a value of 0.75 assumes all molecules colliding on the particle’s surface undergo a mirror reflection and a value of 1.169 assumes total diffusive reflection. This equation indicates that the photophoretic force is independent of particle size, which was experimentally verified by Zhao *et al.* [7]. It is also linearly dependent on the difference between the particle and surrounding gas temperature.

2.3.2 Thermophoresis

Thermophoresis affects small particles (smaller than ~100 µm) when a temperature gradient exists in the bulk gas creating a force in the direction of the lower temperature. It is necessary to define here the distinction made in this work between photophoresis and thermophoresis. As mentioned in the previous section, photophoresis arises from non-uniform heating of a particle's surface by an electromagnetic source; the thermophoretic force arises from a temperature gradient within the surrounding gas. The molecules in the higher temperature region move with greater kinetic energy and the particles naturally diffuse towards the lower temperature region [36]. It is unclear the extent to which the thermophoretic force affects particles in optical trapping because the higher temperature region is confined to the particle and the gas immediately surrounding the particle. Therefore, a sufficient temperature gradient in the gas may not exist for the thermophoretic force to be significant. A more detailed discussion of thermophoresis with respect to optical trapping follows in the Results section.

2.3.3 Thermal Transpiration

Thermal transpiration is the major force operating in Crookes' radiometer [37-39]. It is essentially an edge effect. When there is a temperature gradient across an object, it creates a force in the direction of the colder side. Crookes' radiometer operates at vacuum pressures, but Lu suggests that the optimal pressure increases as the characteristic size of an object decreases [40]. However, Lu and Scandurra make it clear that thermal transpiration would only be significant at ambient pressure for objects on the nanometer scale [40, 41]. The fact that thermal transpiration is primarily an edge effect operative only at vacuum pressures or on nano-scale particles at ambient conditions is what distinguishes thermal transpiration from thermophoresis and photophoresis.

2.3.4 Photon Force

The momentum transfer from the incident laser light (photon force) is more significant than either the photophoretic or thermophoretic forces. Each photon carries momentum equal to h/λ, where h is Planck's constant and λ is the wavelength of the incident light [42]. When monochromatic light, such as that from a laser beam, focuses upon a small particle, the cumulative momentum of the photons creates a force large enough to influence particle motion parallel to the beam axis. Equation 2-2 gives the expression for the force due to the momentum transfer of the laser light, hereafter referred to as the photon force.

$$F_{photon} = \varepsilon \cdot \frac{P_L}{c} \cdot \frac{A_{p.cs}}{A_{beam}} \tag{2-2}$$

Where ε is the particle emissivity at the laser wavelength, P_L is the laser power, c is the speed of light in a vacuum, $A_{p,cs}$ is the particle cross-sectional area, and A_{beam} is the beam cross-sectional area. Photons can also carry angular momentum [43]. Absorbing particles trapped and rotating in a plane-polarized donut mode (TEM_{01}) beam actually change their angular velocity depending on the polarization of the incident light.

2.3.5 Free Convective Drag Force

As a particle in the focus of a laser beam heats up, a free convective flow develops around the particle and creates a drag force on the particle that acts upward (more precisely, opposite the direction of gravity) regardless of the beam orientation. As will be shown hereafter, this free-convection-induced drag force is the largest upward force on the particle and the most important force in the optical trapping mechanism. Other researchers have noted the importance of the induced drag force to the optical trapping mechanism. Spjut *et al* stated, "When a particle is heated in a stagnant atmosphere, a natural convective flow is established around the particle. The flow does not materially affect heat transfer (The Grashof number is <<1**),** but the drag from the flow does exert a measurable force on the particle [44]." In a later investigation, Huisken stated that "heating is essential for the levitation of absorbing particles [29]." Many researchers have worked with electrodynamic chambers that allow the isolation of the free-convective drag force from the other forces acting on the particle and its subsequent measurement [7, 8, 10, 45, 46]. Some have developed correlations for the drag force on a spherical particle due to free convection. Equation 2-3 is the correlation developed by Dudek *et al*. with a discrete least squares method, valid over the range $0.004 < Gr < 0.5$ for $Pr = 0.72$ [46]:

$$\log(C_D) = 1.25 + 0.31 \cdot \log(Gr) - 0.097 \cdot [\log(Gr)]^2 \qquad (2\text{-}3)$$

Where the Grashof number, Gr, and the drag force, F_D, are defined by Equations 2-4 and 2-5, respectively:

$$Gr = g \cdot \beta \cdot (T_s - T_\infty) \cdot {r_p^3}/{\nu^2} \qquad (2\text{-}4)$$

$$F_D = {1}/{2}\,\rho \cdot v^2 \cdot A \cdot C_D \qquad (2\text{-}5)$$

C_D is the drag coefficient, ρ is the gas density, v is the gas velocity due to the free-convective flow, A is the cross-sectional area, β is the coefficient of volume expansion [K^{-1}], r_p is the particle radius, and ν is the gas kinematic viscosity.

Equation 2-6 is the drag force correlation developed by Zhao [7]:

$$F_D = 3\pi \cdot d_{eff} \cdot \mu_g \cdot v \qquad (2\text{-}6)$$

Where d_{eff} is the effective diameter of the particle, which is larger than the actual diameter because of the boundary layer due to the free-convective flow.

The expression from Dudek *et al.* gives lower drag force values than the correlation developed by Zhao, and hence does not seem valid in the range of interest for optical trapping. For a 40 µm particle at 900 K, the correlation by Zhao predicts a drag force of 4.82e-10 N, which is about 95% of the gravitational force on a black liquor particle of this size.

2.4 Electrodynamic Levitation

The electrodynamic balance (EDB) suspends charged particles in an electrodynamic field as a means of studying single particle dynamics, combustion kinetics, and incident forces under a range of conditions. The general theory and operation is described in papers by Bar-Ziv, Sarofim, and others [8, 47-49]. In 1909 Robert Millikan and Harvey Fletcher first applied these principles in the famous Millikan oil-drop experiment to determine the charge of an electron [50]. Particles are charged and usually suspended between three electrodes. A position controller maintains the particles at a fixed position by adjusting the voltage to the electrodes. The EDB allows continuous measurement of particle size, weight, and temperature. It has also been used as a tool to isolate single particles and measure their combustion properties (ignition temperature and reaction kinetics), transport properties (heat capacity and thermal conductivity), and to develop correlations for photophoretic, thermophoretic, free-convective drag, forced-convective drag, and mixed-convective drag forces [7-9, 34, 45, 47, 49, 51].

With regard to combustion studies, the EDB initially targeted single-particle combustion reactions similar to those that are the focus of the present work. However, the EDB cannot study combustion above about 1200-1500 K, depending on particle composition, because of the loss of particle charge [48, 52-54]. This prevents the investigation of high-temperature combustion kinetics.

2.5 Combustion Application

Work done to date with optical levitation of both transparent and opaque particles has investigated the trapping phenomena and its operating mechanism. Glycerol spheres (~20 µm) [27], spherical carbon particles (1.5-8 µm) [28], and metal oxide particles (<20 µm) [29] are a few examples of opaque particles that have been studied to develop the optical trapping mechanism.

The preceding research was limited to investigations of particle dynamics under nonreacting conditions or low-temperature reactions. The system proposed for this project utilizes results from previous work and further applies it to a reacting particle scenario. No previous work has successfully studied a single particle through an entire combustion event. This provides an opportunity to study particle reaction kinetics under a range of gas pressures and compositions.

3 Experimental Methods

3.1 Equipment

A Coherent Verdi V10 Nd:YVO_4 cw, frequency-doubled laser operating at 532 nm with variable power output from 0.01-10.5 watts traps particles for this diagnostic. A 25.4 cm diameter, 4.0 cm focal length lens focuses the beam within a Plexiglas enclosure, the latter inhibiting rapid changes in air flow around trapped particles that would otherwise convect the particles out of the beam (Figure 3-1 and Figure 3-2).

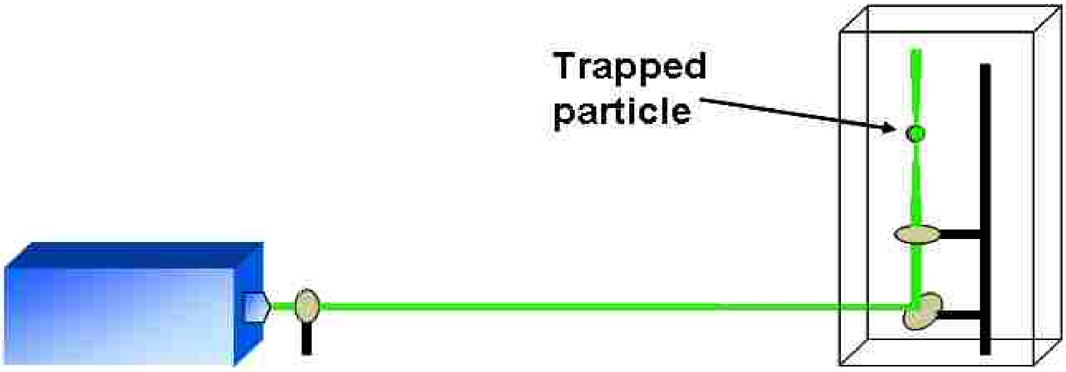

Figure 3-1: Diagram of configuration to trap particles with 532 nm laser.

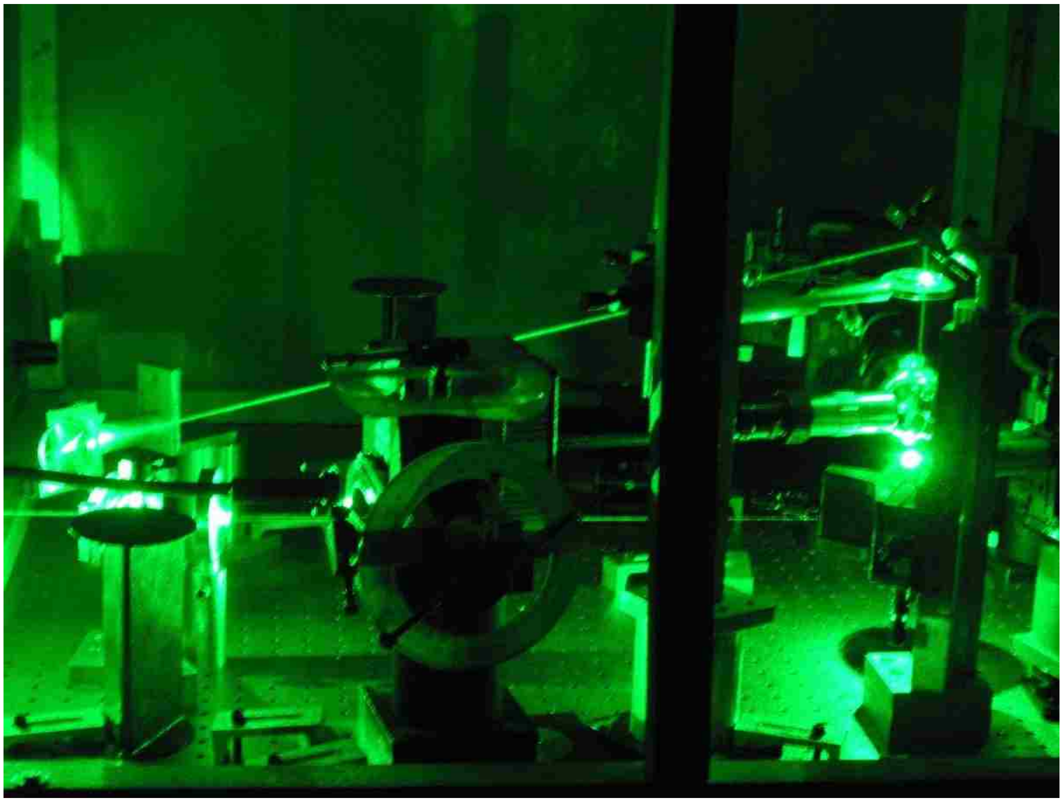

Figure 3-2: Actual experimental setup used to trap particles with 532 nm laser showing mirror directing beam upwards and the trapping lens.

This system represents the primary facility used in this project. Although these figures show the beam directed vertically upward, beams oriented in any direction successfully trap particles, as discussed in more detail in the Experimental Observations section. Two cameras provide experimental data: 1) The Photron Fastcam 1024 PCI camera, which has a resolution of 1024x1024 pixels and a maximum frame rate of 2,000 frames per second (fps) at full resolution and 109,500 fps at reduced resolution; and 2) The FLIR SC6000 infrared camera, which has an indium antimonide (InSb) sensor, 640x512 resolution, and a maximum frame rate of 120 fps. The Photron camera is used in conjunction with an Edmund Optics M Plan Apo 50X Mitutoyo objective lens that images the particles with a 1.3 cm working distance and a 30-60 µm field of view.

A 4X microscope lens for the FLIR camera provides a field-of-view of approximately 3.65 mm x 2.92 mm with a 1.5 cm working distance. The combination of these two cameras, both arranged orthogonally to the beam, allows measurement of particle size, shape, position relative to beam focus, and temperature.

3.2 Setup

From the laser aperture, the beam passes through a beam splitter that transmits about 22.5% of the beam power and reflects the remaining 77.5%. The transmitted portion passes through a 10 cm focal length lens that expands the beam before reaching the trapping lens. This beam expansion creates a smaller spot size at the focal point (Equation 3-1), provided that the beam does not become larger than the lens diameter.

$$2\omega_o = \frac{4\lambda}{\pi} \cdot \frac{f}{D} \tag{3-1}$$

Where $2\omega_o$ is the beam spot size, λ is the wavelength, f is the lens focal length, and D is the diameter of the beam at the lens or the lens diameter if the beam is larger than the lens. Experimental observations indicate that particles are easier to trap and maintain trapped with shorter focal length lenses/smaller beam diameters. After the expanding lens, the beam is directed upwards by a first-surface mirror, after which it is focused by the 4.0 cm focal length lens (hereafter referred to as the trapping lens).

The portion of the beam reflected by the initial beam splitter heats the particles to induce particle combustion. Two mirrors accomplish this. The first mirror angles the beam upward toward the second mirror, which directs the beam downward through a 10 cm focal length lens. This lens focuses the beam upon the suspended particles. This beam and mirrors do not appear in Figure 3-1. In practice, this beam is also split and directed to the particle from symmetric positions to ensure uniform particle heating.

3.3 Particle Trapping

A needle coated with particles and passed through the beam near the focal point consistently produces suspended particles, one or more of which commonly stabilizes in the beam within the Plexiglas enclosure (Figure 3-3).

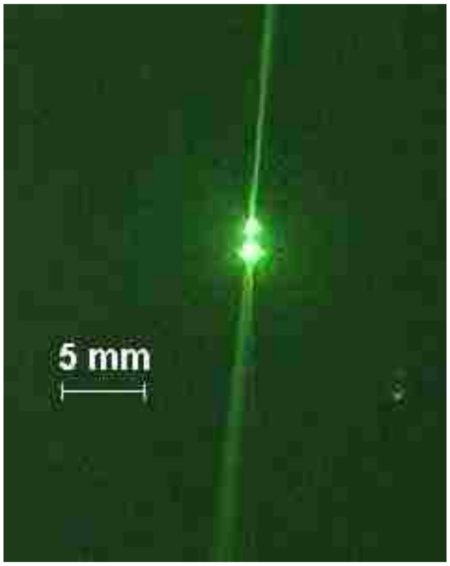

Figure 3-3: Optically trapped black liquor particles.

As mentioned previously, a focused beam may be oriented in any direction to successfully trap particles. A trapped particle denotes a particle with indefinitely stable position and that follows the beam even as the beam moves slowly in any direction. The limitation on the speed of this motion arises from drag forces that destabilize the particle if the beam moves too quickly.

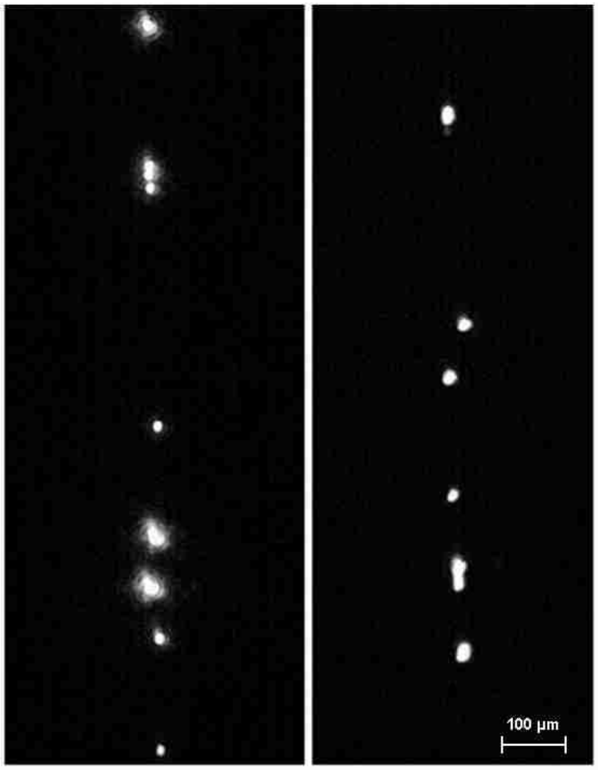

Figure 3-4: Black and white pictures taken with a high speed camera that show trapped black liquor particles at 2 watts of laser power (all particles shown are optically trapped).

Light scattered from dust particles indicates the presence of minor convective flows that do not unduly interfere with particle levitation. While particles trap in beams of many focal lengths, shorter focal lengths provide more stable and robust operation than longer focal lengths. Pictures and video reveal that many particles trap in each trial.

Videos show as many as 8-12 particles stably trapped in the vertical arrangement (Figure 3-4).

3.4 Experimental Observations

This section summarizes several experimental observations that must find explanation in any comprehensive description of particle levitation mechanisms. The following sections explain in greater detail the experimental techniques and theoretical framework developed to quantify these trends and compare them with predictions.

3.4.1 Pressure

Particles levitate in a vacuum chamber with the laser directed in any direction. The approximate low-pressure limit for particle trapping is 1 torr. At pressures less than ambient, particles trap up to several centimeters away from the beam focus on either side of the focal point. However, particles become less stable the farther away from the focal point they are trapped.

Ar^+, Nd:YAG, and Nd:YVO_4 laser beams successfully levitate a variety of particle types (black liquor, aluminum, silver, nickel, iron, magnesium oxide, tungsten, charcoal, carbon black, and graphite) at a variety of pressures (ambient down to about 1 Torr). Vertically upward, vertically downward, horizontal and all other beam directions stably trap particles. Vertical beams propagating upward are the most effective for reasons that will be discussed later. Additionally, while a particle is trapped, the beam can be moved slowly and the particle will follow the path of motion as long as the beam is not obstructed in any way or moved too quickly.

3.4.2 Beam Orientation, Power, and Movement

Particles trap in beams of any orientation, including angled beams, upward, downward, and horizontal beams. Additionally, particles follow the beam if it sweeps slowly from side to side. Particle motion and stability while trapped were observed at ambient pressure (0.842 atm) for each orientation and while increasing and decreasing laser power. Most of the experimental work involved upward-directed beams to keep the forces involved parallel to gravity and symmetric, thus allowing particles to trap with greater stability and simplifying analysis. Similar observations of the particle behavior described here was also observed by Pluchino [28].

Trapped particles seem to be most stable in the vertically upward orientation. Particles move predictably with changes in laser power; they move up with increases in laser power and down with decreases in laser power. In contrast, particles trapped in the horizontal orientation seem to be slightly less stable than in the vertically upward orientation. As laser power increases, particles move in the direction of beam propagation; as laser power decreases, particles move in the opposite direction of beam propagation.

When trapped with the beam directed vertically downward, particle motion is much less steady than that observed with the vertically upward orientation. As power is changed, the net change in force determines the direction that the particle moves. As power increases, particles move downward in the direction of the beam; as power decreases, particles move upward. Additionally, for equal changes in laser power, particles move shorter distances in this orientation than similar particles in the vertically upward and horizontal orientations.

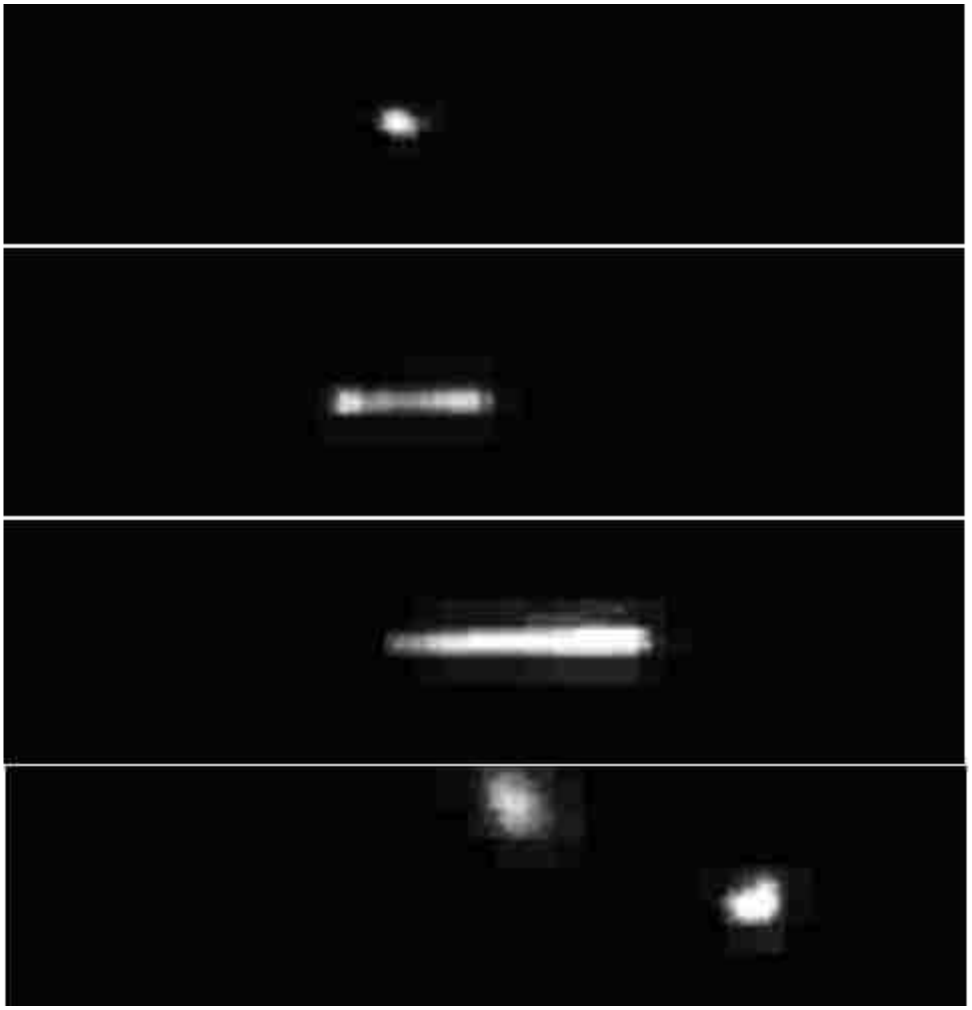

Figure 3-5: Progression of particle oscillating. Each image shows the same particle, except last image, which includes an additional particle (centered). The magnitude of the oscillations captured in these images is about 30-40 µm.

Occasionally particles seem to oscillate or vibrate rapidly regardless of beam orientation. Some oscillate rapidly (30-40 Hz) between two points (frequently separated by 100 µm or more) while trapped (Figure 3-5), suggesting that this behavior is not simply due to Brownian motion. Others pass through the beam and shoot through the focal point in either direction. Such oscillators and shooters are more prevalent at less than ambient pressure, although they may be seen at any pressure with the beam in any orientation. Such behavior may indicate asymmetries in light scattering or surface temperature. In any case, such unstable particles typically exit the beam within seconds, with one or several stably levitated particles remaining in the beam indefinitely.

3.4.3 Types of Particles

Among other variables, particle levitation depends strongly on emissivity and density. Black liquor, a paper-processing byproduct that has been the subject of other investigations in this research group, levitates relatively easily and represents one of the common samples used in these experiments. It has an emissivity (ε) of about 0.8 and a specific gravity ($S.G.$) of about 1.65; 2-8 μm diameter black liquor particles levitate routinely. Alternatively, aluminum particles are much more difficult to trap. Aluminum has an emissivity of about 0.1 and a specific gravity of about 2.7; it is possible to trap aluminum particles, but with greater effort compared to black liquor due to its lower emissivity and higher specific gravity. Silver, nickel, iron, magnesium oxide, tungsten, charcoal, coal, carbon black, graphite, and wood dust all represent samples investigated in this work, with none of these trapped particles larger than 10 μm in diameter.

3.4.4 Stability

With the beam directed vertically upward, many of the larger particles stabilize beneath the focal point, some up to about 1.5 mm below the focus. Generally, particles this far from the focal point seemed slightly less stable than those trapped closer, which was manifested by more frequent oscillations and shifts in position. Occasionally, several particles (>10) would line up vertically within the beam, shifting position in unison with changes in external bulk flow. Of the three types of particles used to demonstrate this technique, black liquor trapped most easily, followed by petcoke ash and then wood dust. This observation is consistent with the proposed mechanism.

3.5 Data Collection Procedures

All data represent optical, remote measurements with the high-speed and IR camera systems. The high-speed camera system determines particle size and shape and allows observation of particle dynamics while trapped and heated. The IR camera system measures particle temperatures using a modified 2-color band pyrometry technique developed specifically for this work; the original color band pyrometry method for temperature measurement was developed separately within this research group [55, 56].

3.5.1 Size Measurement

Once a particle is stably suspended, a He-Ne beam traverses the particle and enters the microscope lens (Figure 3-6 and Figure 3-7). Provided that the particle is in focus, this generates a shadow that is the same size as the suspended particle. The He-Ne laser provides a bright red background that contrasts sharply with the reflected green laser light from the suspended particles (Figure 3-8). The He-Ne beam does not aid in particle suspension; it simply generates a particle shadow that enables size measurement. This contrast enables the researcher to distinguish when the particle is in focus; particles appear larger than actual size when out of focus.

Once in focus, the high-speed camera records three separate images of the particle in sequence as bitmap files. The images are imported into MATLAB®. Typical color cameras display a red, green, and blue value for each pixel; the high-speed camera used in this research records 8-bit images, for which the pixel values have a range of 0-255 pixel counts.

Figure 3-6: Orientation of microscope lens and He-Ne laser for particle size measurements.

For any given pixel, the particle-sizing program written for this procedure sets the red value to zero if the green value is above 38 counts. This removes any red background from the He-Ne beam for pixels that show significant signal above background noise in the green channel. Both green and blue channels are set entirely to zero in the cropped image. The resulting image shows a red background with a dark shadow where the particle was suspended (Figure 3-8). The subroutine determines the perimeter of the particle and then counts each pixel included within the perimeter and determines an effective particle diameter corresponding to a circular cross-section.

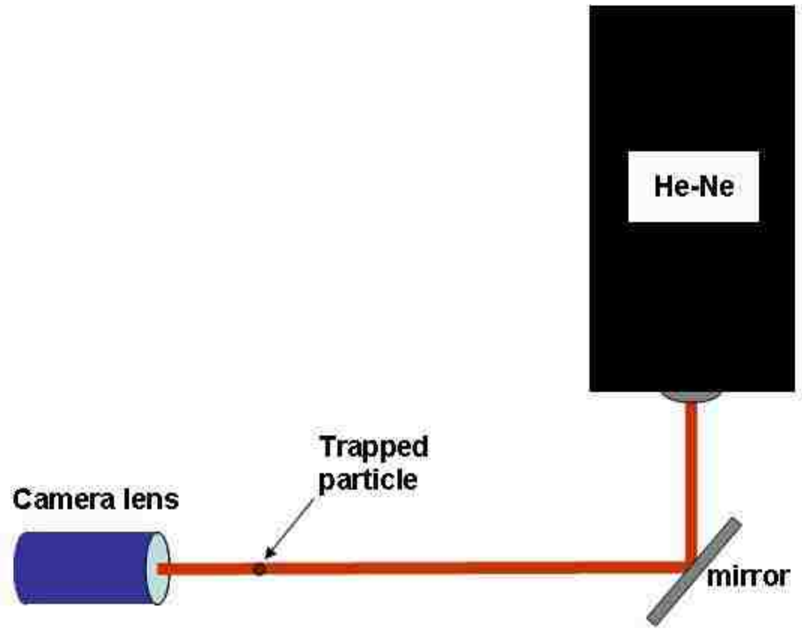

Figure 3-7: Diagram of experimental setup for particle size measurements.

The Fastcam 1024 PCI has 17 µm square pixels from which the overall area is calculated. The values from the three images taken for each particle are averaged to give the final particle diameter. Experimental error seems to increase with increasing particle size due to increased light scattering from larger particles, such as in the last pair of images in Figure 3-8. Without particles of known size within this range, it is very difficult to determine this error accurately.

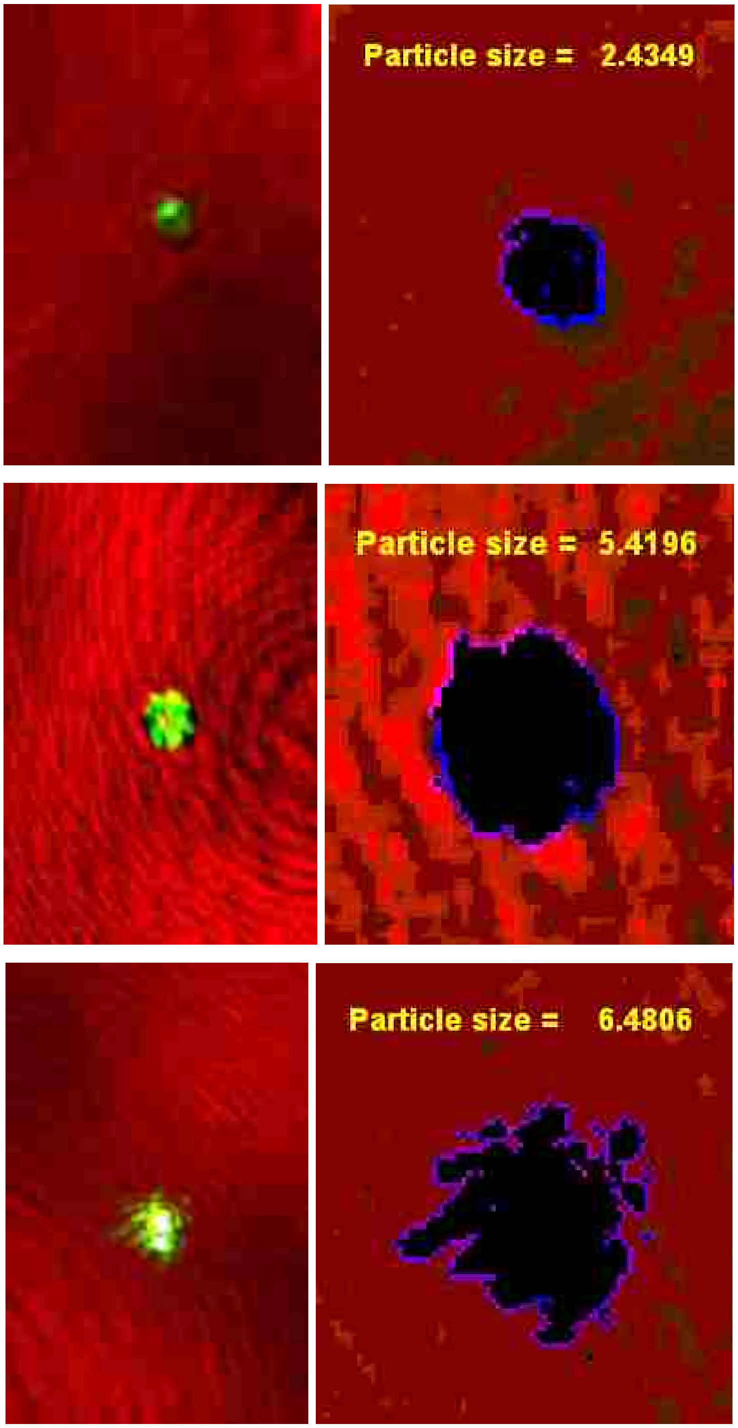

Figure 3-8: Typical images of suspended particles for size determination (each image pair is a separate particle). The left image in each pair is the original cropped image; the right image indicates corresponding particle size in microns after being processed by Matlab.

3.5.2 Temperature Measurement

The FLIR SC6000 infrared camera measures particle temperature. Because the approximate diffraction limit of the camera with the 4X microscope lens is about 6.25 µm, the wavelength range within which the camera is sensitive (3-5 µm) is divided using a high-pass and a low-pass filter. Figure 3-9 shows the transmission curves for the high-pass and low-pass filters. This allows a modified two-color pyrometry method to be employed, which permits temperature measurements on particles smaller than the diffraction limit. This program is included in Section B of the Appendix.

The modified two-color pyrometry method utilizes Equation 3-2, which relates the measured pixel values to the overall energy received by the camera's sensor.

$$DN = \alpha(T) \cdot \varepsilon \cdot \int_{\lambda_1}^{\lambda_2} S_{RF}(\lambda) \cdot \tau(\lambda) \cdot E_b(\lambda, T) d\lambda \qquad (3\text{-}2)$$

$$E_b(\lambda, T) = \frac{C_1}{\lambda^5 \cdot \left[\exp\left(\frac{C_2}{\lambda \cdot T} \right) - 1 \right]} \qquad (3\text{-}3)$$

In Equation 3-2, DN is the measured pixel value, ε is the object emissivity, S_{RF} is the sensor's assumed response function, α is a temperature- and filter-dependent correction factor obtained through calibration that corrects for the difference between the actual and assumed sensor response curves, and τ is the transmission curve for any filters placed between the object and camera lens. Equation 3-3 is Planck's radiation law where λ is the wavelength, T is the temperature, $C_1 = 3.742 \cdot 10^8$ W·µm^4/m^2, and $C_2 = 1.439 \cdot 10^4$ µm·K. The assumed response curve is based upon the response curve submitted in a patent application for the indium antimonide sensor [57].

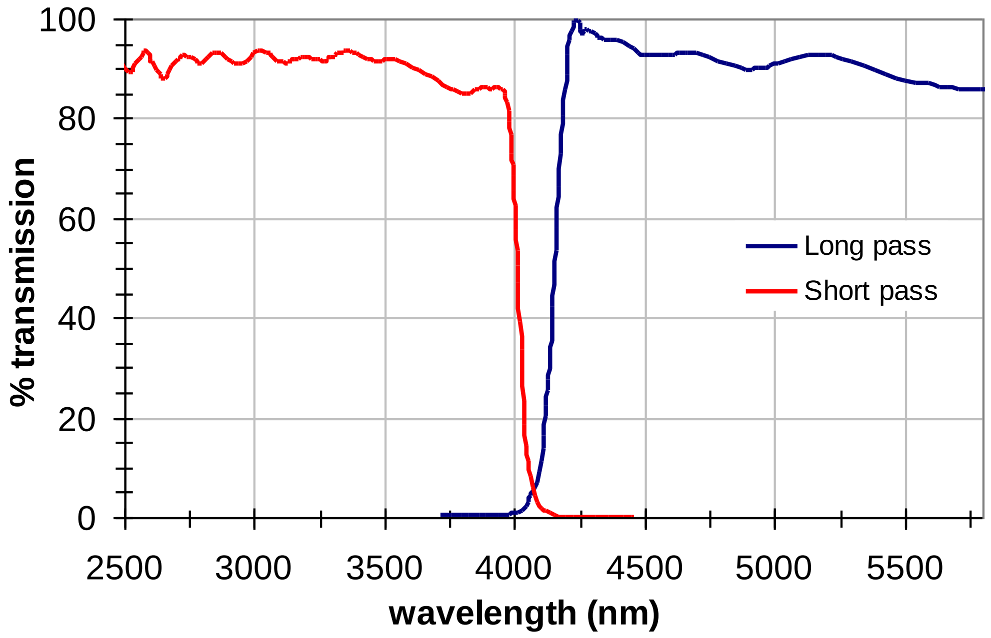

Figure 3-9: Transmission curves for long-pass and short-pass filters used for temperature measurement.

The IR camera and lens were calibrated by placing a 0.0005 inch (12.7 µm) CHROMEGA® thermocouple ($\varepsilon = 0.6$) near the focal point of the laser beam within the camera's field-of-view. Varying laser intensity allowed control of the thermocouple temperature. The IR camera focused upon the heated thermocouple bead and measured the difference between the maximum pixel value across the bead and the average background pixel value corresponding to each temperature.

It is important to measure the difference between the maximum and background values because the background values, and consequently the maximum values, increase as the camera heats up during use. This procedure generated the correction factor α for each filter.

Rearrangement of Equation 3-2 yields the following expression for α.

$$\alpha = \frac{DN(T)}{\int_{\lambda_1}^{\lambda_2} \varepsilon \cdot S_{RF}(\lambda) \cdot \tau(\lambda) \cdot E_b(\lambda, T) d\lambda} \tag{3-4}$$

All variables are known in Equation 3-4 except for *DN(T)*, which is measured for each filter as described in the previous paragraph. The results of this calibration appear in Figure 3-10.

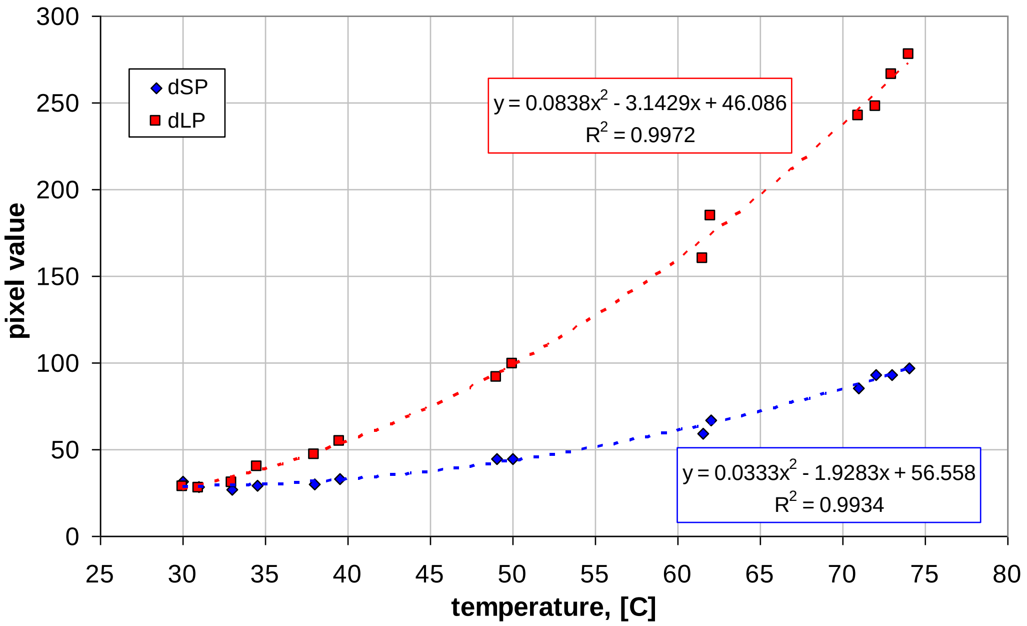

Figure 3-10: Result of LP and SP filter calibration.

The second-order polynomial fits provide expressions for pixel values measured with the respective filters as a function of temperature. The expression for α is then substituted into Equation 3-2 to provide a rigorous expression for pixel values as a function of particle emissivity and temperature.

Once calibrated, the ratio of long pass pixel values (DN_{LP}) to short pass pixel values (DN_{SP}) calculates temperature (Equation 3-5) without needing to know the emissivity of the object. Values of LP/SP vs. temperature are plotted in Figure 3-11, indicating that unique solutions exist up to about 100 °C, at which point the signals saturate in the camera.

$$\frac{DN_{LP}}{DN_{SP}} = \frac{\alpha_{LP}(T)\cdot\int_{\lambda_1}^{\lambda_2} S_{RF}(\lambda)\cdot\tau_{LP}(\lambda)\cdot E_b(\lambda,T)d\lambda}{\alpha_{SP}(T)\cdot\int_{\lambda_1}^{\lambda_2} S_{RF}(\lambda)\cdot\tau_{SP}(\lambda)\cdot E_b(\lambda,T)d\lambda} \tag{3-5}$$

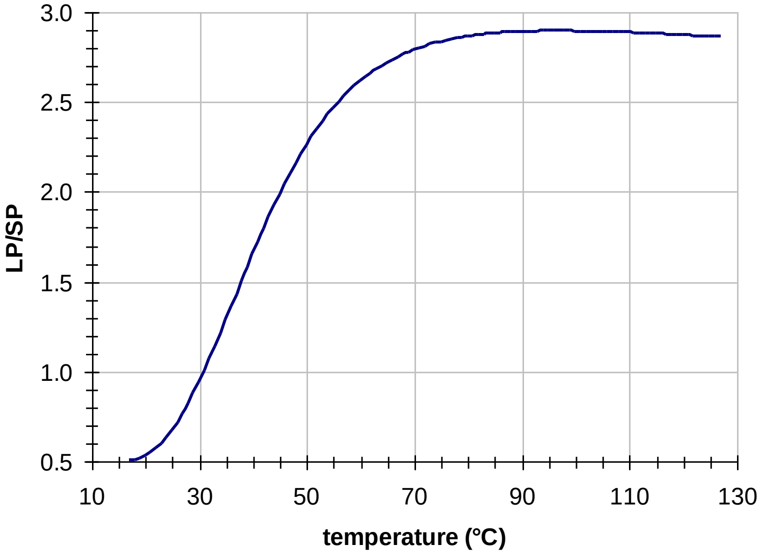

Figure 3-11: LP/SP vs. temperature.

Due to the very low temperatures at which these measurements are taken, it is important that the signal-to-noise ratio be greater than one to ensure valid temperature measurements. For the filter calibration, the signal-to-noise ratio was measured by Equation 3-6 below.

$$SNR = \frac{P\max_p - Pavg_{bkgd}}{\sigma} \quad (3\text{-}6)$$

Where $Pmax_p$ is the maximum pixel value across the particle, $Pavg_{bkgd}$ is the average pixel value of the background, and σ is the standard deviation of the numerator in Equation 3-6 for each temperature.

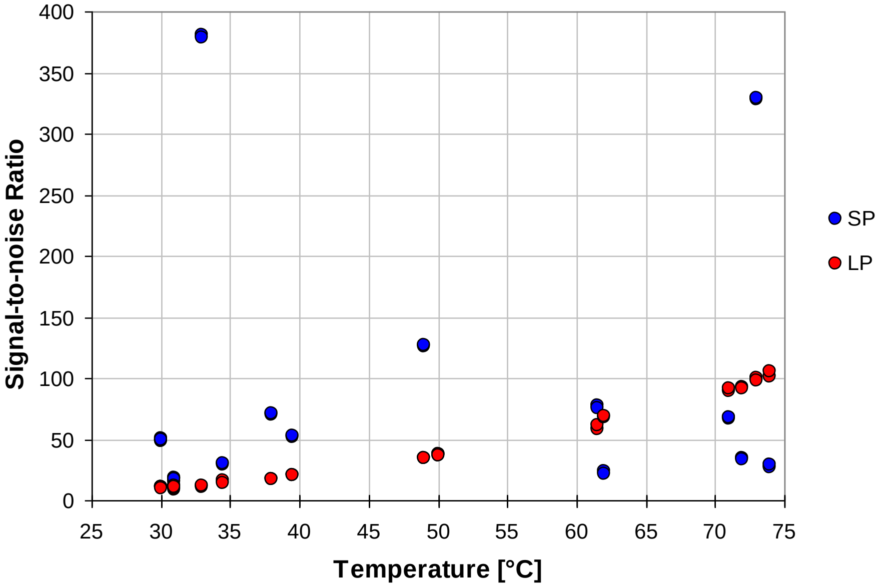

Figure 3-12: Plot of signal-to-noise ratios for the temperature measurement calibration.

Although for the calibration there were only two measurements made for each temperature, the minimum signal-to-noise ratio was 8.7. Figure 3-12 shows the signal-to-noise ratio for each calibration temperature.

This modified 2-color pyrometry method used in conjunction with the IR camera system described provides a means to accurately measure particle temperatures with three distinct advantages over other temperature measurement techniques: 1) it is not necessary to know particle emissivities, 2) enables temperature measurements only slightly above ambient temperature, and 3) can measure temperatures of particles of only several microns in diameter.

3.5.3 Coupling Size and Temperature Measurements

Because the high-speed and IR cameras make size and temperature measurements independently, several steps ensure accurate data collection:

1) The high-speed and IR cameras are centered on the focus of the beam by focusing on the end of the 0.0005 inch wired when placed at the focal point while the beam power is set to 0.01 W. This generates a shadow for the high-speed camera and heats the wire enough to view easily with the IR camera.

2) The laser is set to the desired power and particles are trapped by passing the needle coated with particles through the beam, near the focus. This step is repeated until particles become visible on the IR image. Due to the diffraction limit of the IR camera and lens, particles easily visible with the high-speed camera do not always register on the IR camera image. When visible, particles appear as bright spots (Figure 3-13); however, very large spots on the IR camera usually indicate groups of particles. Avoiding these groups and targeting the smaller spots helps to ensure single particle measurements.

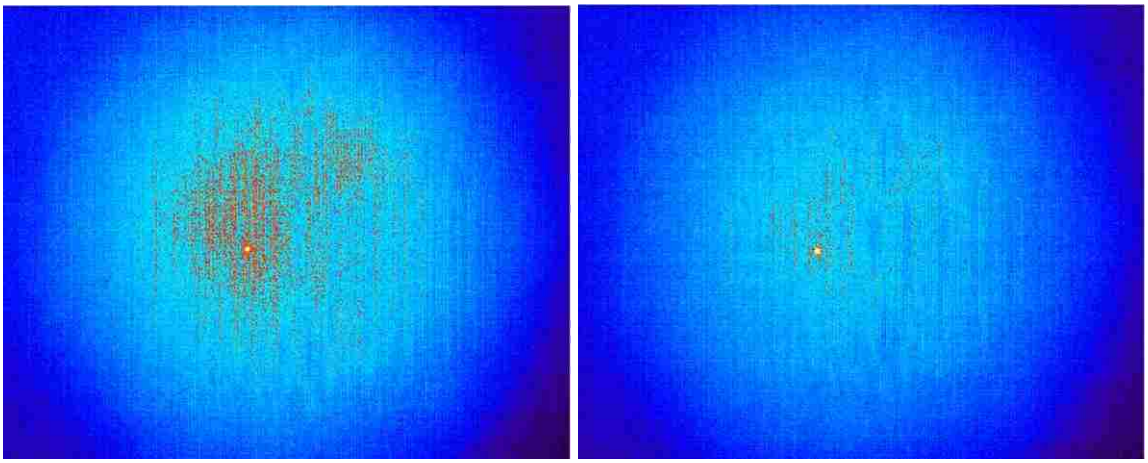

Figure 3-13: Examples of trapped particles imaged with the IR camera.

3) Because the IR camera has a field of view that is much larger than the high-speed camera, 3.65 mm x 2.92 mm versus 190 μm, the IR image discerns relative particle position and approximates the distance of the target particle from the focal point. Once the target particle is determined, its distance from the focus is measured and the high-speed camera position is changed accordingly via a three-dimensional position controller. The vertical adjustment knob moves the field-of-view approximately 1 μm/degree in order to place the particle within the high-speed camera's field of view.

4) If it happens to be a group of particles, the previous steps are repeated until a single particle is successfully isolated. Often, particle movement, especially when significant, helps determine that the same particle is captured by both cameras. Once the particle is located and determined to be a single particle and not a group of particles, the high-speed camera focuses on the particle's shadow and saves at least 3 images to average for d_p measurements.

5) The IR camera focuses on the particle with both the long pass (LP) and the short pass (SP) filters and at least 3 images are saved for each filter. Pixel values extracted from these images determine particle temperature.

4 Results

Theoretical and experimental results appear below, in that order. The concluding section of the experimental results includes comparisons of the theory with the theory. The model development provides a basis to evaluate (and design) the experiments. The final section of this chapter provides critical comments on sources of error based on these experiments.

4.1 Particle Levitation Model Results

As noted above in the Experimental Methods section, essentially any visible or near-infrared laser beam oriented in any direction stably traps solid particles. Vertical beams propagating upward are the most effective for reasons that will be discussed later. Additionally, while a particle remains in the beam, the beam can be moved slowly and the particle follows the path of motion as long as the beam is not obstructed in any way or moved too quickly. These observations led to the hypothesis that there was a natural convective flow induced around the particles as they warmed to somewhat above ambient temperature in the beam focus. This flow creates a drag force that is the dominant force in the trapping mechanism for absorbing particles. The following sections describe the development of the Particle Levitation Model (PLM). This model describes the process, which differs in major ways from all explanations reviewed in the literature.

4.1.1 Energy Balance

An energy balance provides estimates of particle surface temperature, including convective and radiative heat transfer and energy generation through chemical reaction or physical transformations. The data generally use inert or at least nonreacting particles to maintain focus on the levitation rather than the reaction mechanisms. The energy balance equates the change in enthalpy, heat from chemical reaction, and heat from the laser light to the heat lost through convection and radiation (Equation 4-1).

$$m \cdot C_p \frac{dT}{dt} + \Delta H_r \cdot q_{rxn} + P_L \iint_{A_{p,cs}} S_L dA = A_{p,s} h(T_p - T_\infty) + A_{p,s} \varepsilon \sigma (T_p^4 - T_\infty^4) \qquad (4\text{-}1)$$

Where m is particle mass, C_p is the heat capacity of the particle, ΔH_r is the heat of combustion for the specific particle type, q_{rxn} is the reaction rate, P_L is the total laser power, $A_{p,cs}$ is the effective optical cross-sectional area of the particle (which in some conditions can exceed its geometric cross-sectional area), S_L is a function of spatial parameters that describes the beam shape (typically Gaussian cross section), h is the convective heat transfer coefficient, T_p is the particle surface temperature (assumed constant in this case), T_∞ is the ambient gas temperature, $A_{p,s}$ is the particle geometric surface area, ε is the particle emissivity, and σ is the Stefan-Boltzman constant. If the particle is small relative to the beam diameter, the effective cross sectional area of the particle will be its absorption cross section as calculated by Mie scattering and the integral can be approximated as the ratio of the particle absorption cross section to that of the beam. These absorption cross sections differ from physical cross sectional areas, depending on the size of the particle relative to the beam wavelength and the optical properties of the particle. However, the integral on the left is in all cases a constant for a fixed beam shape and particle size. For larger particles, corrections for non-planar waves in a Mie calculation must be included. Also, because this investigation focuses on isothermal, nonreacting particles, the first two terms are zero.

4.1.2 Force Balance

To account for optical trapping, each force acting on the particle must be quantified. As described briefly in the background section, an overall force balance on the particle might include five forces that influence the trapping mechanism: gravity, photophoresis, thermophoresis, the force due to the momentum transfer of the laser light (photon force), and free convective drag. This section describes the origin of each force and its influence, if any, on the trapping mechanism.

Photophoresis is caused by non-uniform heating of the particle surface. In the case of optical trapping, absorption of laser light heats the particle. This causes the ambient gas molecules to rebound with greater momentum from the hotter regions of the surface, generating a net force in the direction of the cold side of the particle, which is usually parallel to the beam direction [7, 28, 34]. For this to be significant to the optical trapping mechanism, which has been previously proposed [27, 28], there must be a sufficient temperature gradient within the particle to cause a net force. Experimental observations of particle motion while trapped indicate that particles may spin while trapped, which would diminish any gradient in temperature that would otherwise have existed. However, small particles respond very rapidly to changing thermal environments, and even rapid small-particle rotations in other applications do not always eliminate temperature gradients. Also, calculations of the Biot number (Equation 4-2) show that any temperature gradient in the particle is negligible. For example, a 5 μm black liquor particle would have a surface temperature of approximately 49 °C (calculated by the energy balance presented above) and a Biot number of about 0.05. If $Bi \ll 1$, temperature gradients are negligible [58].

$$Bi = \frac{h \cdot d_p}{6 \cdot k_p} \tag{4-2}$$

where h is the heat transfer coefficient, d_p is the particle diameter, and k_p is the thermal conductivity of the particle. The preceding arguments suggest photophoresis should be negligible for small particles and it is not included in the model. Zhao *et al* [9] developed an expression for the photophoretic force, Equation 2-1, as discussed in the Literature Review. This expression was developed for 65-150 μm particles and thus is not applicable to this investigation. Zhao's expression significantly over predicts the photophoretic force for the particle sizes of interest to this work (< 10 μm). Other work has been done to quantify photophoresis on aerosols and other transparent particles [59-62]; unfortunately, this work does not translate to opaque particles.

As discussed in the Background section, thermophoresis affects particles smaller than about 100 μm when a temperature gradient exists in the bulk gas creating a force in the direction of the lower temperature. The molecules in the higher temperature region move with greater kinetic energy and the particles naturally diffuse towards the lower temperature region. Equations 4-3 and 4-4 provide quantitative expressions for the thermophoretic force [63]:

$$F_{th} = \frac{-9\pi \cdot \mu^2 \cdot d_p \cdot H \cdot \nabla T}{2\rho_g \cdot T} \tag{4-3}$$

$$H \cong \left(\frac{1}{1+3Kn}\right)\left(\frac{{k_a}/{k_p} + 2.2Kn}{1+2\,{k_a}/{k_p} + 4.4Kn}\right) \tag{4-4}$$

where μ_g is the gas viscosity, d_p is the particle diameter, T is the surrounding gas temperature, ρ_g is the gas density, k_g and k_p are the thermal conductivities of the gas and the particle, and the Knudsen number, Kn, is the ratio of the particle diameter to the mean free path. As indicated by Equation 4-3, for thermophoresis to play a major role in the trapping mechanism there would have to be a significant temperature gradient in the bulk gas. However, in this work, the temperature gradient exists only between the particle and the surrounding air, not within the bulk gas. In addition, the gradients between the particle and the air are in essentially all directions and would provide no preferential path for particle motion. Consequently, thermophoresis is not considered significant to the particle trapping mechanism.

The Background section also included a discussion of thermal transpiration, which is only operative under vacuum pressures or on nano-scale particles at ambient conditions. Therefore, this force is not included in this model.

When light focuses upon a small particle, the cumulative momentum of the photons creates a force large enough to influence particle motion. Each photon carries momentum equal to h/λ, where h is Planck's constant and λ is the wavelength of the incident light [42]. Equation 4-5 gives the expression for the photon force, or radiation pressure force [64].

$$F_{rad} = \frac{I_{inc}}{c}(C_{ext} \cdot a - C_{sca} \cdot g) \qquad (4\text{-}5)$$

Where I_{inc} is the incident intensity on the particle, c is the speed of light, C_{ext} and C_{sca} are the extinction and scattering cross-sections, respectively, a is the direction of laser propagation, and g is the asymmetry vector. The asymmetry vector gives the direction of the scattered light.

The final force considered in the trapping mechanism is the free-convective drag force. Because the laser heats the particles, a free convective flow develops and creates a drag force that acts upward regardless of beam orientation. As will be shown in the next section, this free-convection-induced drag force is the largest weight-counteracting (upward) force on the particle in most cases and the most important force in the optical trapping mechanism. Quantifying this force is difficult because the scale of the particles complicates the determination of the convective flow velocity. The computational fluid dynamics program Fluent can provide estimates of this free convective flow and the resultant drag forces on the particles. The following section details the results of the drag force model.

4.1.3 Drag Force Model Results

Fluent-based numerical simulations provide quantitative data that support the hypothesis that levitation is dominated by the induced convection currents. Induced convective drag force calculations for 5–200 μm diameter spheres at temperatures from 300–1700 K indicate that increasing particle temperature and diameter result in increased convection-induced drag forces. The drag forces were computed for isothermal spheres in air at 1 atm.

The induced-drag forces scale approximately linearly with diameter and particle surface temperature. Since particle weight increases with the cube of particle diameter, increasingly intense beams are required to levitate larger particles. The upper bound of particle temperature, which is usually a materials constraint, limits the intensity of the beam that can be absorbed by a particle and hence the size of the particle that can be levitated. The estimated convective forces on particles of various sizes and temperatures will be discussed. In estimating these forces, normalized velocity and energy residuals were less than $1x10^{-4}$ and $1x10^{-7}$, respectively, and approximately 18,000 nodes covered a 100x100 mm axisymmetric grid, resulting in grid-independent and tightly converged solutions.

The following figures (Figure 4-1 a-d) illustrate gas-phase density contours for various particle sizes. These contours show that the upward convective flow increases with increasing diameter. This convective flow induces a drag force upon the particles that stabilizes them in the optical trap. Velocity contour plots illustrate this free convective flow around the particles (Figure 4-2 a-d). (Contour plots were generated with Fluent.)

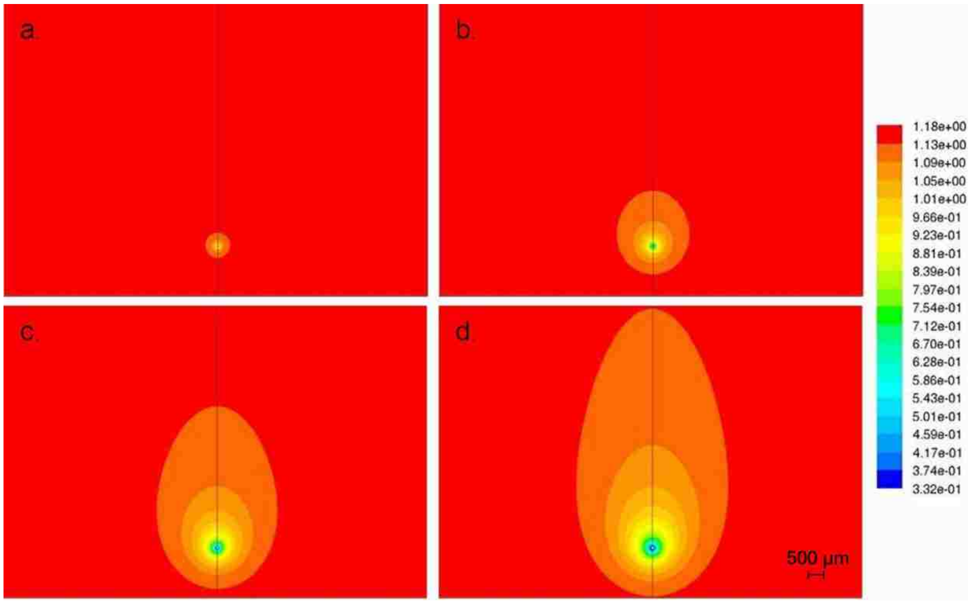

Figure 4-1: Density contours for particles of *a)* 25 µm at 600 K, *b)* 50 µm at 800 K, *c)* 75 µm at 1000 K, and *d)* 100 µm at 1100 K; surface temperatures were estimated by the energy balance. The scale shown is in kg/m^3.

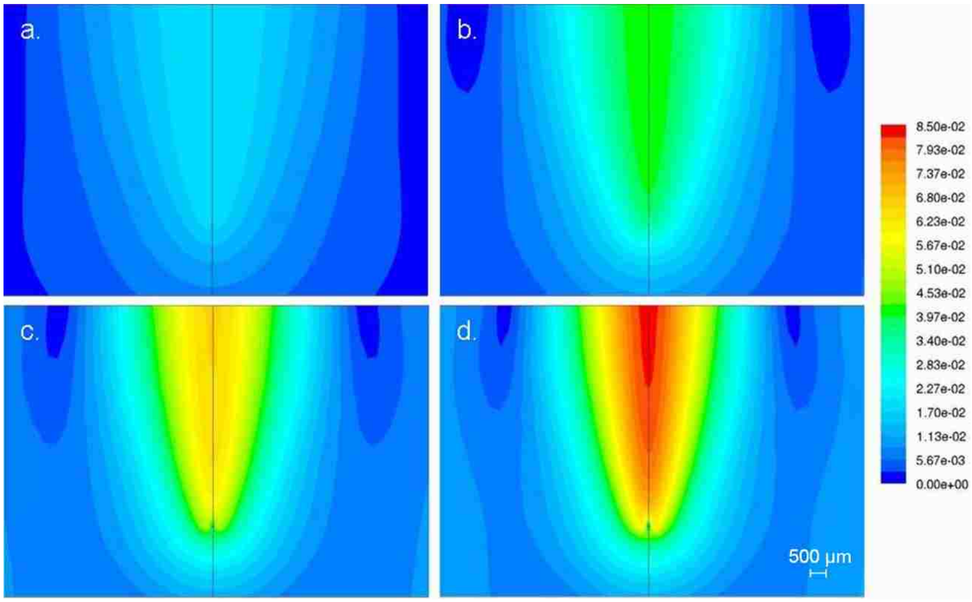

Figure 4-2: Velocity contours for particles of *a)* 25 µm at 600 K, *b)* 50 µm at 800 K, *c)* 75 µm at 1000 K, and *d)* 100 µm at 1100 K; surface temperatures were estimated by the energy balance. The scale shown is in m/s.

The drag force model results agree with experimental data taken by Mograbi and Bar-Ziv [10] within 20%, illustrated in Figure 4-3, over a relatively broad range of temperatures and forces. An electrodynamic balance provided these data based on drag forces for glassy carbon particles heated with a CO_2 laser. There are systematic differences between our predictions and the data. The origin of these differences is not clear, with errors in our analysis or the experimentally estimated temperatures [7] being candidates. Nevertheless, it is apparent that the trends are qualitatively reproduced by this analysis.

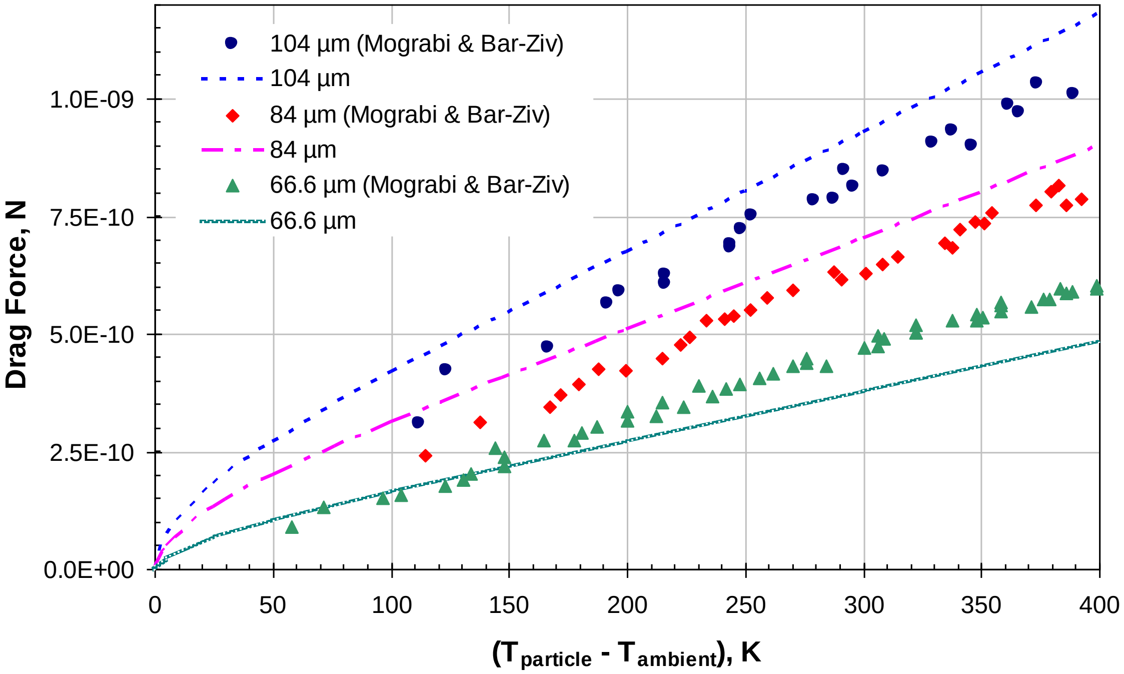

Figure 4-3: Comparison of Fluent predictions with experimental results (Mograbi & Bar-Ziv [10]) of the free-convective drag force versus *ΔT).*

4.1.4 Radiation Pressure: Prediction with Scattering Code

A Mie-type scattering code predicts the net scattering force upon trapped particles. The Amsterdam Discrete Dipole Approximation (ADDA) is a C-based software package that predicts scattering and absorption of light by spherical particles [65, 66]. (The capabilities and limitations of this software are discussed in detail in the referenced article by Yurkin *et al* [66].) The discrete dipole approximation is a method for computing scattering and absorption of electromagnetic radiation by particles of arbitrary geometry [67]. ADDA allows specification of beam parameters (shape, propagation direction, width, and wavelength), particle properties (diameter and complex refractive index), and particle position with respect to the beam center. This allows computation of the radiation pressure force as a function of particle position for a given set of beam and particle parameters. Radiation pressure is the sum of the forces due to both absorption and scattering of light by a particle, expressed by Equation 4-5 [64]. This expression is accurate for a plane wave; however, it can be applied to a Gaussian beam if the localized approximation applies [68-71]. The localized approximation is applicable for a Gaussian beam if the particle is large compared to the wavelength and the beam waist is large compared to the particle [72]. All simulations were modified accordingly. For example, simulations for a 5.5 µm particle would have the following parameters: λ = 532 nm, d_p = 5.5 µm, and $d_b = 2\omega_o$ = 60 µm, where d_b is the beam diameter. These values are consistent with experimental observations. The results of these simulations are shown in Figure 4-4.

This plot shows that the axial component of radiation pressure is a maximum at the beam center and follows a Gaussian profile as does the beam. This result was expected; however, the results for the radial component are more significant. The radial component is negative, indicating that this force is towards the beam center; it also shows a maximum force near r_c/ω_o = 0.375, after which the force decreases. This indicates that the particle will feel a force pulling it toward the center of the beam, thus radially stabilizing the trapped particle. The axial and radial forces are small in most cases compared to, for example, the induced drag force. However, this is the only force that consistently stabilized the particle radially and therefore this represents a significant consideration in the model.

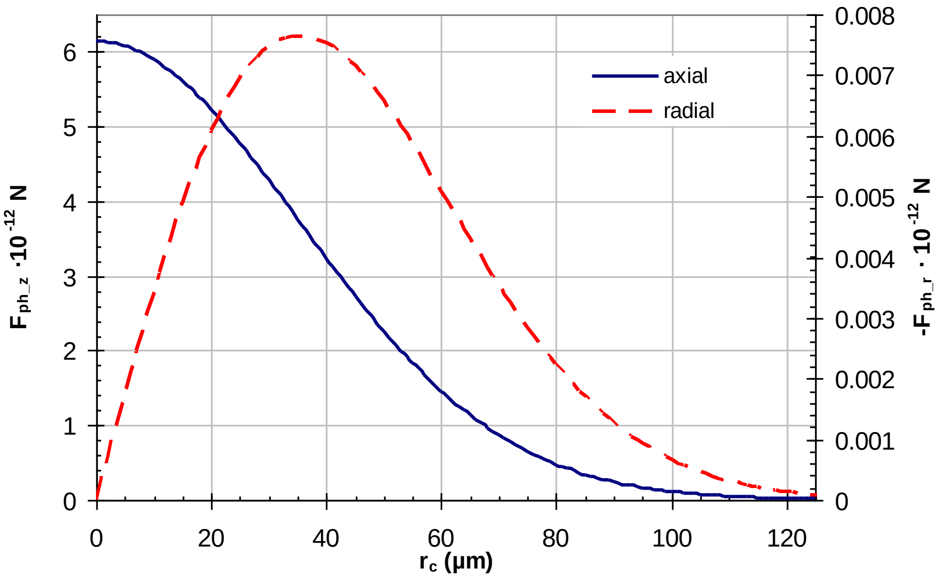

Figure 4-4: Plot of x- and z-components of the radiation pressure force as predicted by the ADDA scattering code (P = 1W, d_p = 5.5 μm, ω_o = 60 μm).

The origin of the radial component lies in the fact that these particles are much larger than the wavelength of incident light ($d_p/\lambda >> 1$). For d_p much greater than λ, there is much more light scattered in the forward direction than in the back direction. Figure

4-5, generated by a scattering program called MiePlot [73], plots scattering intensity versus angle for particles illuminated by 532 nm light.

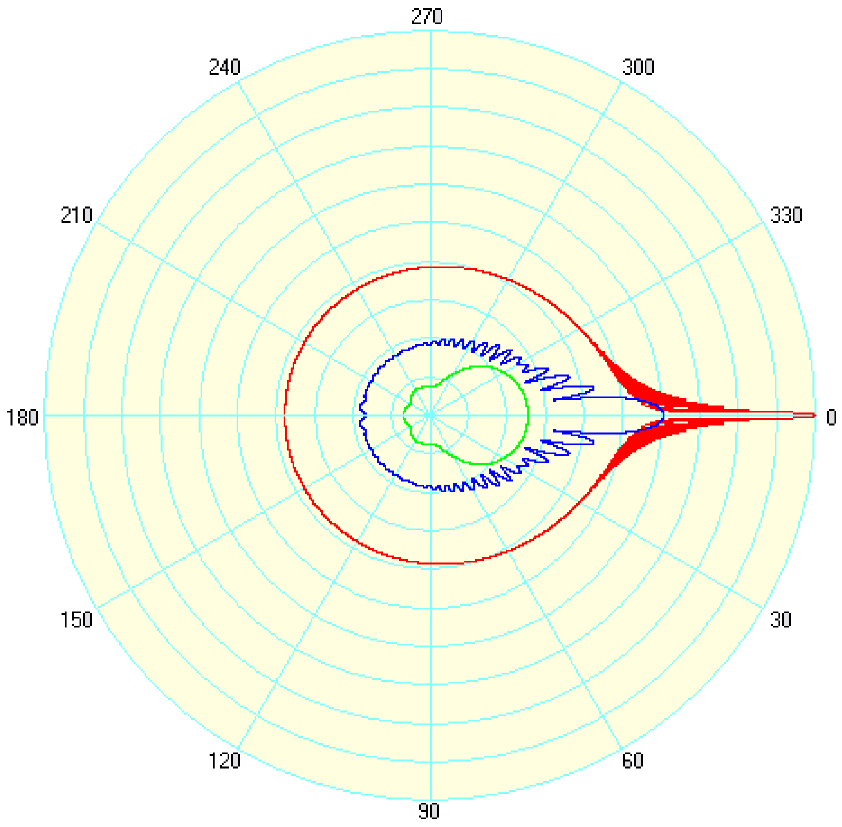

Figure 4-5: Scattering intensity vs. angle for 0.5 µm (green), 5 µm (blue), and 50 µm (red), particles in 532 nm incident light (refractive index: real = 1.6, imaginary = 0.05) [73].

The radial dimension in this plot is logarithmic and divided in powers of 10. Note how much more pronounced the forward scattering becomes as particle size increases. The converse would be evident when using smaller particles or beams of longer wavelengths, causing d_p/λ to become smaller (Figure 4-6). As this ratio approaches 1, the forward and backward scattering lobes become symmetric and the radial restoring force goes to zero. This scattering characteristic may explain the inability to trap particles with IR laser beams.

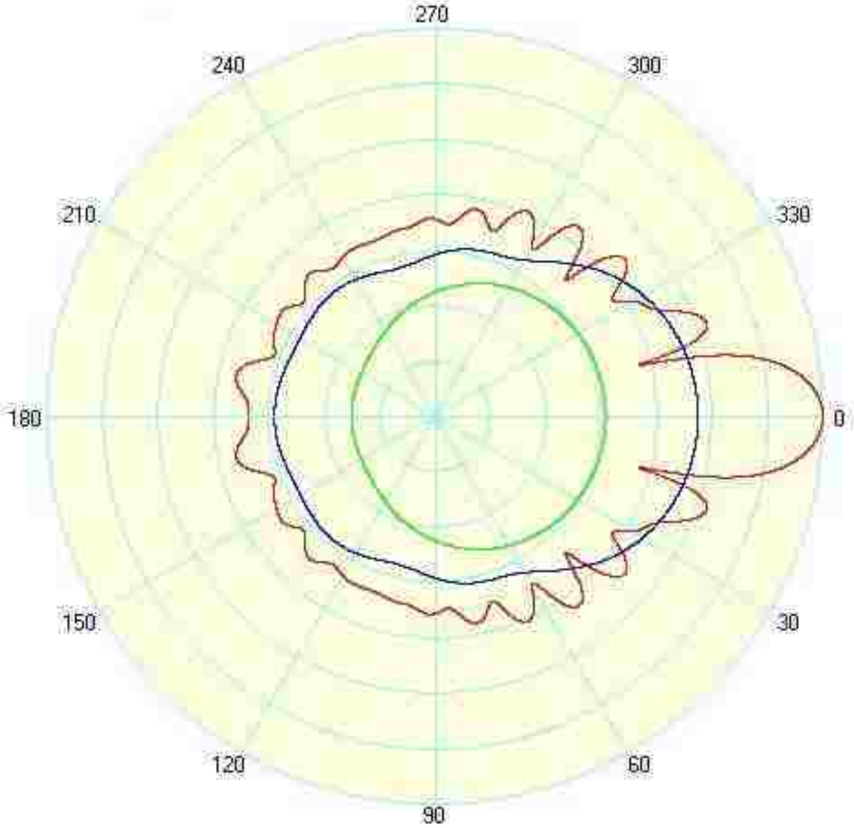

Figure 4-6: Scattering intensity vs. angle for 5 μm (green), 10.6 μm (blue), and 50 μm (red), particles in 10.6 μm incident light (refractive index: real = 1.6, imaginary = 0.05) [73].

However, when particles that are large with respect to the beam's wavelength remain centered in the beam, the forward scattering stays on-axis and the particle experiences no radial photon force. However, when these particles move off-axis, the forward scattered lobe also moves off-axis (Figure 4-7), though perhaps not as symmetrically as this figure illustrates. This imparts a force that is in the direction of the beam center, which acts as a restoring force to maintain particles within the beam that may have otherwise become unstable due to small perturbations. If the perturbations are large enough to move the particle sufficiently out of the beam that the radial force is small, the particles fall out of the beam.

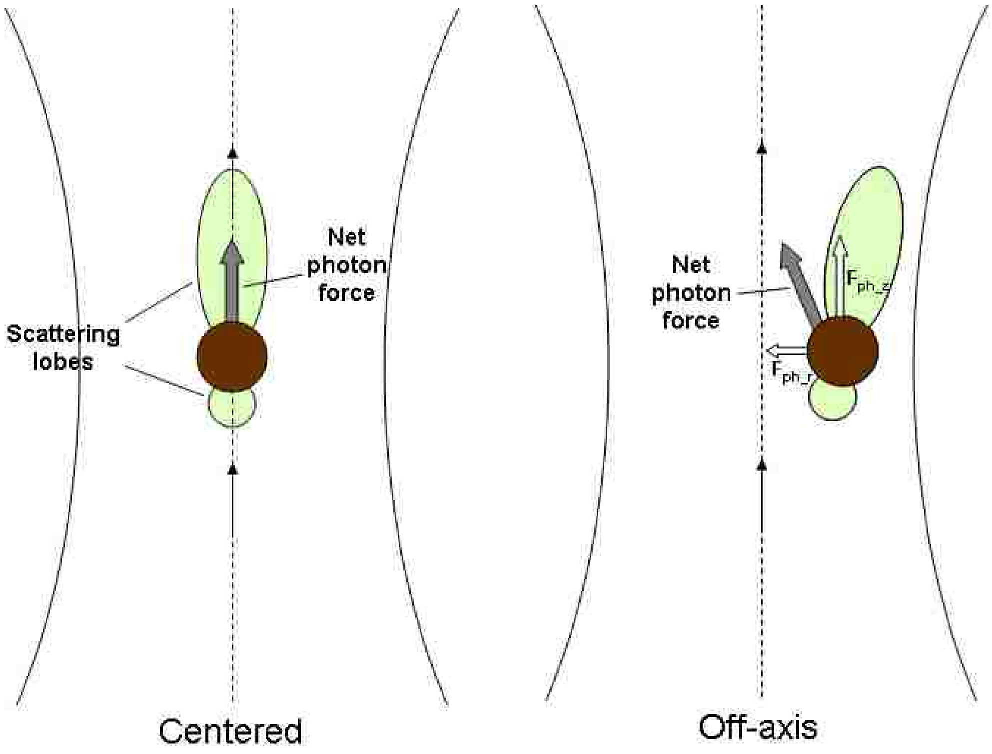

Figure 4-7: Diagram of off-axis scattering lobes and corresponding photon force as a particle moves off beam center.

4.1.5 Drag and Photon Force Equations

The drag force results computed by Fluent were fit to two expressions that agree with Fluent results within about 10% (Equations 4-6 and 4-7), except at very low temperatures (about 300 K or lower). Table 4-1 lists the coefficients. The low-temperature fit ($F_{drag.low}$) is used for $T_p < 350$ K and $d_p \leq 5$ µm; the high temperature fit ($F_{drag.high}$) is used for $T_p > 325$ K and $d_p > 5$ µm. In the equations, d_p is particle diameter in µm and $\Delta T = T_{particle} - T_{ambient}$ in Kelvin.

$$F_{drag.low} = \left(A(d_p)\cdot\Delta T + B(d_p)\right)\cdot 10^{-12} N \quad (4\text{-}6)$$

$$F_{drag.high} = \left(C(d_p)\cdot\Delta T + D(d_p)\right)\cdot 10^{-12} N \quad (4\text{-}7)$$

$$A(d_p) = a_2 d_p + a_3 \quad (4\text{-}8)$$

$$B(d_p) = b_1 d_p{}^2 + b_2 d_p + b_3 \quad (4\text{-}9)$$

$$C(d_p) = c_1 d_p{}^2 + c_2 d_p + c_3 \quad (4\text{-}10)$$

$$D(d_p) = d_1 d_p{}^2 + d_2 d_p + d_3 \quad (4\text{-}11)$$

Table 4-1: Coefficients for Equations 4-8 through 4-11.

	1 / (µm^{-2})	**2 / (µm^{-1})**	**3**
a		**$7.639\cdot10^{-3}$**	**$-1.085\cdot10^{-2}$**
b	**$1.92\cdot10^{-2}$**	**$-9.813\cdot10^{-2}$**	**0.1198**
c	**$2.94\cdot10^{-4}$**	**$8.379\cdot10^{-3}$**	**$-2.613\cdot10^{-2}$**
d	**$1.281\cdot10^{-2}$**	**$-8.562\cdot10^{-2}$**	**0.3584**

The photon force model results from ADDA have also been fit to equations that describe the axial photon force (Equation 4-12) and the radial photon force (Equation 4-13); the coefficients for the photon forces are listed in Table 4-2. (The terms axial and radial refer to the beam axis.) These equations fit the axial and radial simulation results within 5% and 2%, respectively.

$$F_{ph\_z} = \frac{I_{inc}\cdot(A\cdot d_p^{\,2} + B\cdot d_p + C)}{c}\exp\left[\frac{-\left(r_c/\omega_o\right)^2}{2\cdot D^2}\right]\cdot 10^{-12} \tag{4-12}$$

$$F_{ph\_r} = \frac{I_{inc}\cdot(V\cdot d_p^{\,2} + W\cdot d_p + X)\cdot \omega_o^{\,Y}\cdot\left(r_c/\omega_o\right)}{c\cdot Z}\exp\left[-\frac{\left(r_c/\omega_o\right)^2}{2\cdot Z^2}\right]\cdot 10^{-12} \tag{4-13}$$

Table 4-2: Coefficients for Equations 4-12 and 4-13.

A	0.7461 m^2	***V***	355.3 m^2
B	0.9724 m^2	***W***	-2291 m^2
C	-2.541 m^2	***X***	5044 m^2
D	0.5006	***Y***	-0.9941
		Z	0.5013

I_{inc} is the incident laser intensity, c is the speed of light in a vacuum, r_c is the distance of the center of the particle from the center of the beam, d_p is the particle diameter in µm, and ω_o is the beam waist in µm.

4.1.6 Particle Levitation Model: Iterative Method

The Particle Levitation Model combines the results of the energy and force balances to predict incident photon and drag forces and particle surface temperature for a given particle size, properties, and position. The process is iterative as outlined below (Figure 4-8), where Φ_p represents particle properties (refractive index and density).

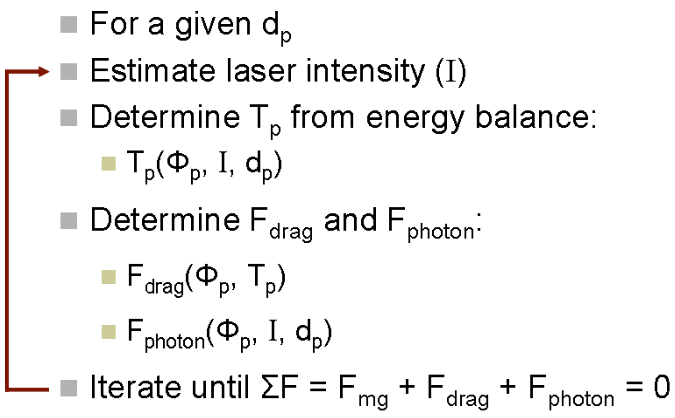

Figure 4-8: Iterative procedure for Particle Levitation Model.

As previously discussed, this model assumes that the only significant forces acting on suspended particles are the photon and free convective drag forces. Particles find a place in the beam where the forces equilibrate: $F_{mg} = F_{photon} + F_{drag}$. Consequently, given a particle with specified size and properties, it will experience the same photon force, drag force, and temperature regardless of beam power. When beam power changes, the forces also change and cause the particle to change position (both radially and axially within the beam) in the beam to allow forces to equilibrate again, otherwise they fall out of the trap. The following sections include results from this model with comparisons to experimental data.

4.1.7 Force Comparison

Comparison of the drag and photon forces relative to particle weight indicates that the free convective drag force is roughly an order of magnitude larger than the photon force. As previously discussed, photophoresis and thermophoresis do not play a significant role in the trapping mechanism.

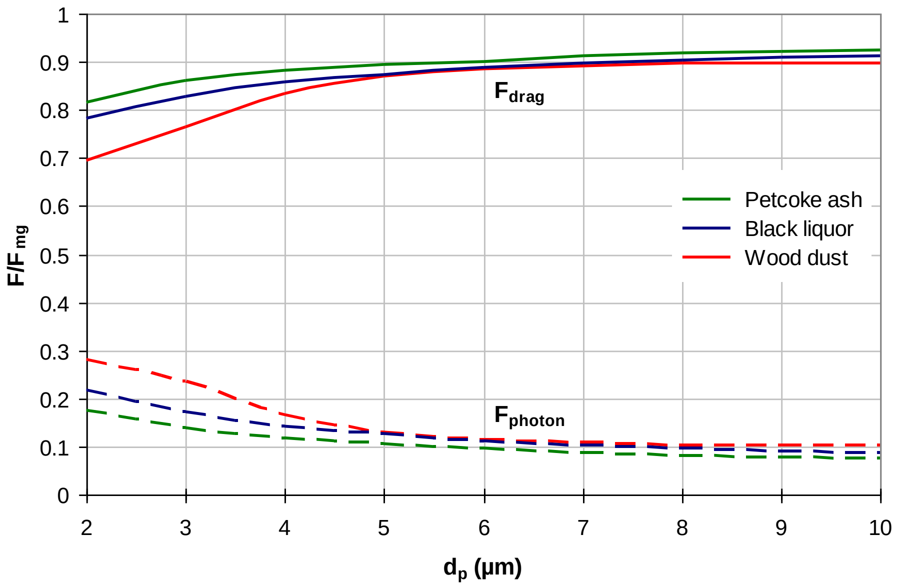

Figure 4-9: Comparison of normalized drag and photon forces for black liquor, wood dust, and petcoke ash.

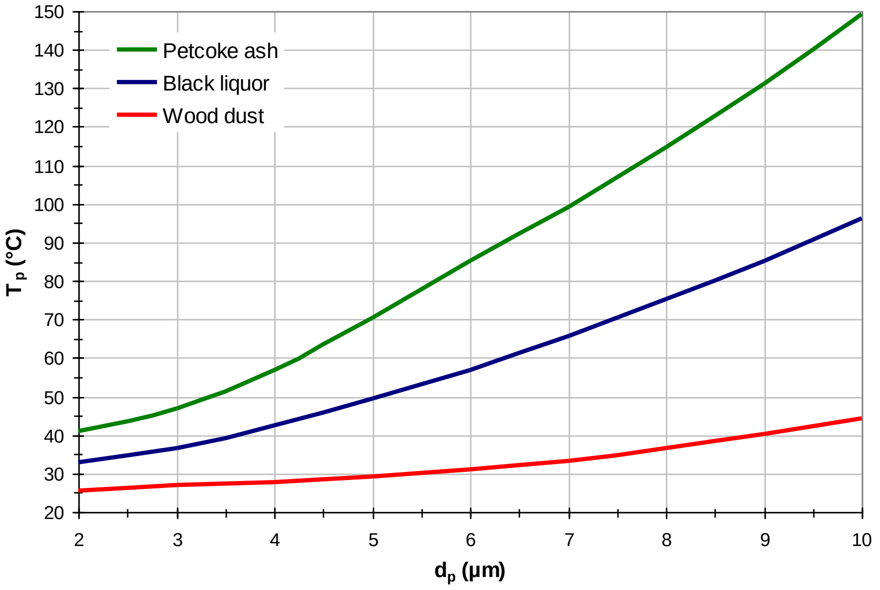

Figure 4-10: Predicted particle surface temperatures for black liquor, wood dust, and petcoke ash.

The convective drag force is far more significant than previously estimated for particles studied in an electrodynamic balance [46]. For 2-10 µm particles evaluated in this work, the free convective drag force ranges from 70-92% of particle weight, as shown in Figure 4-9. The predicted temperatures for particles within this range are shown in Figure 4-10.

4.2 Experimental Results

4.2.1 Particle Size Data

These experiments primarily use three particle types: black liquor, wood dust, and petcoke ash. Table 4-3 lists specific gravities and emissivities of each of the particle types. An optical pyrometer (Pyrometer Instrument Company, Pyrofiber AEMS, model PFD1550/905) measured emissivities. Because exact values are not available for these specific particles, estimates of densities were determined from the literature. Incropera and DeWitt provide the densities of wood dust and petcoke ash [58]. The density of black liquor represents an estimate extrapolated from a range of values provided [74, 75]. The linear fit to the reported data is shown in Figure 4-11. The black liquor used in this work has approximately 95-100% dry solids. Inputting this into the equation for the linear fit gives the estimated specific gravity. Several other particle types were used (Experimental Methods) to observe the capabilities of this technique; however, data collection was limited to black liquor, wood dust, and petcoke ash for practical reasons, although these particles do provide a range of physical properties that allow thorough evaluation of the technique’s capabilities.

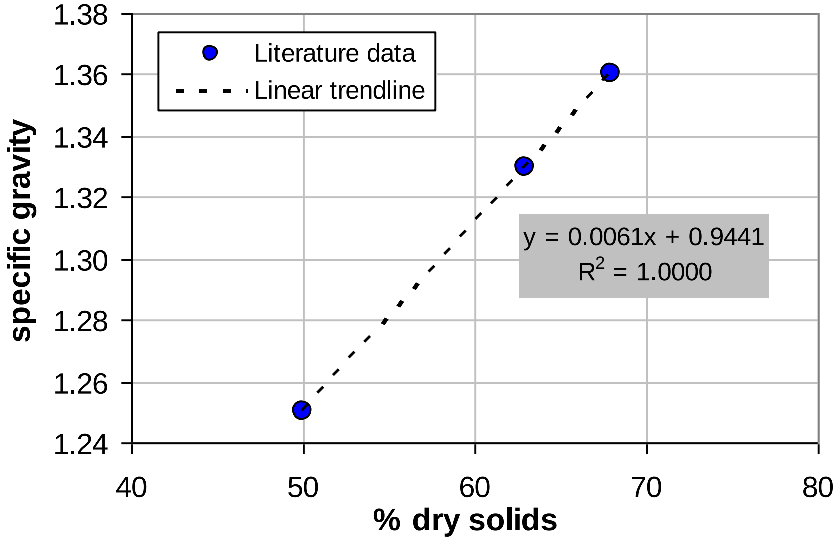

Figure 4-11: Reported black liquor densities from literature and corresponding linear fit.

The high-speed camera measured particle sizes as discussed in the Data Collection Procedures section. Validation of these measurements requires a known size distribution for the particles of interest.

Table 4-3: Properties of particles used in this work [58, 74, 75].

	S.G.	*ε*
Wood dust	0.55	0.457
Black liquor	1.55	0.668
Petcoke ash	2.5	0.883

A Coulter counter (Coulter Electronics, Inc., Model LS100) measured the size distribution of petcoke ash; however, black liquor is water soluble and wood dust absorbs water, thus the Coulter Counter is not a suitable means to obtain size distributions of these particles. Figure 4-12 shows a comparison of sizes measured by the Coulter Counter and the optical trapping technique for petcoke ash particles. Although all measured particle sizes lie within the known size distribution, it is important to make two important notes regarding this plot. First, the nature of the optical trapping mechanism itself provides both upper and lower limits on the size of particles that may be trapped. Larger particles will either burn up when introduced and/or never become stably suspended; smaller particles will not stabilize because the forces cannot balance.

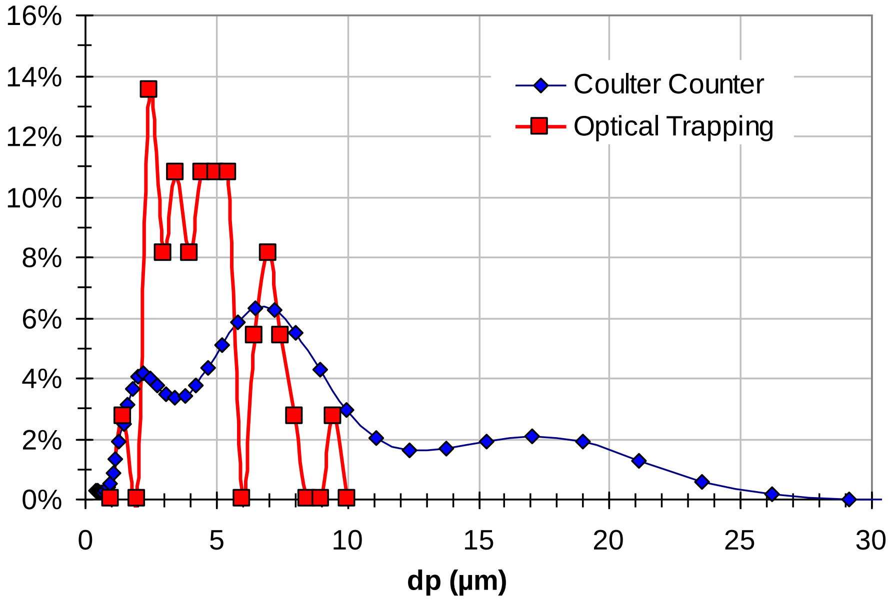

Figure 4-12: Particle size distributions for petcoke ash.

Very few particles beyond the 1-10 μm range are trapped by this technique due to the trapping mechanism. Of course, extremes in particle properties could reasonably produce suspended particles outside of this size range. Second, the size distribution measured by the Coulter Counter indicates a relatively broad range that easily spans the

1-10 µm range. A more accurate approach to validating this size measurement technique would be to obtain particles with a narrow distribution and suitable properties. This approach was not pursued due to limits on time and resources; however, even without these constraints, appropriate particles would be difficult to obtain.

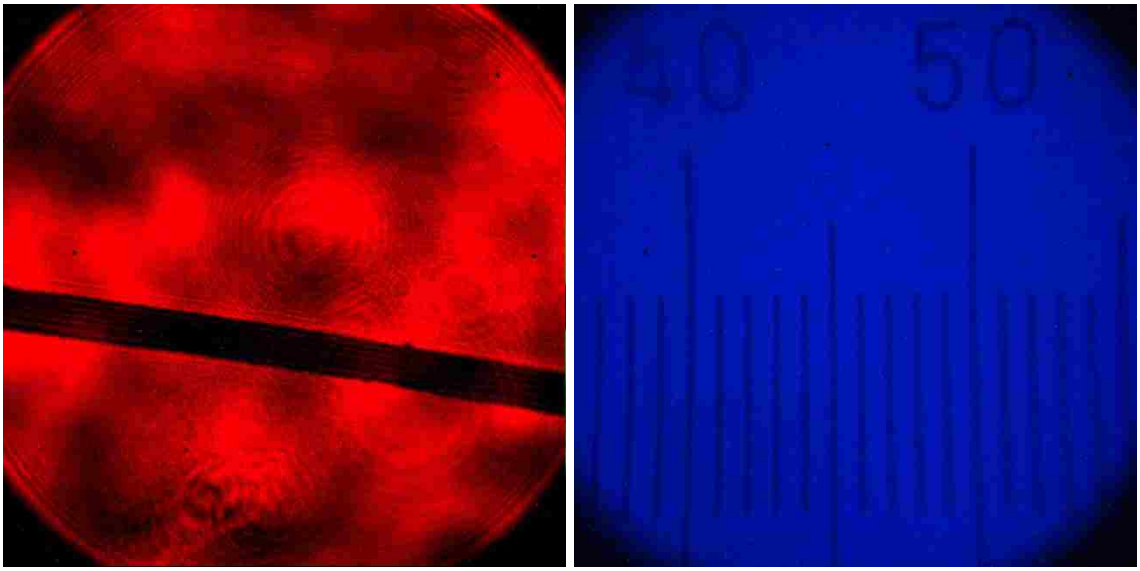

Figure 4-13: Images of 12.7 µm gold wire (left) and microscope reticle (right) used for validation and calibration of particle size measurements.

Validation of black liquor and wood dust size measurements was done with a 0.0005 inch (12.7 µm) gold wire and scanning electron microscope (SEM) images. The wire provided a reasonable comparison of particle images to an object of known size imaged by the same sizing method. Images of this wire and a microscope reticle (10 µm divisions) provided calibration and validation of the size measurement technique for all particles (Figure 4-13).

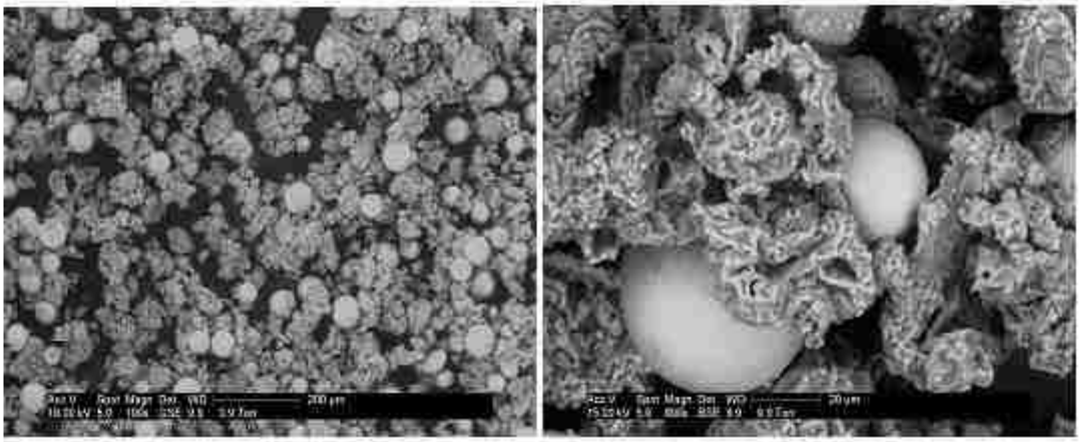

Figure 4-14: SEM images of pulverized black liquor particles.

SEM images for black liquor and wood dust appear in Figure 4-14 and Figure 4-15, respectively. These images indicate a broad particle size distribution for both black liquor and wood dust.

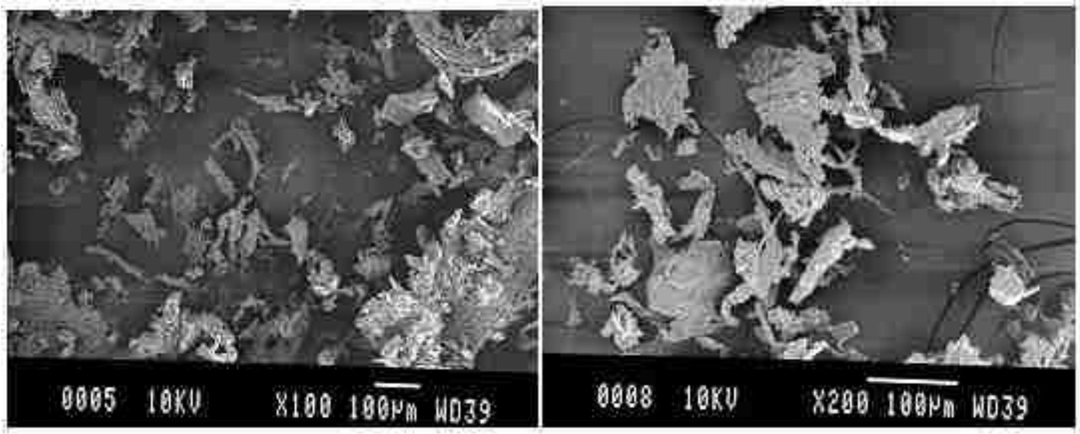

Figure 4-15: SEM images of wood dust particles.

The spheres in the black liquor SEM images are silica beads used to help atomize the black liquor particles in other experiments. These beads are not trapped during experiments because they are much larger than measured particles; the smallest of these beads appears to be about 20 µm. These images indicate that the dried black liquor and wood dust particles break up into much smaller particles when trapped due to their porosity and the rapid heating they experience when introduced into the beam.

4.2.2 T_p vs. d_p: Experiment and Prediction

Particle images were analyzed by the MATLAB® program described in Size Measurement to provide measured particle sizes. Equation 3-5 provides measured particle temperatures based on extracted pixel values from each IR image. The Particle Levitation Model predicts particle behavior according to particle size, type, and properties (Table 4-3). Comparisons of the Particle Levitation Model and experimental results provide the theoretical and experimental information, respectively, to assess understanding and control of this system. This section discusses this comparison.

The following plots summarize experimental and model results of particle temperature versus diameter based on a quadratic fit. The data regression used a quadratic fit because the theoretical particle temperature dependencies on diameter closely follow a quadratic trend in this temperature range. The experimental data themselves do not motivate this choice. The results of this fit (statistical best estimate) and the theoretical predictions appear on each plot, the latter coming from the model developed in this project and independent of any of these measurements. Each plot includes the data, the statistical best estimate of the experimental mean as a function of diameter, 95% confidence intervals for this estimate, 95% confidence intervals for the data points, and the residuals. The definition for the residuals used here is the difference between the statistical best estimate and the measured value, which agrees with the statistical definition of the term but differs slightly from the conceptually more interesting difference between the data and the theoretical prediction. In these cases, these differences are too slight to be of concern. The difference in the two confidence intervals is significant in this analysis. The confidence interval for the mean indicates the region within which the statistically estimated particle temperature should fall, with 95% statistical certainty. The confidence interval for the data indicates the region within which the data should fall, again with 95% certainty. The confidence interval for the mean decreases with increasing number of data points, approximately in proportion to its square root. As the number of data increase, increasingly larger fractions of the data points lie outside the confidence interval for the mean. The confidence interval for the mean also decreases with decreasing scatter in the data, approximately proportional to the standard deviation of the data relative to the predicted values. By contrast, the confidence interval for the data is approximately independent of the number of data points but decreases with increasing data precision. Approximately 5% of the measured data should lie outside of a 95% confidence interval for the data. The confidence interval for the mean is the most rigorous and consistent comparison for the predicted trend in the data. Therefore, the predicted trend should lie within the confidence interval for the mean and well within the confidence interval of the data.

The statistical best estimates and the theoretical predictions agree reasonably well. The trend line for the black liquor data, which is the largest data set, quite closely follows model predictions (Figure 4-16).

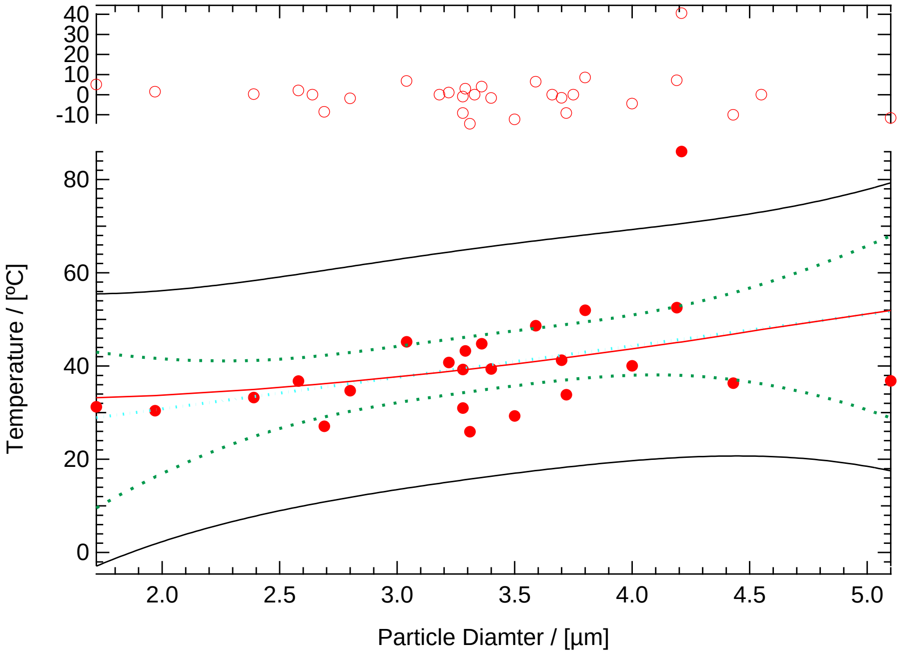

Figure 4-16: Comparison of measured and predicted T_p vs. d_p for black liquor.

Trend lines for the wood dust (Figure 4-17) and petcoke ash (Figure 4-18) data also closely follow the predicted trends but are slightly offset from the predicted statistical best estimates; however, the predictions lie within the predicted 95% confidence region for this estimate. The confidence intervals address the large degree of scatter within each set of data. The confidence intervals show that data for each particle type falls acceptably within the 95% confidence intervals for both the trend lines and the data points, illustrating that the trends of the data follow those of the predictions quite well, considering the different sources of uncertainty.

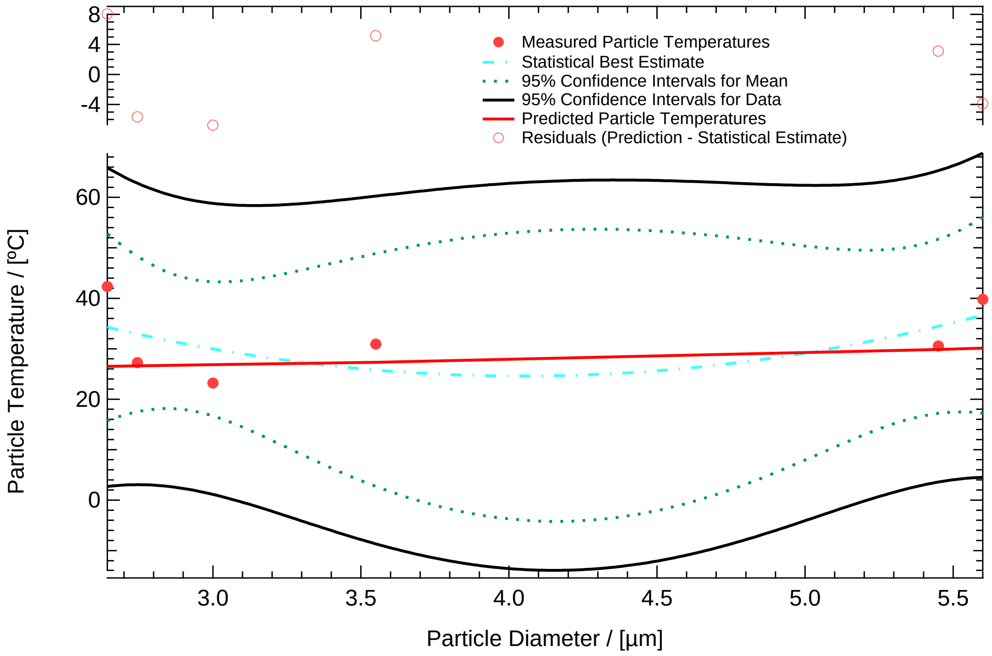

Figure 4-17: Comparison of measured and predicted T_p vs. d_p for wood dust.

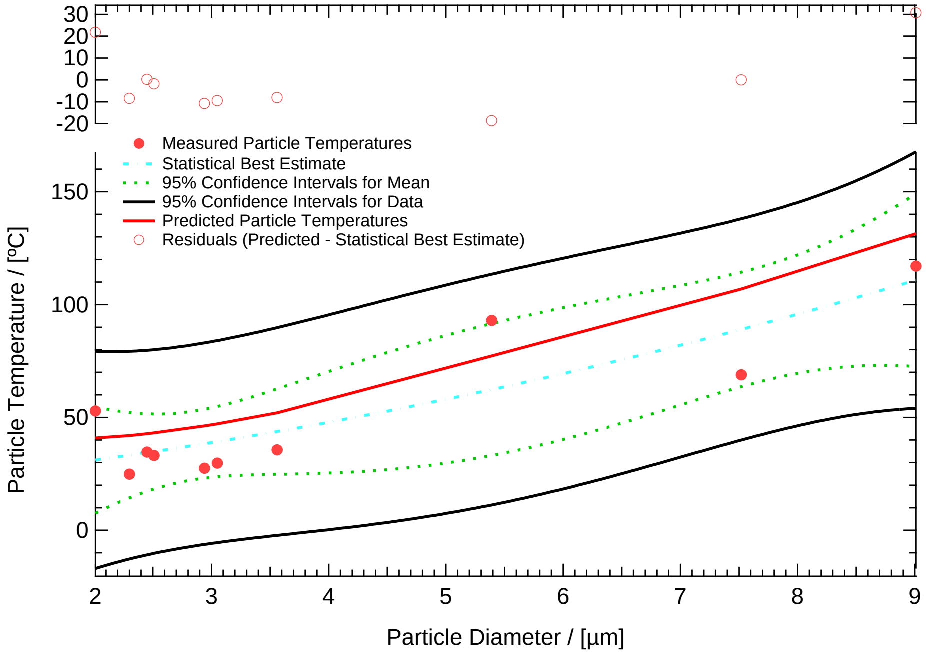

Figure 4-18: Comparison of measured and predicted T_p vs. d_p for petcoke ash.

The large amount of scatter reflects the difficulty in measuring temperatures of particles of this scale. Despite this difficulty, more definitive indications that this theory accurately predicts the particle temperatures depends on decreasing this scatter. The results developed here indicate that the proposed trapping mechanism is qualitatively and possibly quantitatively correct.

Several sources of error create the scatter within these results. Although the uncertainties are difficult to quantify precisely, the following section offers a discussion of the different causes.

4.3 Sources of Error

There are several sources of error in both the particle size and temperature measurements, most of which are due to the scale of the particles and limitations of available diagnostic tools. These sources of uncertainty include issues with both particle stability and diagnostic tools. Discussions of both appear in this section. Discussion of efforts to correct or account for these uncertainties appear throughout the experimental section, but the difficulty of making measurements at such small sizes strains the capabilities of both this analysis and this equipment.

As discussed in the Experimental Methods section, optically suspended particles are exceptionally stable and remain trapped indefinitely under normal conditions. When viewed by the unaided eye, suspended particles are motionless; when viewed through a microscope objective and magnified roughly 2000 times, as with the high-speed camera system, suspended particles actually exhibit significant movement. The drag coefficient for particles of this size obeys Stokes' expression ($C_D = 24/Re$) and, given that Reynolds numbers are near zero, the drag force is very large compared to the particle mass. Therefore, these particles respond almost instantly to very small changes in bulk air flow and, thus, move up to several microns with even very small air currents. Due to this motion, particles regularly move laterally in and out of focus and vertically along the plane of the beam (Figure 4-19).

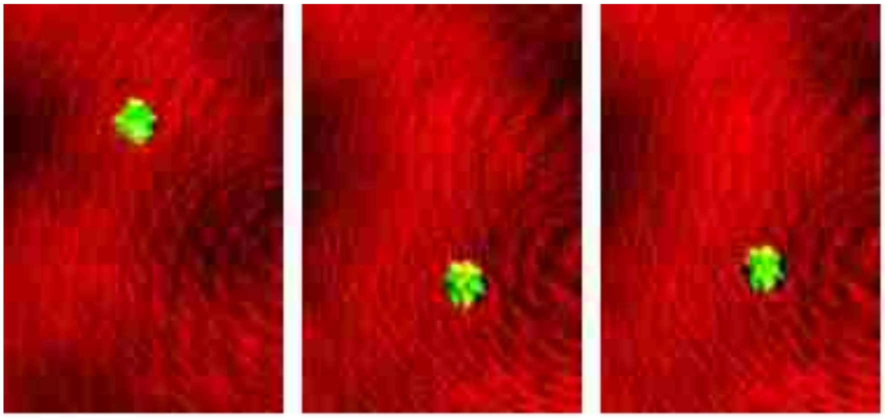

Figure 4-19: Particle images taken with high-speed camera showing movement of particle while obtaining images for size measurement.

Because the depth of field of the imaging system is itself only several microns, this sometimes causes the particle to move slightly out of focus during data collection. This does not necessarily impact the temperature measurements since the relative intensities of light of different wavelengths should be the same even if the image is out of focus, presuming chromatic aberrations are minimal in the optical system. However, the focus issue does affect measured particle sizes. To minimize this error, at least three particle images for each particle formed the raw data used in these analyses (Figure

4-19). The results represent the average of these images. Depending on imaging thresholds, lack of focus generally increases and rarely decreases the measured size. The averaging techniques can reasonably address random errors, but they will not address this systematic error. Because of the high-intensity trapping beam, scattered light from trapped particles is also quite intense. When magnified with the imaging system, this scattered light can distort particle size and cause them to appear larger than they are in reality. Using an expanded He-Ne beam for particle detection and an optical filter to exclude non He-Ne light greatly reduces this problem. The He-Ne beam intensity is far lower than the suspension beam and allows accurate detection of the particle edges. However, for larger particles, this can still be problematic because they scatter more light, which obscures the edge of the particles even with the He-Ne beam (Figure 4-20).

The color imaging system originally designed to take obtain particle temperature measurements exhibited unexpectedly low light sensitivity and highly nonlinear response at light intensity, rendering it incapable of making reliable measurements. The Appendix includes a detailed discussion and analysis of this finding. Although this imaging system does not measure particle temperature, its nonlinear response at light intensity extremes makes it more difficult to obtain accurate particle size data. Reducing the exposure time for large, bright particles reduces pixel saturation and increases sizing accuracy; particles less than 3 μm in diameter have smaller absorption cross-sections, and the camera does not always detect the 532 nm scatter from such particles – though the camera always clearly detects particle shadows.

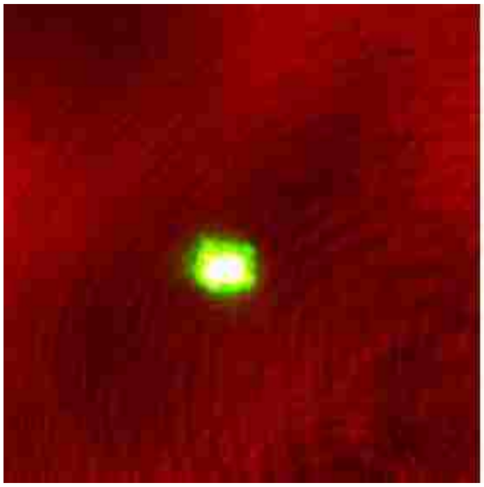

Figure 4-20: Example image of large particle showing distorted edges due to scattered laser light.

Particle temperature measurements, taken with the Flir IR camera system, present the largest source of uncertainty in this work. The approximate diffraction-limited resolution power of this system is 6 µm. From Figure 4-12, this falls approximately in the middle of the range of petcoke ash particles measured and is larger than the average particle size measured for each other type (black liquor, 3.4 µm; wood dust, 3.9 µm; petcoke ash, 4.5 µm). However, although this system cannot completely resolve particles smaller than about 6 µm, it is not necessary to resolve these particles to obtain accurate temperature measurements. The temperature measurement technique used in this work, a modified 2-color pyrometry, requires only that an energy signal for each filter be obtained and that there are no chromatic aberrations in this image. Mirrors and achromatic lenses, as used in this camera system, eliminate or minimize chromatic aberrations. The ratio of the signals with each filter according to Equation 3-5, does not depend on particle size. The uncertainties in focus and ensuring that only one particle is imaged during temperature measurements remain, however. This is difficult because of the system’s diffraction limit, which causes multiple small particles to appear as a single large particle. The steps outlined in Section 3.5.2 (Temperature Measurement) help reduce uncertainty in the temperature measurements. The nonlinearity of the IR camera system response at low temperatures presented another possible source of error. However, proper calibration eliminates this error. Section 3.5.2 (Temperature Measurement) within the Experimental Methods section details this calibration. Ultimately, the largest limitation is the signal-to-noise ratios. This system operates at low signal-to-noise ratios and this is the largest single source of error in the measurements when measured temperatures are only slightly above room temperature.

5 Opaque Particle Levitation Mechanism

5.1 Summary of Mechanism

The presented results and observations establish the mechanism for optical levitation of opaque particles. The complete mechanism is summarized as follows:

Solid, opaque particles introduced near the focal point of a visible or near-infrared laser beam experience a surface temperature rise due to absorption of the incident laser light. This heating induces a natural convective flow that generates a drag force on the particles. Simultaneously, the particle experiences a photon force in the direction of beam propagation due to the absorption and scattering of incident photons. This photon force commonly makes a small contribution to counteracting the weight, which is primarily counteracted by the convective drag force. This is why particles can be suspended with any beam orientation. However, the transverse component of the photon force is the major contributor to stabilizing the particle laterally in the beam, and this stabilization is based on asymmetries of light scattering in off-axis particles. Very small particles, such as dust in the air, have nearly symmetric forward and reverse scattering patterns and are not effectively trapped in or otherwise perturbed by the beam. Similarly, 1-10 μm particles in long-wavelength (infrared) lasers have symmetric scattering patterns and are similarly not stabilized. The induced convective drag force dominates the trapping mechanism for particles with relatively low densities and high emissivities; otherwise the drag and photon forces may be comparable. Other forces exist in the optical trap in certain orientations, but in most cases these forces are negligible.

6 Evaluation of Levitation as a Diagnostic Tool

This section comments on the levitation technique and its suitability as a diagnostic tool separately.

6.1 Particle Levitation Model

Although the optical trapping mechanism for transparent particles in water (optical tweezers) represents a well-established diagnostic, a satisfactory mechanistic description and diagnostic demonstration for trapping of opaque particles in the manner discussed here has thus far not appeared in the literature. The first contribution of this project is a mechanistic understanding of opaque particle levitation. The previous section provides a comprehensive explanation of this mechanism. The Particle Levitation Model establishes this mechanism by predictions of particle surface temperature and magnitudes of the photon and induced convective drag forces that a particle of a given size experiences while optically trapped. Experimental results validate this model and the proposed mechanism. The mechanistic understanding of this technique provides the framework around which this diagnostic tool is built. Additional work to provide a more comprehensive evaluation of this technique to solid fuel particles and the range of conditions under which it is effective continues under the direction of other investigators in the same laboratory. However, this project clearly demonstrates the ability to levitate a wide range of particles under many conditions.

6.2 Diagnostic System to Evaluate Particle Properties

This technique may enable particle investigations with greater accuracy and ease and at reduced experimental cost relative to many alternatives. Therefore, another major contribution of this research is the foundation for an *in situ* diagnostic system that characterizes fuel properties, namely particle size, shape, temperature and possibly mass, as continuous functions of time.

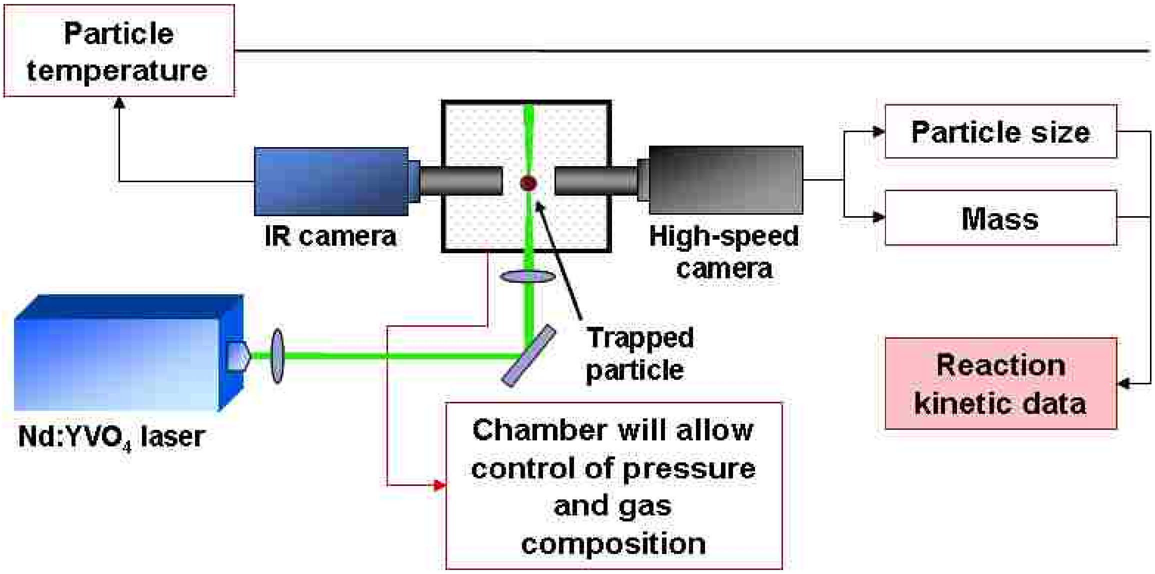

Figure 6-1: Diagnostic system to characterize single particle reaction kinetics using optical levitation.

This tool is ideally suited to investigate the time, temperature, pressure, and particle type dependencies of reactivities, product formation, and particle dynamics during gasification, combustion, and catalytic reaction. The typical system appears in Figure 6-1. The ability to perform fuel characterization on any given fuel with a noninvasive system and especially as a constant function of time in arbitrary environments of composition and temperature will expedite solid fuel characterization. [5-7, 31, 41, 43-45]

This technique indeed has some limitations. The most obvious limitation is particle size. Model and experimental results indicate that particles much larger than about 10 µm in diameter would be very difficult to trap with this system. Certain biomass particles, black liquor for example, are quite well suited for this technique; other particles are clearly outside of the capabilities of opaque particle levitation by laser levitation alone. Current follow-on efforts in this project are investigating aerodynamically assisted levitation and have demonstrated capabilities to levitate particles of several hundred microns. Because of the subtle balance of each of the forces, this technique cannot investigate particles that exhibit extensive jetting, which sometimes occurs during the initial stages of combustion. However, non-jetting fuels and chars of jetting fuels represent well-suited particles for this technique.

Aside from these limitations, this diagnostic has several significant advantages. Its most distinguishing feature is its ability to investigate individual, micron-sized particles over their entire lifetime and under arbitrary conditions of temperature and pressure. Single-particle investigations can resolve subtle changes in reactivity and other behavior on a particle-to-particle basis. This includes changes in reactivities between similar fuels, or even between particles within the same fuel sample. Currently, gas temperature, composition, and especially pressure regimes represent difficult experimental measurements (or at least require large, costly equipment) and commonly produce conflicting results. This diagnostic tool may allow easier and more accurate access to these temperature, composition and pressure regimes. Finally, although this technique cannot completely simulate commercial conditions, it enables investigations of conditions similar to commercial processes, such as gasification and oxyfuel combustion.

Particle levitation of opaque particles is also uniquely suited for light scattering investigations. The ability to suspend solid particles and investigate light scattering and interactions will provide a means to better characterize atmospheric aerosols and particulates.

7 Conclusions and Recommendations

The major conclusions and recommendations from this work appear below in that order.

7.1 Conclusions

This project provides a theoretical and experimental basis for laser levitation of single particles and demonstrates application of the technique to obtain particle size and temperature. These represent the first and most comprehensive analyses and experimental demonstrations to date. The project demonstrated levitation of many opaque particle types under many conditions. A few other laboratories have done similarly as discussed in the literature review. The project also, for the first time, developed a theoretical mechanistic and quantitative framework to describe such levitation and developed experimental data that compares favorably with the predictions of this framework.

The ultimate objective of this work, which extends beyond the scope of a single dissertation, is to enhance understanding of single-particle reactions in, for example, gasification, combustion, and catalysis applications. The work documented in this project contributes substantially to the development of this tool by providing characterizations of all particle properties needed to determine isolated, single-particle reactivities in a controlled environment. The results of these investigations may be extrapolated to commercial conditions, which have application in combustion of small particles, including coal, biomass, ash, metals, and some energetic materials.

The *in situ* diagnostic system based upon optical trapping of solid fuel particles as described in the previous section is far from completion; nevertheless, this work represents significant progress towards that goal. The Particle Levitation Model accurately quantifies the most significant forces involved in the levitation of opaque particles: the natural convective drag force and the photon force. It establishes the drag force as the dominant force in the trapping mechanism. Previous work observed these phenomena and measured convective drag forces, and this research clearly provides new data and observations to those obtained in such investigations. Furthermore, the Particle Levitation Model provides a complete mechanistic understanding of this technique consistent with previous data and observations.

The Particle Levitation Model agrees with results from two experimental techniques developed to measure accurate sizes and temperatures of very small, low-temperature particles. The particle magnification method developed in this work follows changes in particle size, position, and shape. The temperature measurement technique developed for this work measures particle temperatures only slightly exceeding ambient conditions. These techniques enable measurements of reliable data under well-controlled conditions previously difficult to investigate in the context of combustion analysis.

Additionally, the particles studied in this work represent a wide range of physical and optical properties and provide validation of the conclusions of the Particle Levitation Model. Therefore, these conclusions should include particles of similar properties.

7.2 Recommendations for Future Work

The sources of error in this diagnostic technique under controlled conditions include low signal-to-noise ratios in temperature measurements and light-scattering issues in size measurements, with the former representing by far the largest concern for the range of temperatures typically encountered. The comprehensive mechanistic understanding of optical trapping of opaque particles discussed here provides a framework from which a more complete and robust diagnostic may develop. This discussion concludes with several recommendations for future work to fully capitalize on the capabilities of this procedure:

- Include pressure dependence within the Particle Levitation Model in order to evaluate model agreement with low-pressure observations and to make the model more comprehensive.
- Evaluate the technique's capabilities with a broader range of particle size, type, and properties.
- Improve the temperature measurement technique, possibly with additional optics and/or more powerful lenses, to make it more accurate and provide greater sensitivity and resolution.
- Measure mass loss of individual particles by an overall force balance.
- Validate particle size measurements with more narrowly distributed particles.
- Develop the diagnostic as depicted in Figure 6-1 within a pressure vessel with the ability to control gas pressure and composition, thus allowing reaction kinetic investigations.

- Explore the application of this technique to heat capacity, thermal conductivity, and light scattering investigations.

8 References

1. http://www.eia.doe.gov. *Energy Information Administration*. [Internet] 2005 [cited 2005 July 14, 2005]; Available from: http://www.eia.doe.gov/.

2. Turns, S.R., *An introduction to combustion: concepts and applications*. 2nd ed, ed. K.T. Kane. 2000, Boston, MA: McGraw-Hill. 676.

3. http://www.ucsusa.org/global_environment/global_warming. *Union of Concerned Scientists: Global Environment*. 2005 [cited 2005 July 15, 2005]; Available from: http://www.ucsusa.org/global_environment/global_warming.

4. http://www.eia.doe.gov/cneaf/alternate/page/renew_energy_consump/table1.html. *U.S. Energy Consumption By Energy Source*. 2008 [cited 2008 October 29, 2008].

5. http://www.eia.doe.gov/oiaf/ieo/world.html. *International Energy Outlook 2008*. 2008 [cited 2008 October 29, 2008].

6. http://www.eia.doe.gov/cneaf/solar.renewables/page/wood/wood.html. *Energy Information Administration*. 2005 [cited 2005 December 19, 2005].

7. Zhao, B., D. Katoshevski, and E. Bar-Ziv, *Temperature determination of single micrometre-sized particles from forced/free convection and photophoresis.* Measurement Science and Technology, 1999. **10**: p. 1222-1232.

8. Bar-Ziv, E. and G.d. Botton, *The motion of a charged particle in an electrodynamic chamber under feedback control.* Aerosol Science and Technology, 2001. **15**: p. 1-7.

9. Zhao, B. and E. Bar-Ziv, *Further development of temperature determination for a heated micron-sized particle from forced convection.* Journal of Aerosol Science, 2002. **33**: p. 165-180.

10. Mograbi, E. and E. Bar-Ziv, *Dynamics of a spherical particle in mixed convection flow field.* Journal of Aerosol Science, 2005. **36**(3): p. 387-409.

11. Ashkin, A., *Optical trapping and manipulation of neutral particles using lasers.* The National Academy of Sciences of the USA, 1997. **94**: p. 4853-4860.

12. http://fy.chalmers.se/f3a/tweezers/basics.html. *Basics of optical traps*. [Internet] 2003 [cited 2003 July 2003]; Available from: http://fy.chalmers.se/f3a/tweezers/basics.html.

13. Ashkin, A., *Atomic beam deflection by resonance-radiation pressure.* Physical Review Letters, 1970. **25**(19): p. 1321-1324.

14. Ashkin, A., *Applications of laser radiation pressure.* Science, 1980. **210**(4474): p. 1081-1088.

15. Ashkin, A., *Acceleration and trapping of particles by radiation pressure.* Physical Review Letters, 1970. **24**(4): p. 156-159.

16. Ashkin, A. and J.M. Dziedzic, *Optical levitation by radiation pressure.* Applied Physics Letters, 1971. **19**(8): p. 283-285.

17. Ashkin, A. and J.M. Dziedzic, *Stability of optical levitation by radiation pressure.* Applied Physics Letters, 1974. **24**(12): p. 586-588.

18. Agayan, R.A., F. Gittes, R. Kopelman, and C.F. Schmidt, *Optical trapping near resonance absorption.* Applied Optics, 2002. **41**: p. 2318-2327.

19. Lock, J.A., *Calculation of the radiation trapping force forlaser tweezers by use of generalized Lorenz–Mie theory. I. Localized model description of an on-axis tightly focused laser beam with spherical aberration.* Applied Optics, 2004. **43**(12): p. 2532-2544.

20. Lock, J.A., *Calculation of the radiation trapping force for laser tweezers by use of generalized Lorenz-Mie theory. II. On-axis trapping force.* Applied Optics, 2004. **43**(12): p. 2545-2554.

21. Ashkin, A. and J.M. Dziedzic, *Optical levitation in high vacuum.* Applied Physics Letters, 1976. **28**(6): p. 333-335.

22. Ashkin, A. and J.M. Dziedzic, *Feedback stabilization of optically levitated particles.* Applied Physics Letters, 1977. **30**(4): p. 202-204.

23. Gahagan, K.T. and G.A. Swartzlander, *Optical vortex trapping of particles.* Optics Letters, 1996. **21**(11): p. 827-829.

24. Chylek, P., J.T. Kiehl, and M.K.W. Ko, *Optical levitation and partial-wave resonances.* Physical Review A, 1978. **18**(5): p. 2229-2233.

25. MacDonald, M.P., L. Paterson, W. Sibbett, and K. Dholakia, *Trapping and manipulation of low-index particles in a two-dimensional interferometric optical trap.* Optics Letters, 2001. **26**(12): p. 863-865.

26. Gouw, J.A.d., *Laser levitation studies of the physical and chemical properties of single atmospheric aerosols*, Institute for Marine and Atmospheric Research Utrecht: Princetonplein, Utrecht.

27. Lewittes, M. and S. Arnold, *Radiometric levitation of micron sized spheres.* Applied Physics Letters, 1982. **40**(6): p. 455-457.

28. Pluchino, A.B., *Radiometric levitation of spherical carbon aerosol particles using a Nd:YAG laser.* Applied Optics, 1983. **22**(12): p. 1861-1866.

29. Huisken, J. and E.H.K. Stelzer, *Optical levitation of absorbing particles with a nominally Gaussian laser beam.* Optics Letters, 2002. **27**(14): p. 1223-1228.

30. Bellville, B., *Optical Trapping*, in *Physics and Astronomy*. 2003, Brigham Young University: Provo, Utah. p. 27.

31. Bliss, C., *Optical Trapping*, in *Physics and Astronomy*. 2004, Brigham Young University: Provo, Utah. p. 20.

32. Shulimanova, Z.L., E.R. Shchukin, and T.M. Eremchuk, *Photophoresis of moderately large solid spherical particles with a thermal conductivity that depends on the radial coordinate.* Technical Physics Letters, 1996. **22**(9): p. 747-748.

33. Watarai, H., H. Monjushiro, S. Tsukahara, M. Suwa, and Y. Iiguni, *Migration analysis of micro-particles in liquids using microscopically designed external fields.* Analytical Sciences, 2004. **20**: p. 423-434.

34. Pluchino, A.B., *Photophoretic force on particles for low Knudsen number.* Applied Optics, 1983. **22**(1): p. 103-106.

35. Levdansky, D., Measurement Science and Technology, 1995. **8**: p. 875.

36. Davis, E.J. and R. Zheng, *Phoretic force measurement for microparticles under microgravity conditions*, University of Washington, Department of Chemical Engineering: Seattle, WA. p. 209-214.

37. http://en.wikipedia.org/wiki/Crookes_radiometer. *Crookes radiometer*. 2002 [cited 2006 November 2006]; Available from: http://en.wikipedia.org/wiki/Crookes_radiometer.

38. http://math.ucr.edu/home/baez/physics/General/LightMill/light-mill.html. *How does a light-mill work?* 1996 1997 [cited 2006 December 2006]; Available from: http://science.howstuffworks.com/framed.htm?parent=question239.htm&url=http://math.ucr.edu/home/baez/physics/General/LightMill/light-mill.html.

39. Woodruff, A.E., *The Radiometer and How it Does Not Work.* The Physics Teacher, 1968. **6**: p. 358--363.

40. Lu, Z., *Experimental and numerical study of the optimal operation pressure within Crookes radiometer*. Journal of Vacuum Sci. Technol. A, 2005. **23**(6): p. 1531-1534.

41. Scandurra, M., *Enhanced radiometric forces*. 2006, Massachusetts Institute of Technology: Cambridge, MA.

42. Hecht, E., *Optics*. 3rd ed. 1998, Reading, MA: Addison-Wesley.

43. Friese, M.E.J., J. Enger, H. Rubinsztein-Dunlop, and N.R. Heckenberg, *Optical angular-momentum transfer to trapped absorbing particles.* Physical Review A, 1996. **54**(2): p. 1593-1596.

44. Spjut, R.E., A.F. Sarofim, and J.P. Longwell, *Laser-Heating and Particle Temperature-Measurement in an Electrodynamic Balance.* Langmuir, 1985. **1**(3): p. 355-360.

45. Zhang, X. and E. Bar-Ziv, *Direct determination of 3D forces applied on a particle suspended in an electrodynamic chamber.* Measurement Science and Technology, 1996. **7**: p. 1713-1720.

46. Dudek, D.R., T.H. Fletcher, J.P. Longwell, and A.F. Sarofim, *Natural convection induced drag forces on spheres at low Grashof numbers: comparison of theory with experiment.* International Journal of Heat and Mass Transfer, 1988. **31**: p. 863-873.

47. Bar-Ziv, E., *Physicochemical processes of single liquid and solid particles in an electrodynamic chamber*, Nuclear Research Center - Negev and Ben-Gurion University of the Negev: Beer-Sheva, Israel.

48. Barziv, E. and A.F. Sarofim, *The Electrodynamic Chamber: A Tool for Studying High-Temperature Kinetics Involving Liquid and Solid Particles.* Progress in Energy and Combustion Science, 1991. **17**(1): p. 1-65.

49. Baum, D., Y. Har-Nov, H. Guterman, and E. Bar-Ziv, *A robust particle position controller for an electrodynamic chamber.* Rev. Sci. Instrum, 1993. **64**(12): p. 3627-3633.

50. http://en.wikipedia.org/wiki/Oil-drop_experiment. *Oil-drop experiment*. 2008 [cited 2008 June 14, 2008]; Available from: http://en.wikipedia.org/wiki/Oil-drop_experiment.

51. Bar-Ziv, E., B. Zhao, E. Mograbi, D. Katoshevski, and G. Ziskind, *Experimental validation of the Stokes law at nonisothermal conditions.* Physics of Fluids, 2002. **14**(6): p. 2015-2018.

52. Barziv, E., D.B. Jones, R.E. Spjut, D.R. Dudek, A.F. Sarofim, and J.P. Longwell, *Measurement of Combustion Kinetics of a Single Char Particle in an*

Electrodynamic Thermogravimetric Analyzer. Combustion and Flame, 1989. **75**(1): p. 81-106.

53. Damore, M., L. Tognotti, and A.F. Sarofim, *Oxidation Rates of a Single Char Particle in an Electrodynamic Balance.* Combustion and Flame, 1993. **95**(4): p. 374-382.

54. Dudek, D.R., D.A. Wright, J.P. Longwell, A.F. Sarofim, and J. Yeheskel, *Charge Loss from Heated Particles Levitated in an Electrodynamic Balance.* Combustion Science and Technology, 1990. **73**(1-3): p. 447-461.

55. Ip, E., A. Mackrory, L.L. Baxter, and D.R. Tree. *Comprehensive Time Dependent Black Liquor Single Droplet Experiments and Predictions*. in *2005 ACERC Conference*. 2005. Provo, Utah.

56. Lu, H., L. Werrett, M. Vickers, T. Gunderson, and L.L. Baxter. *Effects of Particle Shape and Size on Biomass Reactivity*. in *2005 ACERC Conference*. 2005. Provo, Utah.

57. Kasai, I., H.L. Hettich, and S.L. Lawrence, *Visible and infrared indium antimonide (INSB) photodetector with non-flashing light receiving surface*. 1994, Santa Barbara Research Center (Goleta, CA): United States.

58. Incropera, F.P. and D.P. DeWitt, *Fundamentals of Heat and Mass Transfer*. Fourth ed. 1996, New York: John Wiley & Sons.

59. Bogolepov, A.I., G.P. Bystrai, S.A. Beresnev, V.G. Chernyak, and G.A. Fomyagin, *Experimental and theoretical study of photophoresis in a low-density gas.* High Temperature, 1991. **29**(4): p. 587-594.

60. Bogolepov, A.I., P.E. Suetin, S.A. Beresnev, G.P. Bystrai, and V.G. Chernyak, *Photophoresis of Model Aerosol Particles.* High Temperature, 1996. **34**(5): p. 751-756.

61. Pluchino, A.B. and S. Arnold, *Comprehensive model of the photophoretic force on a spherical microparticle.* Optics Letters, 1985. **10**(6): p. 261-263.

62. Rohatschek, H., *Levitation of stratospheric and mesospheric aerosols by gravito-photophoresis.* Journal of Aerosol Science, 1996. **27**(3): p. 467-475.

63. http://jets.poudres.free.fr/index_fichiers/page0007.html. *Motion of particles (thermophoresis)*. 2005 [cited 2005 December 19, 2005].

64. Mishchenko, M.I., L.D. Travis, and A.A. Lacis, *Scattering, Absorption, and Emission of Light by Small Particles*. 2002, New York, New York: Cambridge University Press.

65. http://www.science.uva.nl/research/scs/Software/adda/. *The Amsterdam DDA.* 2006 October 14, 2006 [cited 2006 July 2006]; Available from: http://www.science.uva.nl/research/scs/Software/adda/.

66. Yurkin, M.A., V.P. Maltsev, and A.G. Hoekstra, *The discrete dipole approximation for simulation of light scattering by particles much larger than the wavelength.* J. Quant. Spectros. Radiat. Transf., 2007. **106**: p. 546-557.

67. http://en.wikipedia.org/wiki/Discrete_dipole_approximation. *Discrete dipole approximation*. 2007 [cited 2007 September 11, 2007].

68. Yurkin, M., *Radiation pressure*, S. Lewis, Editor. 2006.

69. Nieminen, T., *Radiation pressure*, S. Lewis, Editor. 2006.

70. Draine, B., *Radiation pressure*, S. Lewis, Editor. 2006.

71. Mishchenko, M.I., *Radiation pressure,* S. Lewis, Editor. 2006.

72. Yurkin, M., *Localized approximation*, S. Lewis, Editor. 2006.

73. Laven, P. *MiePlot: A computer program for scattering of light from a sphere using Mie theory & the Debye series*. 2006 October 1, 2006 [cited 2008 January 17, 2008]; Available from: www.philiplaven.com/mieplot.htm.

74. *ChEResources: Online Chemical Engineering Information*. [Internet] 2001 [cited 2007 December 2007]; Available from: www.cheresources.com/overflow.pdf.

75. Lightner, G.E., *Black liquor removed from pulp*. 2004: United States.

76. http://www.rit.edu/~andpph/photofile-c/schlieren-3659.jpg. *High speed, Schlieren and photoinstrumentation photographs*. 2006 [cited January 30, 2006].

77. http://en.wikipedia.org/wiki/Mie_theory. *Mie theory*. 2007 [cited 2007 September 11, 2007].

78. Bohren, C.F. and D.R. Huffman, *Absorption and Scattering of Light by Small Particles*. 1983, New York: John Wiley & Sons, Inc.

79. http://en.wikipedia.org/wiki/Airy_disk. *Airy disk*. 2007 [cited 2007 September 11, 2007].

80. http://www.cambridgeincolour.com/tutorials/diffraction-photography.htm, *Tutorials: Diffraction and photography*. 2006.

81. http://www.ugr.es/~jadiaz/docencia.htm, *Docencia*. 2006.

82. http://en.wikipedia.org/wiki/Transverse_mode. *Transverse mode.* 2009 [cited 2009 January 24, 2009].

83. http://en.wikipedia.org/wiki/Schlieren_photography. *Schlieren photography*. 2009 [cited 2009 January 27, 2009].

84. http://www.newport.com/servicesupport/Tutorials/default.aspx?id=112. *Gaussian Beam Optics Tutorial*. 2009 [cited 2009 January 27, 2009].

85. http://www.photonics.com/dictionary/lookup/XQ/ASP/url.lookup/entrynum.2170/letter.g/pu./QX/lookup.htm. 2009 [cited 2009 January 27, 2009].

Appendix A. Unsuccessful Experimental Methods

"I have not failed. I've just found 10,000 ways that won't work."

– Thomas Edison

"Just because something doesn't do what you planned it to do doesn't mean it's useless."

– Thomas Edison

"An expert is a person who has made all the mistakes that can be made in a very narrow field."

– Neils Bohr

Several different techniques and data collection procedures were attempted during the evaluation of this diagnostic that were ultimately unsuccessful. Although certainly disappointing, valuable insights and understanding were gained with each failure and the fact that they did not work was an important result itself. These observations led to a more accurate determination of the particle levitation mechanism and a more complete evaluation of the limits of this diagnostic tool. The following sections describe these techniques and resultant observations and conclusions.

Aerodynamically Assisted Particle Suspension

The levitation of particles larger than about 10 µm in diameter requires forces greater than those a particle experiences during laser levitation. Aerodynamically assisted particle suspension attempted to do this by utilizing the Bernoulli Effect to stabilize particles by passing a steady air stream past particles in order to increase the effective drag force to suspend particles. Compressed air passed through a regulator and a needle valve into a glass nozzle made by heating glass tubing over a flame and drawing the glass to a fine tip. Small funnels were used in conjunction with the glass nozzles to help stabilize the particles and the airflow.

Of the particles attempted, many were successfully suspended, but none smaller than 600 µm. Suspending particles smaller than this requires near perfectly spherical particles. Levitation of 600 µm particles was achieved using a nozzle with an aperture of about 100 µm. Attempts at levitating particles smaller than 100 µm were frustrated by the particle's size, making it difficult to introduce them into the stream and making them nearly impossible to see and track thereafter. Once the proper air flow was determined, particles remained stably suspended indefinitely.

The major challenges with this technique are the ability to accurately control the air flow and the ability to adequately monitor the suspended particles. Despite these challenges, this technique should be further explored in order to aerodynamically suspend particles in the range of 10-100 µm in diameter. With the increased drag force, these particles could be externally heated, possibly by laser radiation, and studied without being constrained by particle size or optics capabilities.

Helium/Hydrogen Gas Immersion

This technique was employed with the intent to more firmly establish the free-convective drag force as the major component in the trapping mechanism. Because the drag force in Stokes regime is directly proportional to the viscosity of the ambient gas according to $C_d = 24/Re$, increases in the dynamic viscosity should cause the particle to move upward in the optical trap and vice versa. Thus, changing the ambient gas should cause suspended particles to change position when immersed in a gas with a sufficiently different viscosity. This was done by trapping particles in an inverted, transparent glass test tube and taking images of the particle position when trapped stably. The test tube was then filled with either H_2 or He gas and new images of the particle's position were taken. Comparing these images indicated that the particles would move when the new gases were introduced, however, they did not move significantly or consistently enough to give conclusive evidence that the free-convective drag force is the dominant force in the mechanism. The major challenges with this method are 1) introducing the second gas without disturbing the particle, 2) controlling the level of the second gas, and 3) adequately resolving changes in particle position. Similar experiments may be performed when a fully-sealed vessel is available.

Schlieren Imaging

Although the optical trapping mechanism has been established by both the Fluent and mathematical models, visualization of the convective flow pattern around the trapped particles will provide substantial validation to the trapping mechanism. A Schlieren imaging system best accomplishes this. The details of such a system were researched and implemented to further establish the hypothesized trapping mechanism. Schlieren imagery operates on the concept that a fluid has different indices of refraction for different densities [83]. This allows visualization of convective flows or flows in which there exist significant temperature or pressure gradients (Figure 8-1).

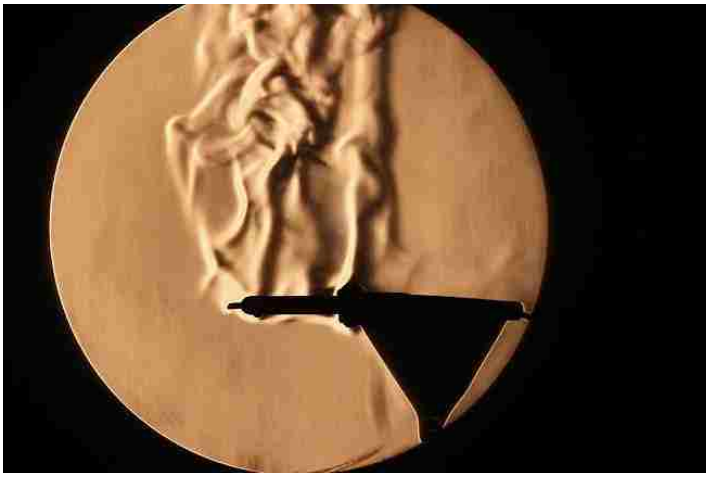

Figure 8-1: Example Schlieren image used to visualize hot air currents [76].

Particle Sizing Attempts

Mie scattering can provide a very accurate measurement of particle size. Mie theory provides a complete analytical solution to Maxwell’s equations for scattering of electromagnetic radiation from spherical particles, valid for any d_p/λ [77, 78]. Significant effort was focused on determining particle size by the airy rings generated by a laser incident upon a suspended particle (Figure 8-2). Airy rings (also referred to as Fraunhofer rings) are characteristic of diffraction through small apertures or by small particles. The concentric rings of the airy disk indicate particle size by the angle between each successive ring, according to the formula $sin\ \theta = 1.22 \cdot \lambda / d_p$ [79]. Similar patterns may be generated using a pinhole. Trapped particles were illuminated with a 633 nm He-Ne laser and the scattered laser light was viewed on a white background. However, despite extensive effort, no recognizable ring pattern was detected. It was determined that the particles are not sufficiently spherical to generate the expected scattering pattern.

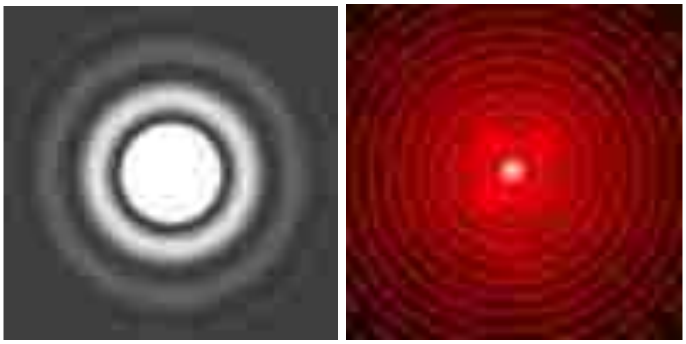

Figure 8-2: Examples of airy rings; *left*, computer generated and, *right*, generated by a He-Ne laser through an aperture [80, 81].

A power meter from Gentec was later purchased to measure the laser intensity with and without suspended particles. The difference could be attributed to the energy absorbed by the trapped particles. A size could theoretically be calculated based upon the energy absorbed by the particles. The meter sampled laser intensity every 100 ms and the results we saved as a text file and exported to Excel. Although there was some difference detected, this difference was not greater than the drift measured from both the laser and the power meter. The differences between average intensities over periods with and without trapped particles were never consistent enough, although statistically significant, to give us confidence that the resulting sizes were accurate.

Another unsuccessful attempt was the use of a microscope reticle (1 mm with 0.01 mm divisions) to measure the camera's field of view at different magnifications and frame rates. The 532 nm laser was used to illuminate the edge of a razor blade at various beam intensities to determine the extent to which the reflected laser light would distort particle size (Figure 8-3).

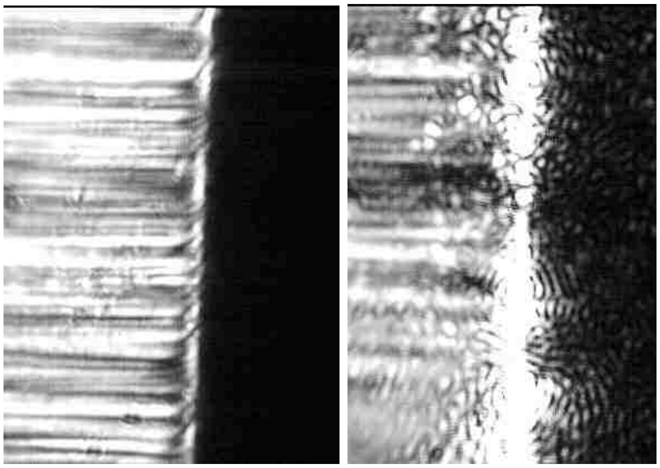

Figure 8-3: *Left,* razor blade with no laser illumination; *right,* razor blade illuminated by 532 nm laser at 0.5 watts.

The reflected light created an uncertainty of about 2-4 µm with the razor blade. Particle pictures were then taken and compared to the calibrated field of view as shown in Figure 8-4. The problem with this technique was that the camera was imaging the scattered laser light by the particles. Therefore, changing exposure time changed the apparent size of the particles: shorter exposure times produce smaller particles and vice versa. This method could work if used consistently at a given exposure time and calibrated for that setting; however, each setting would have to be individually calibrated and the technique needed to be more versatile.

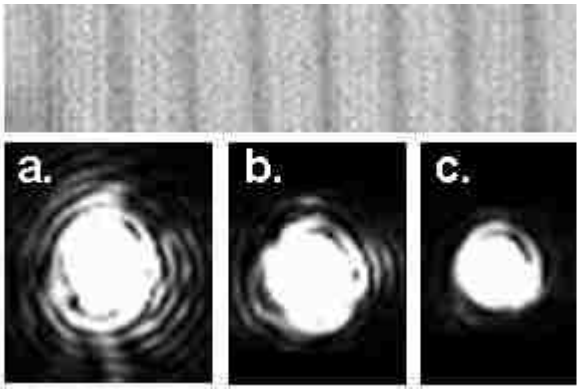

Figure 8-4: Black liquor particles: *a)* 12 µm, *b)* 11 µm, and *c)* 10 µm in diameter. Micrometer scale shown in 10 µm intervals.

CO_2 Laser Configuration

A Synrad CO_2 laser (10.6 µm, 50-watt maximum output) may be regulated down to 10-15 Watts to heat the particles. As described above, the 532 nm laser suspends the particles, the optics are arranged to split the CO_2 beam and heat the particles symmetrically as shown in Figure 8-5. The mirrors (M1-M4) are silicon, 1.0-inch in diameter and 0.118-inches thick. The 50/50 beam splitter is zinc-selenide, 1.0-inch in diameter and 0.08-inches thick.

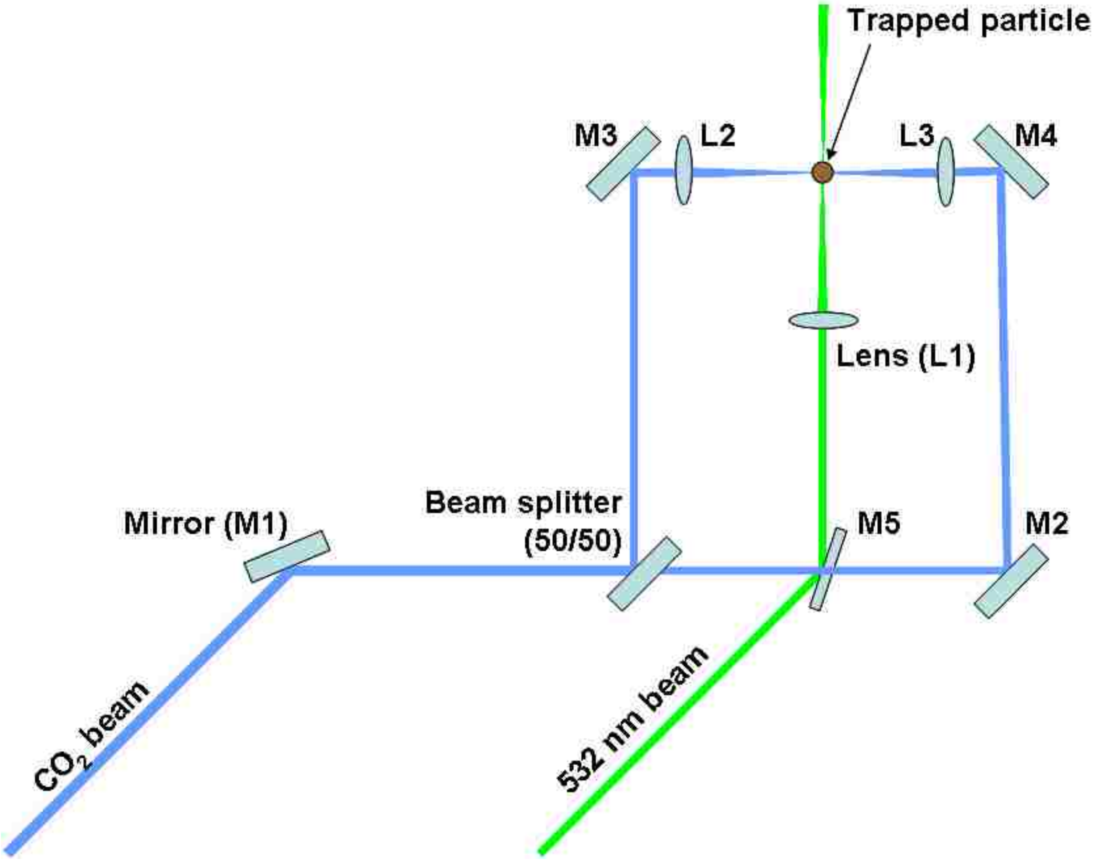

Figure 8-5: Arrangement of optics with CO_2 beam used to heat suspended particles.

Aligning the CO_2 beam to heat the particles, as illustrated in Figure 8-5, is difficult and extremely tedious. Several methods were attempted to view the IR beam during alignment. Typical IR viewers, including military-issued night vision goggles, only amplify the available light and detect wavelengths up to about 1000 nm. An IR camera, which detects up to about 13 µm, was employed to detect the beam but found that the risk of damaging the camera's detector because of the beam intensity was too great. After all of these efforts, it was determined that the best option was to align the beam using small cards to indicate the location of the beam periodically.

Particle Trapping with the CO_2 Beam

Previous attempts were conducted to levitate particles with the CO_2 beam, but new understanding that particles are much more stable when the beam is expanded to its largest possible diameter when transmitted through the focusing lens prompted further investigation. Expanding the focusing beam provides a smaller focal point. Another lens was used to expand the beam. A power meter helped to regulate laser power. The laser output power was kept at 2 watts or lower. Three configurations attempted to trap particles: horizontal, vertically upward, and angled upward.

The horizontal and vertically upward arrangements were tried initially. The CO_2 laser operates by pulsed width modulation, with the aperture never being open more than about 95% of the time. To make the beam truly continuous, a 5.5-6 volt signal was connected directly to the laser instead of using the control box. With this modification, the vertically upward and angled upward beams were used to trap particles. Despite these efforts, particles never successfully trapped using the CO_2 beam. When passed through the focus, particles would consistently be knocked off of the needle, but none would remain levitated. This observation can be explained in greater detail by Section 4.1.4 “Radiation Pressure: Prediction with Scattering Code” in the body of this work. As outlined in this section, particle diameter was approximately equal to (and in most cases smaller than) the wavelength of the CO_2 laser (10.6 µm). Thus, the forces a particle experiences with this beam are likely very different than those operative with the 532 nm beam where $d_p/\lambda >> 1$, preventing particle levitation.

Heating Particles

One final attempt was made to heat particles with the CO_2 beam. The 532 nm beam trapped the particles, which were then imaged by a CCD camera and monitored by live video. Despite extensive efforts, particles could not be successfully heated the with the CO_2 beam due to the difficulty aligning the invisible beam. Although the particles were occasionally knocked out of the trap, this did not happen consistently. Due to these difficulties, further experiments to heat the trapped particles were continued only with the 532 nm beam.

To heat the particles, the 532 nm Verdi laser was set to the maximum power (10.5 watts). A beam splitter allowed approximately 5% of the beam power to trap the particles and the other 95% to heat them. Because of losses through the various optical components, about 70 mW was delivered for trapping and about 7 watts for heating. After aligning the beams, the high-speed camera captured particle behavior as the heating beams were applied. Several videos appeared to show the particles begin to swell, which is characteristic of black liquor. Most particles remained in the field of view for about 10 ms. The force from the laser light and probably jetting from the particles as they were heated and began to pyrolyze caused this behavior. Particles were observed swelling up to approximately 3 times the original diameter while in the field of view.

Because of the very brief time (10 ms) that the particles remain in the camera field of view and thus in the focus of the heating beams, the heating rate had to be increased in order to capture complete particle combustion. This was done by using additional mirrors and lenses to focus, reflect, and then refocus the beam upon the particles. As illustrated in Figure 8-6, the beam was focused on the particle four times, effectively doubling the heating rate from the previous arrangement.

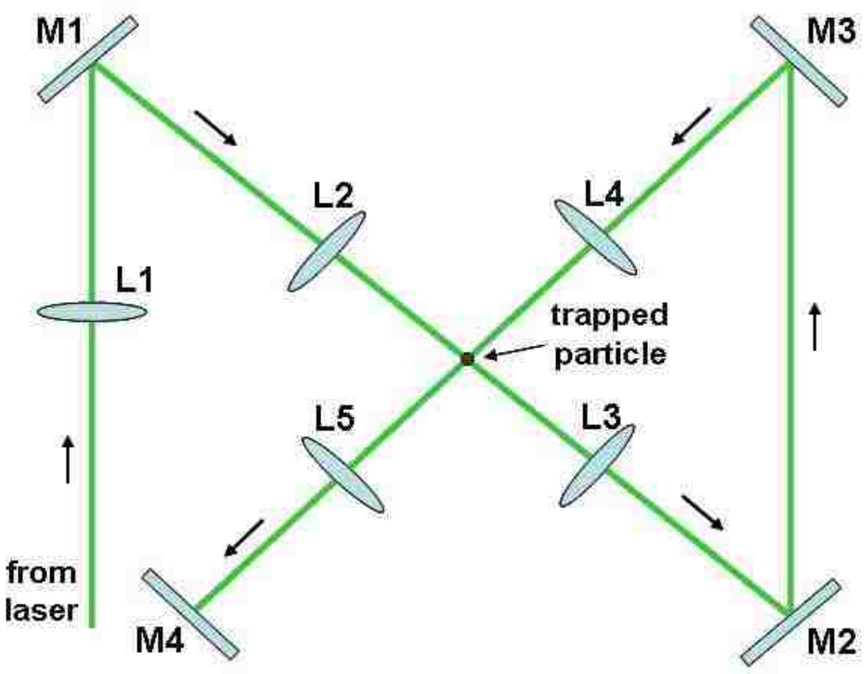

Figure 8-6: Arrangement to increase heating rate.

The beam shown is the 95% portion of the beam. It passed through the first lens (L1) to collimate the beam. The first mirror (M1) reflected the beam through the second lens, which focused the beam upon the particle. The beam then passed through the third lens, which collimated the beam again. The beam was then reflected to the third mirror, which directed the beam through the fourth lens. This lens focused the beam upon the particle again and the beam was then collimated by the fifth lens. Finally, the fourth mirror reflected the beam back through the original path. The mirrors that collimated the beam on the first pass then focused the beam upon the particle and vice versa. Thus the beam was focused upon the particle four times.

The current work established the viability of heating suspended particles by this technique; however, the study of particle combustion by this method is left for future work.

High-Speed Camera Characterization

The Fastcam 1024 PCI by Photron has 17 µm pixels, 1024x1024 resolution, and a 10-bit CMOS sensor. It is capable of 1,000 frames-per-second (fps) at full-resolution and up to 109,500 fps at reduced resolution. This camera was obtained primarily to measure particle surface temperature and to monitor particle dynamics during combustion experiments.

In order to measure temperature, the camera spectral response was obtained from Photron (Figure 8-7). It indicates significant sensitivity in the infrared. However, early evaluation of the camera response quickly revealed that an IR-filter prevents any response above about 700 nm, thus making the manufacturer’s spectral response invalid. This section details the method used to measure the actual spectral response.

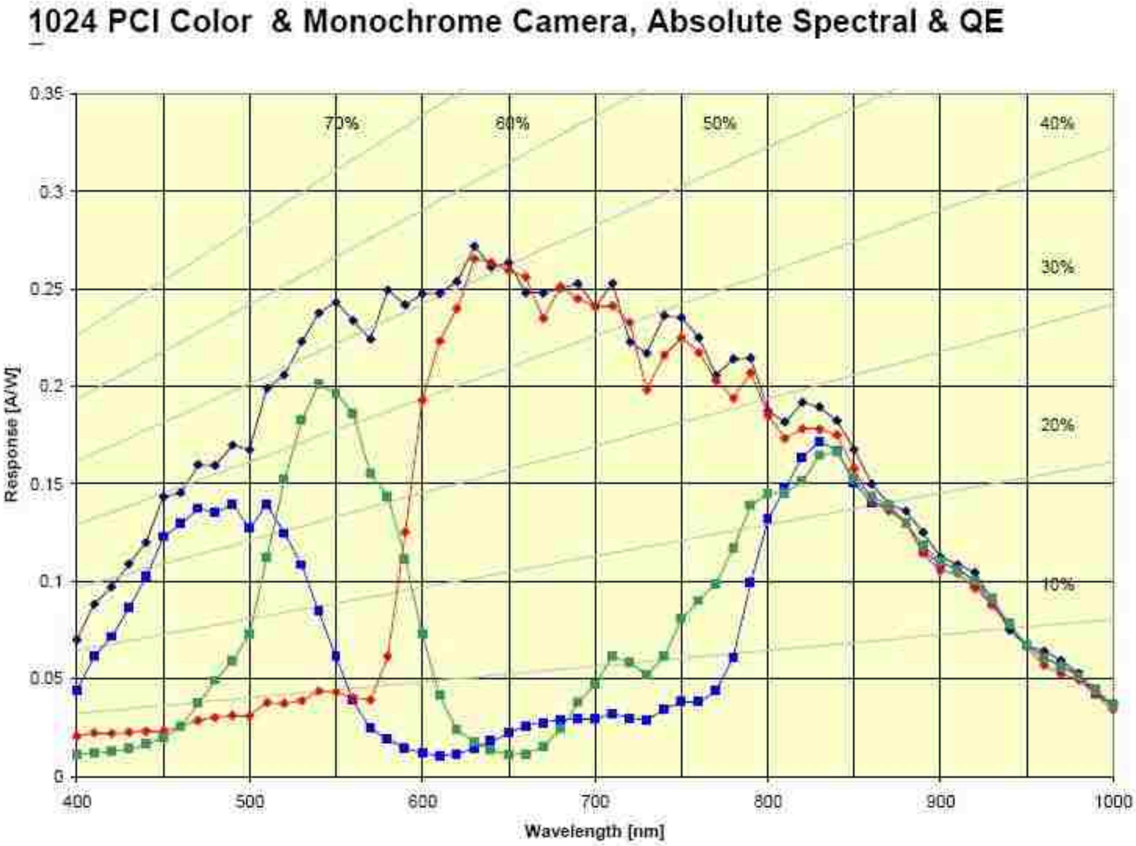

Figure 8-7: Manufacturer's spectral response for Fastcam 1024 PCI.

A blackbody was used as the light source to measure the spectral response. Setting the blackbody to a constant temperature and changing the exposure time indicated that the camera sensor responds linearly (Figure 8-8). This response was typical for this camera at higher blackbody temperatures; however, at lower temperatures when there is much lower signal there is very little response in the blue channel.

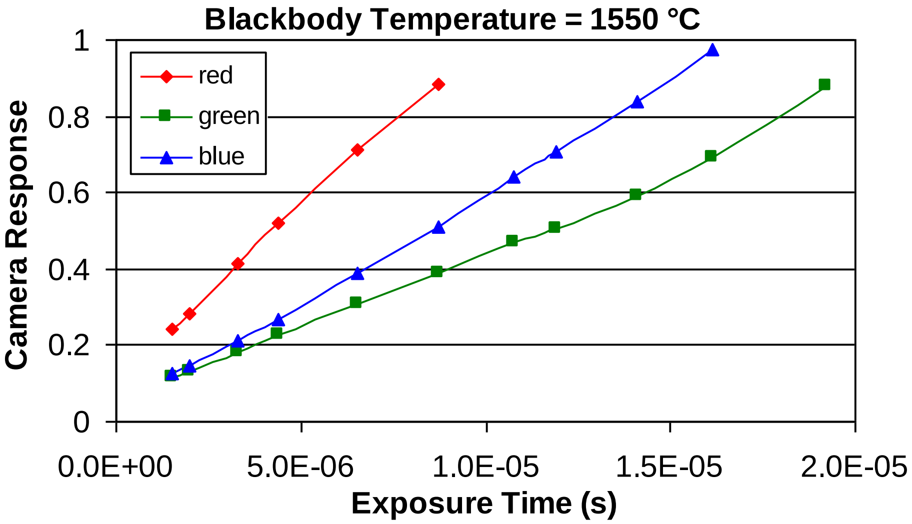

Figure 8-8: Plot showing camera's linear response with changes in exposure time for each channel (T_{BB} = 1550 °C).

After determining that the camera responded linearly, spectral response curves were obtained for the camera with two different lenses and a notch filter (Semrock, 532 nm center, 17 nm 50% bandwidth, > 6 OD). The response for the VZM 1000 (FOV 640 µm – 2.56 mm) lens is shown in Figure 8-9. The response for the 7X Precision Zoom with 50X Mitutoyo lens (FOV 25-170 µm) is shown in Figure 8-10.

During calibration, it was also noted that there was very little usable, overlapping data between the three channels below about 1300 °C. For example, when the red channel was not saturated, the blue or green channels do not indicate a significant response. Thus, accurate temperature measurements below 1300 °C are not possible with two-color pyrometry.

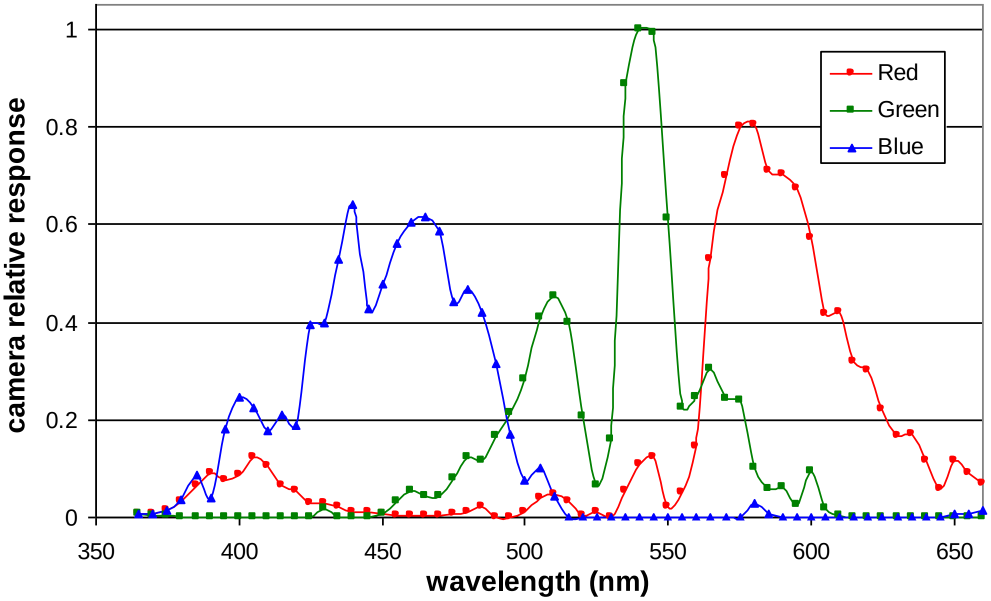

Figure 8-9: Spectral response with VZM 1000 lens, 532 nm notch filter, and a fiber optic light source.

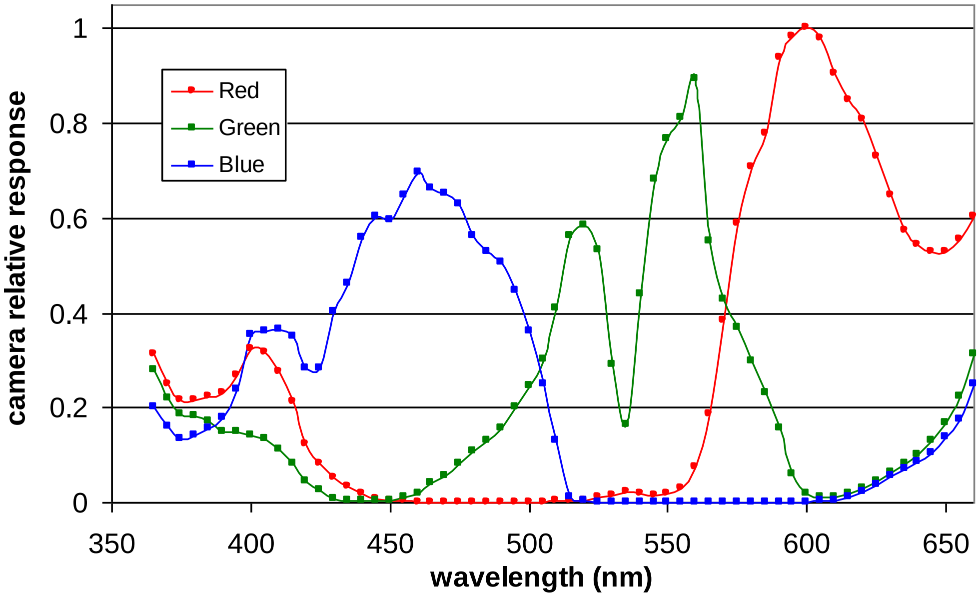

Figure 8-10: Spectral response with 7X Precision Zoom with 50X Mitutoyo lens, 532 nm notch filter, and a fiber optic light source.

Unfortunately, this camera was determined to be much less light sensitive than was expected. Within this research group there was a Sony camera that had been used for similar temperature measurements. It had 6.7 µm pixels and did not have high-speed capability (max frame rate is 15 fps). To compare light sensitivity, a small furnace was used to heat a ceramic cylinder to about 800 °C – this acted as the blackbody calibration source. The same lens was placed on each camera and the resulting pixel values and exposure times were compared with the blackbody at about the same temperature. The Sony camera showed red pixel values of about 975 or ~95% of saturation (1023 being the maximum/saturation value for a 10-bit camera) at about 6.5 ms. With the same lens, the Fastcam camera showed red pixel values of about 25 or ~10% of saturation (255 being the saturation value for an 8-bit camera) at 16.67 ms – nearly 3 times the exposure time. Values closer to saturation could be approached with the Fastcam if the exposure time could be increased, but this was not an available option and it would not affect the overall light sensitivity.

Image Magnification

In order to get more pixels across the surface of a suspended particle to increase the accuracy of the IR temperature measurements, the IR image was magnified using a pair of mirrors. The use of mirrors instead of lenses prevents chromatic aberration, which would be significant at the wavelengths the camera detects (3-5 µm). This IR camera and lens have a diffraction limit of 6.25 µm. It detected the particles fairly well, but they did not cover much more than a single pixel. An accurate temperature reading may require the particles to cover about 9 pixels (3x3) to ensure that the center pixel is completely covered by the particle. The smallest particles (~5 μm) cover much less area than this and likely indicate temperatures that are too low.

In order to get more pixels across the surface of the particle, the IR image was intended to be magnified using a pair of mirrors. The first mirror was placed one focal length away from the particle. This collimated the reflected light. The second mirror focused the collimated light from the first mirror. Image magnification is equal to F2/F1, where F1 and F2 are the focal lengths of the first and second mirrors, respectively.

The first mirror had a 2-inch focal length. The second mirror initially had a 20-inch focal length. This was quickly found to be too long because at 10X magnification, the particles did not emit enough IR light to be visible to the camera. Mirrors with 12- and 8-inch focal lengths were obtained with the same result. A thermocouple placed in the camera’s field of view and heated by the focused beam had to reach approximately 50 °C before it became visible to the camera with the 8-inch focal length mirror. Therefore, it became clear that the trapped particles were cooler than 50 °C and that magnifying the IR image with this technique was not a viable option.

Appendix B. Temperature Measurement Subroutine

IR camera spectral response:

$\mathrm{ORIGIN} := 1$ $\quad \mu m := 10^{-6} m$ $\quad nm := 10^{-9} m$

Planck's distribution: $E_b(\lambda, T) := \dfrac{C1}{\lambda^5 \cdot \left(\exp\left(\dfrac{C2}{\lambda \cdot T} \right) - 1 \right)}$

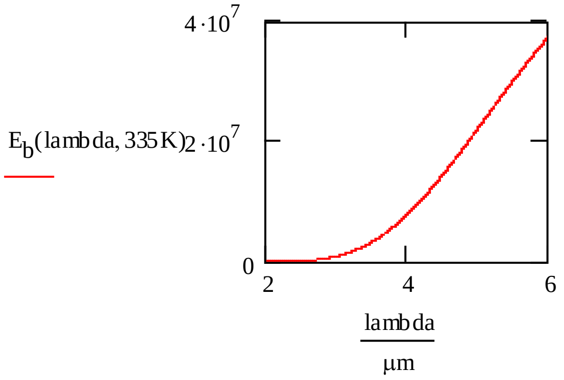

$C1 := 3.742 10^8 \cdot \dfrac{W \cdot \mu m^4}{m^2}$ $\quad C2 := 1.439 10^4 \cdot \mu m \cdot K$ $\quad \varepsilon_{tc} := 0.$

$\mathrm{lambda} := 2\mu m, 2.001\mu m .. 6\mu m$

$T_{room} := 293K$

Pixel value equation: $DN = \displaystyle\int_{\lambda_1}^{\lambda_2} \alpha \cdot \varepsilon \cdot S_{RF} \cdot E_b(\lambda, T)\, d\lambda$ $\quad \alpha = \dfrac{DN}{\displaystyle\int_{\lambda_1}^{\lambda_2} \varepsilon \cdot S_{RF} \cdot E_b(\lambda, T)\, d\lambda}$

$\mathrm{lambda2} := 1600nm, 1601nm .. 6000nm$ $\quad S_{RF}(x) := \mathrm{linterp}(\mathrm{lambda}_S, \mathrm{trans}_S, x)$

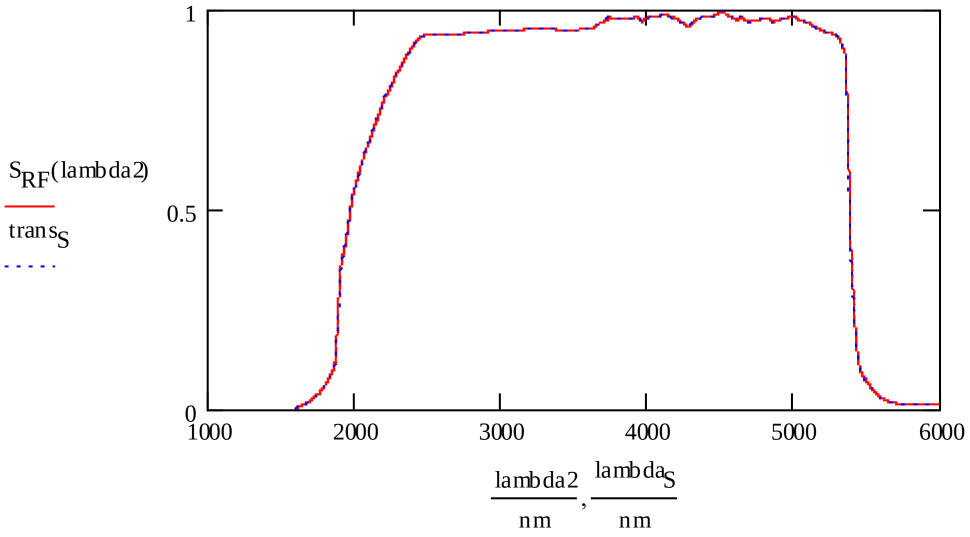

$\lambda_1 := 2475\text{nm} \qquad \lambda_2 := 6000\text{nm}$

y = 0.1306x2 - 5.9275x + 84.715

$T_{filter} := 290K, 291K..400K$

$$DN_{tot}(T) := 0.1306\left(\frac{T - 273.15K}{K}\right)^2 - 5.9275\frac{T - 273.15K}{K} + 84.715$$

$$\alpha_{tot}(T) := \frac{DN_{tot}(T)}{\int_{\lambda_1}^{\lambda_2} \varepsilon_{tc}\cdot S_{RF}(\lambda)\cdot E_b(\lambda, T)\, d\lambda}$$

Long/short pass equations:

$\text{lambda2} := 2475\text{nm}, 2476\text{nm}..6000\text{nm} \qquad \tau_{LP}(x) := \text{linterp}\left(\text{lambda}_{LP}, \text{trans}_{LP}, x\right)$

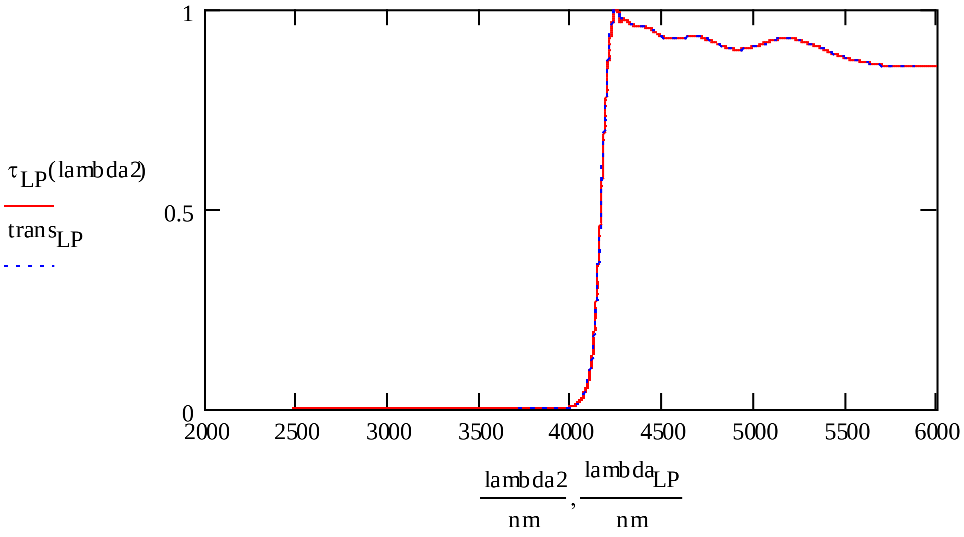

y = 0.0838x2 - 3.1429x + 46.086

$$T_{filter} := 290K, 291K..400K$$

$$DNLP(T) := 0.0838\left(\frac{T - 273.15K}{K}\right)^2 - 3.1429\frac{T - 273.15K}{K} + 46.08$$

$$\alpha LP(T) := \frac{DNLP(T)}{\int_{\lambda_1}^{\lambda_2} \varepsilon_{tc} \cdot S_{RF}(\lambda) \cdot \tau_{LP}(\lambda) \cdot E_b(\lambda, T)\, d\lambda}$$

$$\tau_{SP}(x) := \mathrm{linterp}\left(\mathrm{lambda}_{SP}, \mathrm{trans}_{SP}, x\right)$$

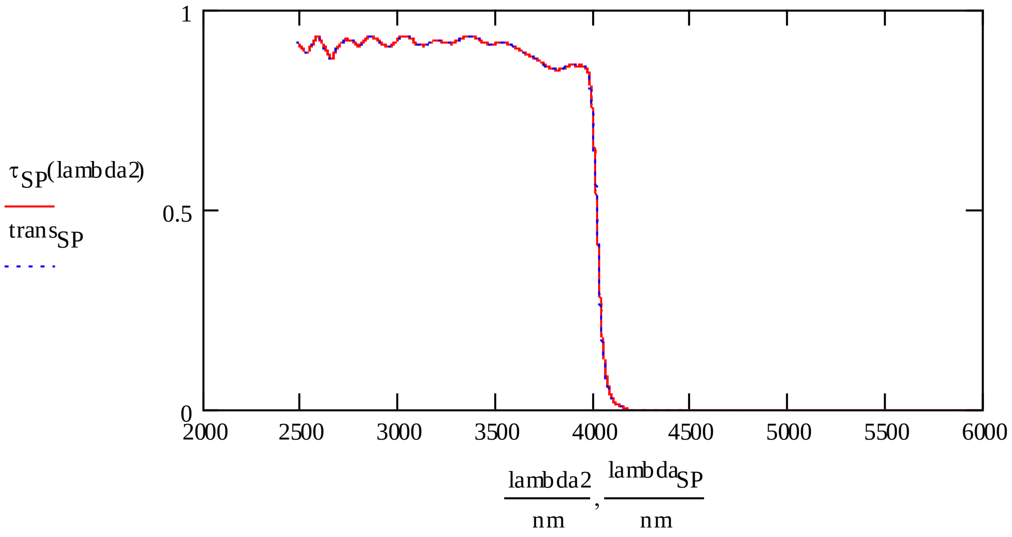

y = 0.0333x2 - 1.9283x + 56.558

$T_{filter} := 290K, 291K .. 400K$

$$DNSP(T) := 0.0333\left(\frac{T - 273.15K}{K}\right)^2 - 1.9283\frac{T - 273.15K}{K} + 56.55$$

$$\alpha SP(T) := \frac{DNSP(T)}{\int_{\lambda_1}^{\lambda_2} \varepsilon_{tc} \cdot S_{RF}(\lambda) \cdot \tau_{SP}(\lambda) \cdot E_b(\lambda, T)\, d\lambda}$$

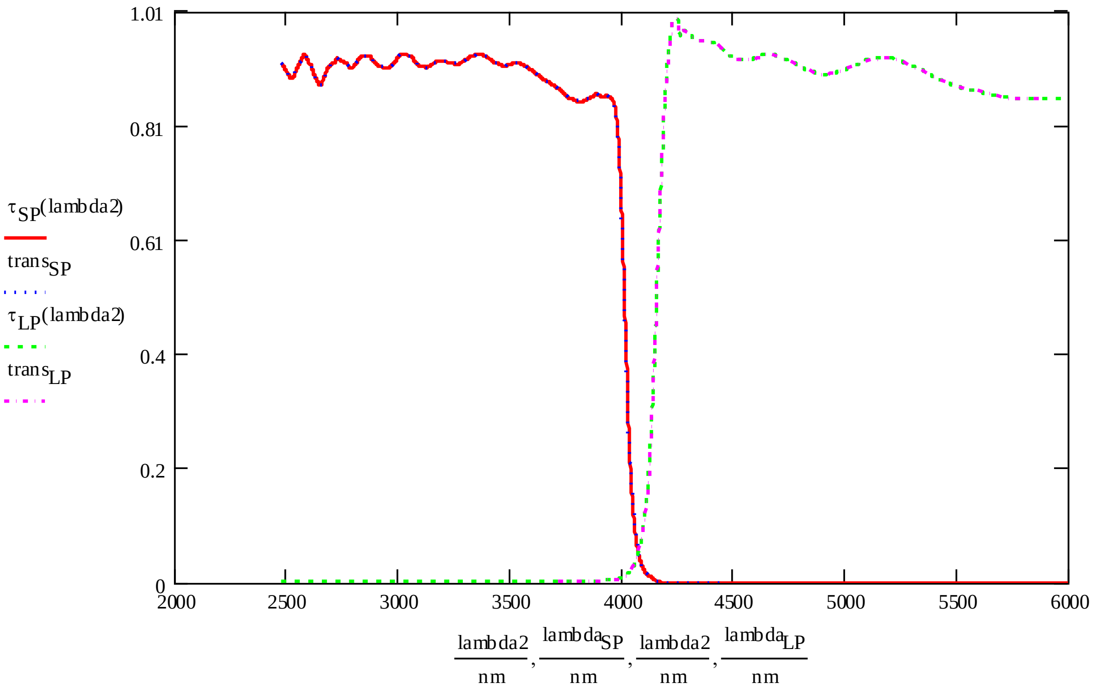

$T_{range} := 290K, 291K .. 400K$

$$DN_{tot}(\varepsilon, T) := \alpha_{tot}(T)\cdot\varepsilon\cdot\int_{\lambda_1}^{\lambda_2} S_{RF}(\lambda)\cdot E_b(\lambda, T)\, d\lambda$$

$$DN_{SP}(\varepsilon, T) := \alpha SP(T)\cdot\varepsilon\cdot\int_{\lambda_1}^{\lambda_2} S_{RF}(\lambda)\cdot\tau_{SP}(\lambda)\cdot E_b(\lambda, T)\, d\lambda$$

$$DN_{LP}(\varepsilon, T) := \alpha LP(T)\cdot\varepsilon\cdot\int_{\lambda_1}^{\lambda_2} S_{RF}(\lambda)\cdot\tau_{LP}(\lambda)\cdot E_b(\lambda, T)\, d\lambda$$

$T_{tot} := 100K + 273.15K$

$\varepsilon_{range} := 0.01, 0.02 .. 1.0$

Use this to estimate temperature for measurements without the filters:

Given

$\mathrm{DN}_{\mathrm{tot}}\left(0.69, \mathrm{T}_{\mathrm{tot}}\right) = 4198$

$\mathrm{T}_{\mathrm{tot}} := \mathrm{Find}\left(\mathrm{T}_{\mathrm{tot}}\right)$

$$\mathrm{dLPoSP} := \begin{pmatrix} 2.8 \\ 1.170238696 \end{pmatrix} \qquad \mathrm{D}_{\mathrm{tot}} := \begin{pmatrix} 119.372 \\ 163.312 \\ 266.2066667 \\ 135.0833333 \\ 342.1933333 \\ 254.2333333 \\ 167.9775 \\ 531.8933333 \\ 58.76333333 \\ 457.9875 \\ 20.58 \end{pmatrix}$$

$$\frac{\mathrm{DN}_{\mathrm{LP}}}{\mathrm{DN}_{\mathrm{SP}}} = \frac{\mathrm{alphaLP(T)} \cdot \int_{\lambda_1}^{\lambda_2} \mathrm{S}_{\mathrm{RF}}(\lambda) \cdot \tau_{\mathrm{LP}}(\lambda) \cdot \mathrm{E}_{\mathrm{b}}(\lambda, \mathrm{T})\, d\lambda}{\mathrm{alphaSP(T)} \cdot \int_{\lambda_1}^{\lambda_2} \mathrm{S}_{\mathrm{RF}}(\lambda) \cdot \tau_{\mathrm{SP}}(\lambda) \cdot \mathrm{E}_{\mathrm{b}}(\lambda, \mathrm{T})\, d\lambda}$$

$$\mathrm{LPoverSP}(\varepsilon, \mathrm{T}) := \frac{\mathrm{DN}_{\mathrm{LP}}(\varepsilon, \mathrm{T})}{\mathrm{DN}_{\mathrm{SP}}(\varepsilon, \mathrm{T})}$$

$\mathrm{LPoverSP}\left(\varepsilon_{\mathrm{tc}}, 317\mathrm{K}\right) = 1.926$

$$\mathrm{k} := 1 \qquad \mathrm{LPoSP} := \overrightarrow{\frac{\mathrm{D}_{\mathrm{LPdata}}}{\mathrm{D}_{\mathrm{SPdata}}}}$$

To find temperature with LP/SP filters:

$$\mathrm{Dtemp} := \begin{pmatrix} 3.275288871 \\ 27.092 \\ 33.834 \end{pmatrix}$$

$\mathrm{T} := 50\mathrm{K} + 273\mathrm{K}$

$\mathrm{LPoverSP}(0.8, T_{range}) = $ ▮

Given $\quad \mathrm{LPoverSP}(\varepsilon_{tc}, T) = \mathrm{dLPoSP}_k$

$T_{ex} := \mathrm{Find}(T) \qquad T_{ex} - 273.15K = $ ▮

To back out emissivity once temperature is known:

$\varepsilon_{guess} := 0.65$

Given

$\mathrm{DN}_{SP}(\varepsilon_{guess}, T_{ex}) = 36.5 \qquad \varepsilon_{exSP} := \mathrm{Find}(\varepsilon_{guess}) \qquad \varepsilon_{exSP} = $ ▮

Given

$\mathrm{DN}_{LP}(\varepsilon_{guess}, T_{ex}) = 72.5 \qquad \varepsilon_{exLP} := \mathrm{Find}(\varepsilon_{guess}) \qquad \varepsilon_{exLP} = $ ▮

Predicted temperature with no filter:

$$\varepsilon_{ex} := \frac{\varepsilon_{exSP} + \varepsilon_{exLP}}{2} \qquad T_{guess} := (50 + 273.15)K$$

Given

$\mathrm{DN}_{tot}(\varepsilon_{ex}, T_{guess}) = 75.756666 \quad T_{tot} := \mathrm{Find}(T_{guess})$

$T_{tot} - 273.15K = $ ▮

To find multiple temperatures with LP/SP filters:

$$\mathrm{dLPoSP} := \begin{pmatrix} 0.614717809 \\ 1.646957404 \\ 1.009420956 \\ 0.984201389 \end{pmatrix}$$

$i := 1..4$

$T_{guess} := 300K$

$$T_{balance_i} := \mathrm{root}\left[\left(\frac{\mathrm{LPoverSP}(\varepsilon_{tc}, T_{guess})}{\mathrm{dLPoSP}_i} - 1\right), T_{guess}\right]$$

$T_{ex} := T_{balance} - 273.15K \; T_{ex} = $ ▮

To find multiple temperatures with LP/SP filters:

$$\mathrm{dLPoSP} := \begin{pmatrix} 0.614717809 \\ 1.646957404 \\ 1.009420956 \\ 0.984201389 \end{pmatrix} \qquad i := 1..4$$

$T_{guess} \coloneqq 300K \quad T_{balance2_i} \coloneqq \mathrm{root}\left[\left(\frac{\frac{DNLP\left(T_{guess}\right)}{DNSP\left(T_{guess}\right)}}{dLPoSP_i} - 1\right), T_{guess}\right]$

$T_{balance2} = \blacksquare \quad T_{ex2} \coloneqq T_{balance2} - 273.15K \qquad T_{ex2} = \blacksquare$

Appendix C. Particle Sizing Subroutine

Main Matlab Code:

```
% BEGINNING OF CODE:
clear;
clc;

% LOADING OF PARTICLE IMAGE:
[filename,pathname] = uigetfile({'*.bmp','Image (*.bmp)'; ...
                                '*.*','All Files (*.*)'}, ...
                                'Select particle image file');

addpath(pathname);
imagefile = filename;

    P=imread(imagefile(1,:));
    P=double(P);
    P=P/255;
      [rows,cols,depth] = size(P);

% Get rid of red, blue behind particle.
    for i = 1:max(size(P))
        for j = 1:max(size(P))
            if P(i,j,2) > 38.0/255.0
                P(i,j,1) = 0;
                P(i,j,3) = 0;
            end
        end
    end

% % LOADING OF BRIGHT (He-Ne) IMAGE:
% [filename,pathname] = uigetfile({'*.bmp','Image (*.bmp)'; ...
%                                 '*.*','All Files (*.*)'}, ...
%                                 'Select background image file');
%
% addpath(pathname);
% imagefile = filename;
%
%     B=imread(imagefile(1,:));
%     B=double(B);
%     B=B/255;
%     [rows,cols,depth] = size(B);

% LOADING OF DARK IMAGE:
% [filename,pathname] = uigetfile({'*.bmp','Image (*.bmp)'; ...
%                                 '*.*','All Files (*.*)'}, ...
%                                 'Select dark image file');
```

```
%
% addpath(pathname);
% imagefile = filename;
%
%     D=imread(imagefile(1,:));
%     D=double(D);
%     D=D/255;
%     [rows,cols,depth] = size(D);

%     darkmax = max(max(max(D)));
%         disp(num2str(darkmax));
%         pause(0.1);
%     darkmin = min(min(min(D)));
%         disp(num2str(darkmin));
%         pause(0.1);

% CREATE FINAL IMAGE:
%     F = (P - D)./(B - D);
%     F = B - P;
%     for i = 1:max(size(F))
%         for j = 1:max(size(F))
%             for k = 1:3
%                 if F(i,j,k) > 1
%                     F(i,j,k) = 1;
%                 elseif F(i,j,k) < 0
%                     F(i,j,k) = 0;
%                 end
%             end
%         end
%     end

    F = P;

        % Crop image
        image(F);
            axis image;
        [X,Y] = ginput(2);

        % Size of area to average:
            x1 = round(X(1));
            x2 = round(X(2));
            y1 = round(Y(1));
            y2 = round(Y(2));

        close(gcf);

        figure;
        subplot(1,2,1);
%         set(gca,'Position',[0.03 0.52 0.94 0.44]);
        image(F(y1:y2,x1:x2,:));
        axis image;

      % RGB components
    Red = F(y1:y2,x1:x2,1);
      Green = F(y1:y2,x1:x2,2);
      Blue = F(y1:y2,x1:x2,3);
```

```
    composite(:,:,1) = Red;
    composite(:,:,2) = zeros(size(Red));
    composite(:,:,3) = zeros(size(Red));
    subplot(1,2,2);
%     set(gca,'Position',[0.03 0.03 0.94 0.44]);
    image(composite); axis image;

%     figure;
%     image(composite); axis image;

    PixValTotal = Red;

    % Edge detection using Sobel
    [mask,composite] =
edgefinder_nogreen(F(y1:y2,x1:x2,:),PixValTotal);
    composite(:,:,3) = double(bwperim(mask));

    % Sums the total number of pixels across particle image after
adjustment
        [row,col] = size(PixValTotal);
        sumTot = row*col - sum(sum(double(mask)));
%         disp(num2str(sumTot));
%         pause(0.1);

        area = 17*17*sumTot;                % camera has 17 micron
square pixels
        diameter = ((4*area/pi)^0.5)/90.17;   % units of microns; 89 is
a conversion
%         disp(num2str(diameter));            % for a magnification of
about 2.5x
%         pause(0.1);

    figure;
    image(composite);  axis image;
        title('Overlayed area is the particle');
        text(0.1,0.95,'Particle size =
','color','y','units','normalized','fontweight',...
            'bold','fontsize',14);

text(0.55,0.95,num2str(diameter),'color','y','units','normalized','font
weight',...
            'bold','fontsize',14);
```

Edgefinder Matlab Subroutine:

```
function [mask,composite] = edgefinder_nogreen(F,PixValTotal)
% Edge detection using Sobel
%-----------------------------------------------------------------------
------

C = zeros(size(F));

[row,col] = size(PixValTotal);
bwTot = false(size(PixValTotal));
% Detect edge of particle
% [bwT,ThreshTot] = edge(PixValTotal,'sobel');
```

```
% ThreshTot = ThreshTot;    % Increase threshhold value
ThreshTot = 0.2*max(max(PixValTotal));
disp(num2str(ThreshTot));   % Displays initial threshhold value
pause(0.1);
bwTot = PixValTotal >= ThreshTot;
mask = bwTot == 1;

% New stuff
Outside = zeros(size(F));
Inside = zeros(size(F));

%   Finds pixels inside and outside of particle area
    for i = 1:row
        for j = 1:col
            if F(i,j,1) > ThreshTot
                Outside(i,j) = F(i,j,1);
            elseif F(i,j,1) < ThreshTot
                Inside(i,j) = F(i,j,1);
            end
        end
    end

% Sums the values of pixels within each area
OutSum = sum(sum(Outside));
InSum = sum(sum(Inside));

% Finds the number of pixels within each area
InNum = (row*col - sum(sum(double(mask))));
OutNum = (sum(sum(double(mask))));

% Finds the average pixel value within each area
AvgOut = OutSum/OutNum;
AvgIn = InSum/InNum;

Diff = AvgOut(:,:,1) - AvgIn(:,:,1);

%   Recalculate threshhold value
    bwTot = false(size(PixValTotal));
    ThreshTot = AvgOut(:,:,1) - 0.85*Diff;
    bwTot = PixValTotal >= ThreshTot;
    mask = bwTot == 1;

% End of new stuff

figure;  set(gcf,'Name','Edge Finding ---
GLOBAL','Units','Normalized',...
    'Position',[0.01 0.04 0.98 0.88]);
    subplot(2,1,2);
    set(gca,'Units','Normalized','Position',[0.03 0.03 0.94 0.44]);
    composite(:,:,1) = PixValTotal;
    composite(:,:,2) = zeros(size(PixValTotal));
    composite(:,:,3) = double(bwperim(mask));
    image(composite);  axis image;

dummy = 1;
while dummy ~= 0    % adjust threshold values
    subplot(2,1,1);
```

```
    set(gca,'Units','Normalized','Position',[0.03 0.52 0.94 0.44]);
    imagesc(bwTot);  axis image;
%     text(1.05,1,'Inside Flame','color',[0.5625 0
0],'units','normalized',...
%         'fontweight','bold');
%     text(1.05,0.95,'Red Flame','color',[1 0.8125
0],'units','normalized',...
%         'fontweight','bold');
%     text(1.05,0.90,'Blue Flame','color',[0 0.8125
1],'units','normalized',...
%         'fontweight','bold');
%     text(1.05,0.85,'Outside Flame','color',[0 0 0.5625],'units',...
%         'normalized','fontweight','bold');

text(0.1,0.95,'dp+','color','y','units','normalized','fontweight',...
        'bold','fontsize',14);
%
text(0.2,0.90,'+','color','y','units','normalized','fontweight',...
%         'bold','fontsize',16);
    text(0.3,0.95,'dp-
','color','y','units','normalized','fontweight',...
        'bold','fontsize',14);
%
text(0.4,0.90,'+','color','y','units','normalized','fontweight',...
%         'bold','fontsize',16);
%     text(0.5,0.95,'B-
','color','y','units','normalized','fontweight',...
%         'bold','fontsize',14);
%
text(0.6,0.90,'+','color','y','units','normalized','fontweight',...
%         'bold','fontsize',16);
%
text(0.7,0.95,'B+','color','y','units','normalized','fontweight',...
%         'bold','fontsize',14);
%
text(0.8,0.90,'+','color','y','units','normalized','fontweight',...
%         'bold','fontsize',16);

text(0.9,0.95,'QUIT','color','y','units','normalized','fontweight',...
        'bold','fontsize',14);

text(0.1,0.05,'ADJUST','color','y','units','normalized','fontweight',..
.
        'bold','fontsize',14);
    % text is (0,0) @ lower left corner for normalized units

    pause(0.1);
    [X,Y] = ginput(1);  % ginput is (0,0) @ upper left corner
    x = X/col;
    y = Y/row;
    if x < 0.2 & y < 0.1
        ThreshTot = ThreshTot - 0.02;
    elseif 0.2 < x & x < 0.4 & y < 0.1
        ThreshTot = ThreshTot + 0.02;
    elseif 0.8 < x & x < 1.0 & y < 0.1
        dummy = 0;
        dummy1 = 0;
```

```
    elseif x < 0.2 & y > 0.9
        dummy = 0;
        dummy1 = 1;
    else
        dummy = 1;
    end

    bwTot = PixValTotal >= ThreshTot;
    mask = bwTot == 1;
    subplot(2,1,2);              % overlayed edge is part of particle
    set(gca,'Units','Normalized','Position',[0.03 0.03 0.94 0.44]);
    composite(:,:,3) = double(bwperim(mask));
    image(composite);  axis image;
end

disp(num2str(ThreshTot));   % Displays final threshhold value
pause(0.1);

close(gcf);

% Sums the initial total number of pixels across particle image
sumTot = sum(sum(double(mask)));
disp(num2str(sumTot));
pause(0.1);

pause(0.1);
figure;  set(gcf,'Name','Edge Finding','Units','Normalized',...
    'Position',[0.01 0.04 0.98 0.88]);
bwTot = PixValTotal >= ThreshTot;
mask = bwTot == 1;
composite(:,:,3) = double(bwperim(mask));
image(composite);  axis image;

flameperim = zeros(size(PixValTotal));
background = 1;     % Red channel
while dummy1 ~= 0   % adjust individual pixels or regions
      text(0.9,1.1,'QUIT','color','k','units','normalized','fontweight'
,...
        'bold','fontsize',14);

text(0.1,0.05,'FILL','color','y','units','normalized','fontweight',...
        'bold','fontsize',14);

text(0.1,0.95,'REMOVE','color','y','units','normalized','fontweight',..
.
        'bold','fontsize',14);
    text(-0.15,0.3,'CLEAN EDGE','color','k','units','normalized',...
        'fontweight','bold','fontsize',14);
%     text(-0.15,0.5,'----------','color','k','units','normalized',...
%         'fontweight','bold','fontsize',14);
    text(-0.15,0.7,'DRAW LINE','color','k','units','normalized',...
        'fontweight','bold','fontsize',14);
%     text(0.1,-0.1,'SNR PLOT','color','k','units','normalized',...
%         'fontweight','bold','fontsize',14);
%     text(0.35,-0.1,'RED PLOT','color','k','units','normalized',...
%         'fontweight','bold','fontsize',14);
```

```
%     text(0.68,-
0.1,'FLAME','color','k','units','normalized','fontweight',...
%         'bold','fontsize',14);
%     text(laserpixel/col-0.01,1.02,'\downarrow
LASER','color','k','units',...
%         'normalized','fontweight','bold','fontsize',14);

    pause(0.1);
    [X,Y] = ginput(1);
      x = round(X);
      y = round(Y);
    if 0.8 < x/col & x/col < 1.0 & y/row < 0
        dummy1 = 0;
    elseif x/col < 0.33 & y/row > 1.0
        background = 0;     % SNR
    elseif 0.33 < x/col & x/col < 0.67 & y/row > 1
        background = 1;     % normal
%     elseif 0.67 < x/col & x/col < 1.0 & y/row > 1
%         background = 2;     % flame
    elseif 0 < x/col & x/col < 0.2 & 0 < y/row & y/row < 0.1
        % Ask user for blob size to remove
            prompt  = 'Remove blobs smaller than size:';
        title   = 'Blob removal';
        lines   = 1;
        def     = {'30'};
        answer  = inputdlg(prompt,title,lines,def);
        blobsize = str2num(answer[4]);
        noblob = bwareaopen(mask,blobsize);
        bwTot = noblob == 1;
%         bwTot = 3*double(bwTot);
        bwTot = uint8(bwTot);
    elseif x/col < 0 & 0 < y/row & y/row <= 0.5     % draw line
        pause(0.1);
        [X,Y] = ginput(1);
            x1 = round(X);
            y1 = round(Y);
        [X,Y] = ginput(1);
            x2 = round(X);
            y2 = round(Y);
        dx = x2-x1;
        dy = y2-y1;
        if dx ~= 0
            slope = dy/dx;
        else
            slope = 1e9;
        end
        distance = max(abs(dy),abs(dx));
        for i=1:distance
            if abs(dx) >= abs(dy)
                if x1 > x2
                    i = -i;
                end
                y = round(y1 + slope*i);
                x = x1 + i;
                bwTot(y,x) = 3;
            else
                if y1 > y2
```

```
                    i = -i;
                end
                y = y1 + i;
                x = round(x1 + i/slope);
                bwTot(y,x) = 3;
            end
        end
    elseif x/col < 0 & 0.5 < y/row & y/row < 1
        % Ask user for edge pixel connectivity to remove
            prompt  = 'Remove edge pixels with connectivity less
than:';
        title   = 'Edge pixel removal';
        lines   = 1;
        def     = {'4'};
        answer  = inputdlg(prompt,title,lines,def);
        edgeconn = str2num(answer[4]);
        % 00000000
        % 00x00000  the x is 1 and produces maskcounter = 4
        % 11111111
        for i=2:row-1
            for j=2:col-1
                if flameperim(i,j) == 1
                              maskcounter = 0;
                              for k = i-1:i+1
                        for l = j-1:j+1
                            if mask(k,l) ~= 0
                                maskcounter = maskcounter + 1;
                            end
                        end
                              end
                              if maskcounter > edgeconn
                        bwTot(i,j) = 1;
                    else
                        bwTot(i,j) = 0;
                              end
                end
            end
            end
     elseif x/col < 0.2 & y/row > 0.9
         bwTot = imfill(bwTot,'holes');
    else
            if bwTot(y,x) == 1
            bwTot(y,x) = 0;
            elseif bwTot(y,x) ~= 1
            bwTot(y,x) = 1;
            end
    end
%     mask = bwflame == 3;
    mask = bwTot == 1;
%     flameperim = bwperim(mask);
%     if background == 1
%         Red(1:10,laserpixel) = 1023;        % show laser location
%         Red(end-9:end,laserpixel) = 1023;
%         imagesc(Red + 900*double(flameperim));  axis image;
% %     elseif background == 0
% %         snrR(1:10,laserpixel) = 60;
% %         snrR(end-9:end,laserpixel) = 60;
```

```
% %         imagesc(snrR + 60*double(flameperim));  axis image;
%     else
%         C(1:10,laserpixel,2) = 1023;
%         C(end-9:end,laserpixel,2) = 1023;
%         C(:,:,1) = 256*double(flameperim);
%         overlay = imadjust(((A+C+1)/1280),[],[],0.4);
%         image(overlay);  axis image;
%     end
end

% Sums the total number of pixels across particle image after
adjustment
sumTot = sum(sum(double(mask)));
disp(num2str(sumTot));
pause(0.1);

area = 17*17*sumTot;                % camera has 17 micron square
pixels
diameter = ((4*area/pi)^0.5)/89;    % units of microns; 89 is a
conversion
disp(num2str(diameter));            % for a magnification of about 2.5x
pause(0.1);

% circum = sumTot*17;
% diameter = circum/pi/89;
% disp(num2str(diameter));

close(gcf);
```

Appendix D. Particle Levitation Model Code

Particle temperature from force balance:

$\mu m := 10^{-6} m \qquad kW := 1000W \qquad mW := 0.001W$

Constants:

$\sigma := 5.67 \cdot 10^{-8} \frac{W}{m^2 \cdot K^4} \qquad R_g := 8.3145 \frac{J}{K \cdot mol} \qquad c := 2.9979 \cdot 10^8 \frac{m}{s} \qquad kmol := 1000mol$

Planck's constant: $h_b := 6.626 \cdot 10^{-34} J \cdot s$

$P := 1atm \qquad MW_{air} := 28.85 \frac{gm}{mol} \qquad g = 9.807 \frac{m}{s^2}$

Density of black liquor: $\rho_{BL} := 1550 \frac{kg}{m^3}$

$T_{inf} := 295K \qquad \rho_{air} := 1.177 \frac{kg}{m^3} \quad \rho_{AL} := 2700 \frac{kg}{m^3} \quad T_{film}(T) := \frac{T + T_{inf}}{2} \quad \rho_{film}(T) := \frac{P \cdot MW_{air}}{R_g \cdot T_{film}(T)}$

$A_p(d_p) := \pi \cdot \left(\frac{d_p}{2}\right)^2 \qquad V(d_p) := \frac{4}{3} \pi \cdot \left(\frac{d_p}{2}\right)^3$

(The subscript *p* refers to the particle; *g* refers to the gas -- air in this case.)

$mass_{BL}(d_p) := V(d_p) \cdot \rho_{BL}$

Viscosity of air:

$mass_{BL}(5.5\mu m) \cdot g = 1.3242 \times 10^{-12} N$

$\mu_A := 1.425 \times 10^{-6} \qquad \mu_B := 0.504 \qquad \mu_C := 108.3$

$$\mu_g(T) := \frac{\mu_A \cdot \left(\frac{T_{film}(T)}{K}\right)^{\mu_B}}{1 + \frac{\mu_C \cdot K}{T_{film}(T)}} \cdot Pa \cdot s$$

Thermal conductivity of air:

$k_A := 3.142\times 10^{-4} \qquad k_B := 0.77 \qquad k_C := -0.71 \qquad k_D := 2.122\times 10^{3}$

$$k_g(T) := \frac{k_A\cdot\left(\frac{T_{film}(T)}{K}\right)^{k_B}}{1+\frac{k_C\cdot K}{T_{film}(T)}+\frac{k_D\cdot K^2}{T_{film}(T)^2}}\cdot\frac{W}{m\cdot K}$$

Density of air (ideal gas):

$$\rho_g(T) := \frac{P\cdot MW_{air}}{R_g\cdot T}$$

Heat capacity of air:

$Cp_A := 2.8958\times 10^{4} \qquad Cp_B := 9.39\,10^{3} \qquad Cp_C := 3.012\,10^{3} \qquad Cp_D := 7.58\,10^{3} \qquad Cp_E := 1.484\,10^{3}$

$$Cp_g(T) := \left[Cp_A + Cp_B\cdot\left(\frac{\frac{Cp_C\cdot K}{T_{film}(T)}}{\sinh\left(\frac{Cp_C\cdot K}{T_{film}(T)}\right)}\right)^2 + Cp_D\cdot\left(\frac{\frac{Cp_E\cdot K}{T_{film}(T)}}{\cosh\left(\frac{Cp_E\cdot K}{T_{film}(T)}\right)}\right)^2\right]\cdot\frac{1}{MW_{air}}\cdot\frac{J}{kmol\cdot K}$$

Estimate of heat transfer coefficient:

Prandtl number: $\quad Pr(T) := \frac{Cp_g(T)\cdot\mu_g(T)}{k_g(T)}$

$$\nu(T) := \frac{\mu_g(T)}{\rho_{film}(T)} \qquad \beta(T) := \frac{1}{\frac{T+T_{inf}}{2}} \qquad \alpha(T) := \frac{k_g(T)}{Cp_g(T)\cdot\rho_{film}(T)}$$

$$Ra(T,d) := \frac{g\cdot\beta(T)\cdot\left(T-T_{inf}\right)\cdot d^3}{\nu(T)\cdot\alpha(T)} \qquad Nu(T,d) := 2+\frac{0.589\,Ra(T,d)^{\frac{1}{4}}}{\left[1+\left(\frac{0.469}{Pr(T)}\right)^{\frac{9}{16}}\right]^{\frac{4}{9}}}$$

$$Nu(500K, 10\mu m) = 2.022 \qquad h(T,d) := \frac{Nu(T,d)\cdot k_g(T)}{d}$$

$$h(300K, 20\mu m) = 2.625\times 10^{3}\,\frac{W}{m^{2}\cdot K}$$

$$Bi = \frac{h\cdot dp}{6\cdot kp} \qquad kp := 0.18\frac{W}{m\cdot K}$$

Estimated from Incropera and DeWitt [58].

Cross-sectional area of each beam:

$$A_{beam1}(d_{beam1}) := \pi\cdot\left(\frac{d_{beam1}}{2}\right)^{2} \qquad A_{beam2}(d_{beam2}) := \pi\cdot\left(\frac{d_{beam2}}{2}\right)^{2}$$

$$Bi(T, d) := \frac{h(T, d)\cdot d}{6\cdot kp} \qquad Bi(322K, 5\mu m) = 0.04984$$

Overall energy balance:

beam1 = trapping beam
beam2 = heating beam

Radiation from particle:

$$q_{rad}(d, T, \varepsilon) := 4\cdot\pi\cdot\left(\frac{d}{2}\right)^{2}\cdot\varepsilon\cdot\sigma\cdot\left(T^{4} - T_{inf}{}^{4}\right)$$

Convection from particle:

$$q_{conv}(d, T) := 4\cdot\pi\cdot\left(\frac{d}{2}\right)^{2}\cdot h(T, d)\left(T - T_{inf}\right)$$

$r_c := 0\mu m \qquad P := 2W \quad \omega_o := 220\mu m \qquad d_p := 5\mu m \qquad \varepsilon := 0.6$

Incident intensity:

$Trad := 325K$

$$q_{rad}(d_p, Trad, \varepsilon) = 1.005\times 10^{-8}W \qquad I_o(P, \omega_o) := \frac{2\cdot P}{\pi\cdot\omega_o{}^{2}}$$

$$P_{inc}(r_c, P, \omega_o, d_p) := \int_{0}^{2\cdot\pi}\int_{0}^{\frac{d_p}{2}} I_o(P, \omega_o)\cdot\exp\left[\frac{-2\cdot\left[\left(r_c + r\cdot\cos(\theta)\right)^{2} + \left(r\cdot\sin(\theta)\right)^{2}\right]}{\omega_o{}^{2}}\right]\cdot r\,dr\,d\theta$$

$$q_{conv}(d_p, Trad) = 2.547\times 10^{-5}W$$

$$\boxed{q_{laser}(r_c, P, \omega_o, d_p, \varepsilon) := \varepsilon \cdot P_{inc}(r_c, P, \omega_o, d_p)}$$

$$q_{laser}(r_c, P, \omega_o, d_p, \varepsilon) = 3.254 \times 10^{-4} W$$

We measured the full-width half-max, which is actually 0.59*wo [84].

Guess temperature:

$T_p := 900K$

Given

$$q_{laser}(r_c, P, \omega_o, d_p, \varepsilon) = (q_{rad}(d_p, T_p, \varepsilon) + q_{conv}(d_p, T_p))$$

$$\boxed{T_p(r_c, P, \omega_o, d_p, \varepsilon) := \mathrm{Find}(T_p)}$$

$\left(T_p(r_c, P, \omega_o, d_p, \varepsilon) - 273.15K\right) \cdot \frac{1}{K} = 310.41$ Particle temperature in Celcius.

Particle Levitation Model:

(Iteration to find where particle sits with respect to focal point and more accurate surface temperature)

1) Given particle diameter
2) Calculate particle weight
3) Guess beam diameter
4) Calculate particle temperature from energy balance
5) Determine drag force from Fluent results
6) Determine photon force
7) Check if Fg = Fdrag + Fphoton (if not, return to step 3)
    - if Fg < Fdrag + Fphoton, increase beam diameter
    - if Fg > Fdrag + Fphoton, decrease beam diameter

$$a := \begin{pmatrix} 0.007639 \\ -0.010851 \\ 0.019197 \\ -0.098128 \\ 0.119775 \end{pmatrix}$$ These coefficients are for low Tp (< 350K) and small dp (<= 5 μm).

$$b := \begin{pmatrix} 0.000294 \\ 0.008379 \\ -0.026115 \\ 0.012812 \\ -0.085617 \\ 0.358367 \end{pmatrix}$$ These coefficients are for Tp > 325K and dp > 5 μm.

$$A(d_p) := a_0 \cdot \left(\frac{d_p}{\mu m}\right) + a_1 \qquad C(d_p) := b_0 \cdot \left(\frac{d_p}{\mu m}\right)^2 + b_1 \cdot \left(\frac{d_p}{\mu m}\right) + b_2$$

1) $d_p := 7.5\mu m$

2) $F_g(d_p) := \frac{4}{3} \cdot \pi \cdot \left(\frac{d_p}{2}\right)^3 \cdot \rho_{BL} \cdot g \qquad F_g := F_g(d_p) \qquad F_g = 3.358 \times 10^{-12} N$

$$B(d_p) := a_2 \cdot \left(\frac{d_p}{\mu m}\right)^2 + a_3 \cdot \left(\frac{d_p}{\mu m}\right) + a_4$$

$$D(d_p) := b_3 \cdot \left(\frac{d_p}{\mu m}\right)^2 + b_4 \cdot \left(\frac{d_p}{\mu m}\right) + b_5$$

3) $\omega_o := 150\mu m$

$$A_{cs}(d_p) := \pi \cdot \left(\frac{d_p}{2}\right)^2 \qquad dT(T_p) := \frac{T_p - T_{inf}}{K}$$

$r_c := 0\mu m \qquad P := 1W \qquad \omega_o = 150\mu m \qquad d_p = 7.5\mu m \qquad \varepsilon := 0.8$

4) $T_p := T_p(r_c, P, \omega_o, d_p, \varepsilon) \qquad T_p = \text{function} \qquad T_{p.celcius} := \frac{T_p - 273.15K}{K} \qquad T_{p.celcius} =$

5) $F_{drag.low}(d_p, T_p) := \left(A(d_p) \cdot dT(T_p) + B(d_p)\right) \cdot 10^{-12} N$ This drag equation is for low Tp and dp.

$F_{drag.high}(d_p, T_p) := \left(C(d_p) \cdot dT(T_p) + D(d_p)\right) \cdot 10^{-12} N$ This drag equation is for high Tp and dp.

6) Coefficients for photon forces:

$$I_{inc\_exact}(r_c, P, \omega_o, d_p) := \frac{P_{inc}(r_c, P, \omega_o, d_p)}{A_{cs}(d_p)} \qquad I_{inc\_exact}(r_c, P, \omega_o, d_p) = 2.8277 \times 10^{7} \frac{W}{m^2}$$

$$Az(d_p) := \left[0.7461 m^2 \cdot \left(\frac{d_p}{\mu m}\right)^2 + 0.9724 m^2 \cdot \frac{d_p}{\mu m} - 2.541 m^2\right] \cdot 10^{-12} \qquad Bz := 0.500$$

$$F_{photon\_z}\left(r_c, P, \omega_o, d_p\right) := \frac{I_{inc\_exact}\left(r_c, P, \omega_o, d_p\right)}{c} \cdot Az\left(d_p\right) \cdot \exp\left[\frac{-\left(\frac{r_c}{\omega_o}\right)^2}{2 \cdot Bz^2}\right]$$

$$Ax\left(d_p\right) := \left[355.3m^2 \cdot \left(\frac{d_p}{\mu m}\right)^2 - 2291m^2 \cdot \frac{d_p}{\mu m} + 5044m^2\right] \cdot 10^{-12}$$

$F_{photon\_z} := F_{photon\_z}\left(r_c, P, \omega_o, d_p\right)$ $\qquad$ $F_{photon\_z} = 4.407 \times 10^{-12}\,N$

$Bx := 0.501$ $\qquad$ $Cx := -0.994$ $\qquad$ $T_{low} := 290K, 291K .. 400K$

$$F_{photon\_x}\left(r_c, P, \omega_o, d_p\right) := \frac{I_{inc\_exact}\left(r_c, P, \omega_o, d_p\right)}{c} \cdot \frac{Ax\left(d_p\right) \cdot \left(\frac{\omega_o}{\mu m}\right)^{Cx} \cdot \left(\frac{r_c}{\omega_o}\right) \cdot \exp\left[\frac{-\left(\frac{r_c}{\omega_o}\right)^2}{2 \cdot Bx^2}\right]}{-1000\,Bx^2}$$

$F_{photon\_x} := F_{photon\_x}\left(r_c, P, \omega_o, d_p\right)$ $\qquad$ $\frac{F_{photon\_x}}{10^{-20}} = 0 \times 10^{0}\,N$

7) $\frac{F_g}{F_{drag} + F_{photon\_z}} = \blacksquare$ (Iterate until this ratio equals 1)

Distance from the focal point:

$nm := 10^{-9}m$ $\qquad$ $f := 4cm$ $\qquad$ $Diam := 2cm$ $\qquad$ $\lambda := 532nm$

$w_{o\_true} := \frac{2 \cdot \lambda \cdot f}{Diam \cdot \pi}$ $\qquad$ $w_{o\_true} = 0.677\mu m$

Guess: $x := 1mm$

Given

$$\omega_o = \sqrt{w_{o\_true}^2 \cdot \left[1 + \left(\frac{\lambda \cdot x}{\pi \cdot w_{o\_true}^2}\right)^2\right]}$$

$x := \mathrm{Find}(x)$ $\qquad$ $x = 599.99\mu m$

Gaussian beam:

A beam of light whose electrical field amplitude distribution is Gaussian. When such a beam is circular in cross section, the amplitude is E(r) = E(0) exp [-(r/w)^2], where r is the distance from beam center and w is the radius at which the amplitude is 1/e of its value on the axis; w is called the beam width [85].

(Streamlined) Particle Levitation Model:

$d_p := 7.8\mu m$ $\quad \omega_o := 220\mu m$ $\quad r_c := 0\mu m$ $\quad P := 0.75W$ $\quad \varepsilon := 0.63$

$$T_p(r_c, P, \omega_o, d_p, \varepsilon) = \blacksquare \qquad F_g(d_p) := \frac{4}{3}\cdot\pi\cdot\left(\frac{d_p}{2}\right)^3\cdot\rho_{BL}\cdot g$$

$$T_{p.celcius}(r_c, P, \omega_o, d_p, \varepsilon) := \frac{T_p(r_c, P, \omega_o, d_p, \varepsilon) - 273.15K}{K} \qquad T_{p.celcius}(r_c, P, \omega_o, d_p, \varepsilon) = 207.78$$

$$dT(r_c, P, \omega_o, d_p, \varepsilon) := \frac{T_p(r_c, P, \omega_o, d_p, \varepsilon) - T_{inf}}{K}$$

$$F_{drag.low}(r_c, P, \omega_o, d_p, \varepsilon) := \left(A(d_p)\cdot dT(r_c, P, \omega_o, d_p, \varepsilon) + B(d_p)\right)\cdot 10^{-12}N$$

$$F_{drag.high}(r_c, P, \omega_o, d_p, \varepsilon) := \left(C(d_p)\cdot dT(r_c, P, \omega_o, d_p, \varepsilon) + D(d_p)\right)\cdot 10^{-12}N$$

$$F_{photon\_z}(r_c, P, \omega_o, d_p) := \frac{I_{inc\_exact}(r_c, P, \omega_o, d_p)}{c}\cdot Az(d_p)\cdot \exp\left[\frac{-\left(\frac{r_c}{\omega_o}\right)^2}{2\cdot Bz^2}\right]$$

$$F_{photon\_x}(r_c, P, \omega_o, d_p) := \frac{I_{inc\_exact}(r_c, P, \omega_o, d_p)}{c}\cdot\frac{Ax(d_p)\cdot\left(\frac{\omega_o}{\mu m}\right)^{Cx}\cdot\left(\frac{r_c}{\omega_o}\right)\cdot \exp\left[\frac{-\left(\frac{r_c}{\omega_o}\right)^2}{2\cdot Bx^2}\right]}{-1000Bx^2}$$

$$\frac{F_g(d_p)}{F_{drag.tot}(r_c, P, \omega_o, d_p, \varepsilon) + F_{photon\_z}(r_c, P, \omega_o, d_p)} = \blacksquare$$

$$\begin{pmatrix} F_g(d_p) \\ F_{drag.tot}(r_c, P, \omega_o, d_p, \varepsilon) \\ F_{photon\_z}(r_c, P, \omega_o, d_p) \\ \dfrac{F_{photon\_x}(r_c, P, \omega_o, d_p)}{10^{-20}} \end{pmatrix} = \blacksquare \qquad \frac{F_{photon\_z}(r_c, P, \omega_o, d_p)}{F_{drag}(r_c, P, \omega_o, d_p, \varepsilon)} = \blacksquare\,\%$$

Distance from focal point:

Given

$$\omega_o = \sqrt{w_{o\_true}^2 \cdot \left[1 + \left(\frac{\lambda \cdot x}{\pi \cdot w_{o\_true}^2}\right)^2\right]}$$

$x := \mathrm{Find}(x) \qquad x = 0.88\mathrm{mm}$

High drag eqn. for >325K and >5 µm.

This is temperature limit b/w drag eqns.

$$\frac{325K - 273.15K}{K} = 51.85 \ \mathrm{degC}$$

(Fastest) Particle Levitation Model (single size):

Guess: $d_p := 9\mu m$

$r_c := 0\mu m \qquad P := 0.75W \qquad \varepsilon := 0.668 \qquad \omega_o := 500\mu m \qquad \rho_{BL} = 1550\frac{kg}{m^3}$

$$\omega_{balance} := \mathrm{root}\left(\frac{F_g(d_p)}{F_{drag.high}(r_c, P, \omega_o, d_p, \varepsilon) + F_{photon\_z}(r_c, P, \omega_o, d_p)} - 1, \omega_o\right)$$

$\omega_{balance} = 446.392\mu m \qquad \omega_o := \omega_{balance} \qquad T_{p.celcius}(r_c, P, \omega_o, d_p, \varepsilon) = 85.354$

$$\begin{pmatrix} F_g(d_p) \\ F_{drag.low}(r_c, P, \omega_o, d_p, \varepsilon) \\ F_{photon\_z}(r_c, P, \omega_o, d_p) \\ \frac{F_{photon\_x}(r_c, P, \omega_o, d_p)}{10^{-20}} \end{pmatrix} = ■ \qquad I_{inc\_exact}(r_c, P, \omega_o, d_p) = ■$$

$P_{test} := 5W \qquad w_{test} := 2.5\mu m \qquad d_{test} := 35\mu m$

Comparison of drag fit equations:

$I_{inc\_exact}(r_c, P_{test}, w_{test}, d_{test}) = ■$

$d_{ex} := 6\mu m \qquad w_{ex} := 100\mu m, 200\mu m .. 1000\mu m \qquad w_{ex1} := 700\mu m$

$F_g(d_{ex}) = ■$

$F_{drag.tot}(r_c, P, w_{ex1}, d_{ex}, \varepsilon) = ■$

$F_{drag.low}(r_c, P, w_{ex1}, d_{ex}, \varepsilon) = ■$

$F_{photon\_z}(r_c, P, w_{ex1}, d_{ex}) = ■$

Particle Levitation Model (multiple sizes):

$\rho_{BL} = ▮$

Guess: $d_p := \begin{pmatrix} 3.66 \\ 2.80 \\ 3.40 \\ 3.31 \\ 4.55 \\ 3.22 \\ 5.1 \\ 3.29 \\ 3.8 \\ 2.58 \\ 1.72 \\ 1.97 \end{pmatrix} \mu m$

$i := 0, 1 .. 11 \qquad r_c := 0\mu m \qquad P := 0.75W \qquad \varepsilon := 0.66 \qquad \omega_o := 500\mu m$

$$\omega_{balance_i} := \mathrm{root}\left[\left(\frac{F_g\left(d_{p_i}\right)}{F_{drag.low}\left(r_c, P, \omega_o, d_{p_i}, \varepsilon\right) + F_{photon\_z}\left(r_c, P, \omega_o, d_{p_i}\right)} - 1\right), \omega_o\right]$$

$\omega_{balance} = ▮\ \mu m \qquad \omega_o := \omega_{balance} \qquad T_{p.celcius}\left(r_c, P, \omega_{o_i}, d_{p_i}, \varepsilon\right) = ▮$

$I_{inc\_exact}\left(r_c, P, \omega_{o_i}, d_{p_i}\right)$ $\qquad \dfrac{F_g\left(d_{p_i}\right)}{10^{-12}}$ $\qquad \dfrac{F_{drag.low}\left(r_c, P, \omega_{o_i}, d_{p_i}, \varepsilon\right)}{10^{-12}}$

▮ ▮ ▮

$\dfrac{F_{photon\_z}\left(r_c, P, \omega_{o_i}, d_{p_i}\right)}{10^{-12}}$ $\qquad \dfrac{F_{photon\_x}\left(r_c, P, \omega_{o_i}, d_{p_i}\right)}{10^{-20}}$

▮ ▮